Modeling of plasmon mediated single-photon devices

Chen, Yuntian

Publication date:
2010

Document Version
Publisher's PDF, also known as Version of record

Modeling of plasmon mediated single-photon devices

A dissertation
submitted to the Department of Photonics Engineering
at the Technical University of Denmark
in partial fulfillment of the requirements
for the degree of
philosophiae doctor

Yuntian Chen
January 6, 2011

DTU Fotonik
Department of Photonics Engineering
Technical University of Denmark

Preface

The research presented in the thesis was carried out in the Theory and Signal Processing Group at DTU Fotonik from September 2007 to August 2010 during my Ph.D study. The Ph.D study has been supervised by Prof. Jepser Mørk, Associate Prof. Peter Lodahl, Assistant Prof. Torben R. Nielsen and Assistant Prof. Niels Gregersen.

Firstly, I would like to express my utmost gratitude to my supervisors for their guidance and support during the three years. I would like thank Jesper for providing the opportunity to carry out such an exciting research project during my ph.d study, and for sharing his great knowledge and physical insights in modeling of nanophotonic devices. I also would also like to thank Peter, Niels and Torben for sharing their knowledges, and also for always for being available for questions.

Secondly, I also would like to thank Dr. Femius Koenderink for hosting me in Resonant Nanophotonics group at AMOLF, Amsterdam, the Netherlands. During the external stay, I had a great time of working with Dr. Femius Koenderink.

Thirdly, I also would like to thank the people at Nanophotonics Cluster for all informal discussions and the enjoyable coffee time. In particular, I would like to acknowledge Mads, Qin, Philip for simulating discussions. I also want to thank my Chinese friends, including Sanshui, Minhao, Lirong, Yaohui, Liuliu, Weiqi, Jihua, Pengliang, Huhao and many more. Without the parties and their company, I would not have had such a lot fun in my spare time during the three years.

Finally, I would like to express very special thanks to my wife, Jing, for her unconditional support and the appreciation for my absence during many weekends.

Yuntian Chen

September, 2010

Abstract

The thesis describes the theoretical study of optical plasmons mediated light-matter interaction, with an emphasis on developing efficient single photon sources by engineering the spontaneous emission of a single emitter coupled to plasmonic nanostructures.

Firstly, we develop a self-consistent finite element method to quantitatively study spontaneous emission from emitters in nanoscale proximity of plasmonic waveguides. It is assumed that only one guided mode is dominatingly excited, while the cross section of the plasmonic waveguide can be arbitrary. The fraction of the energy coupled to the plasmonic mode can be calculated exactly, which can be used to determine the efficiency with which single optical plasmons are generated. The numerical method is applied to calculate the coupling of a emitter coupled to a cylindrical nanowire and a square metallic nanowire.

Secondly, we numerically investigate the coupling efficiency of a single self-assembled quantum dot coupled to a metallic slot waveguide embedded in inhomogenous dielectric environment. Due to the inhomogeneity, leaky plasmonic modes referring to radiation modes with plasmonic features will be excited. Compared with the ideal case of the homogenous dielectric environment, the coupling efficiency is significantly reduced due to the excitation of the leaky plasmonic modes. By increasing the refractive index of the coating layer to minimize the impacts from the leaky plasmonic modes, we find that the coupling efficiency can be enhanced by more than a factor 2.

Last, we examine a quantum emitter coupled to free photons, mediated by optical nanoantennas. We mimic the conventional Yagi-Uda to realize its optical analogy based on an array consisting of several metallic rods. We also propose a plasmon-based reconfigurable antenna to controllably distribute emission from a single emitter in spatially separated channels. Our calculations show that crossed

particle arrays can split the stream of photons from the emitter into multiple narrow beams. We predict that beams can be switched on and off by switching host refractive index.

Resumé

Denne afhandling beskriver teoretiske undersøgelser af lys-stof vekselvirkning medieret af optiske plasmoner. Hovedvægten er på udviklingen af effektive enkeltfotonkilder der virker ved at kontrollere den spontane lysudsendelse af en enkelt lysudsender ved at koble denne til plasmoniske nanostrukturer.

Vi udvikler en selvkonsistent finite-element metode til kvantitativt at studere den spontane lysudsendelse fra lyskilder i nanometer-nærhed af plasmoniske bølgeledere. Det er antaget at kun en enkelt bølgeledertilstand primært er anslået, mens tværsnittet af den plasmoniske bølgeleder kan være arbitrært. Brøkdelen af energien der bliver overført til den plasmoniske tilstand kan udregnes eksakt, hvilket kan bruges til at bestemme genereringenseffektiviteten af enkelte optiske plasmoner. Den numeriske metode er anvendt til at udregne koblingen af en lysudsender til en cylindrisk-og en kvadratisk metallisk bølgeleder.

Vi undersøger numerisk koblingseffektiviteten af et enkelt selv-samlet kvantepunkt til en metallisk mellemrumsbølgeleder der er indkapslet i ikke-homogene dielektriske omgivelser. På grund af de ikke-homogene omgivelser vil ikke-bundne plasmoniske tilstande, der er udstrålings tilstande, blive exciteret. Sammenlignet med det optimale tilfælde, som er homogene omgivelser, vil koblingseffektiviteten være betragteligt nedsat på grund af exciteringen af disse ikke-bundne plasmoniske tilstande. Ved at forøge brydningsindekset af det overdækkende lag, for at minimerer effekten af de ikke-bundne plasmoniske tilstande, finder vi at koblingseffektiviteten kan blive forøget med mere end en faktor 2.

Til slut undersøger vi koblingen af kvantelyskilder til frie fotoner medieret af optiske nano-antenner. Vi efterligner det konventionelle Yagi-Uda design og realiserer dets optiske analogi baseret på et array bestående af adskillige metalstænger. Derudover, foreslår vi en plasmon-baseret rekonfigurable antenne til kontrolleret at distribuere lysudsendelse fra en enkelt lyskilde til rumligt adskilte kanaler. Vores

udregninger viser at krydsede partikelarrays kan opdele strømmen af fotoner fra en emitter ind i adskillige tynde stråler. Vi forudser at strålerne kan blive tændt og slukket ved at skifte værtsbrydningsindekset.

Ph.D. Publications

The following publications have resulted from this Ph.D. project.

1. Y. Chen, P. Lodahl, and A. F. Koenderink, Dynamically reconfigurable directionality of plasmon-based single photon sources, Phys. Rev. B, **82**, 081402 (2010)

2. Y. Chen, T. R. Nielsen, N. Gregersen, P. Lodahl, and J. Mørk, Finite-element modeling of spontaneous emission of a quantum emitter at nanoscale proximity to plasmonic waveguides, Phys. Rev. B, **81**, 125431 (2010)

3. Y. Chen, N. Gregersen, T. R. Nielsen, J. Mørk, and P. Lodahl , Spontaneous decay of a single quantum dot coupled to a metallic slot waveguide in the presence of leaky plasmonic modes, Optics Express, **18**, 12489 (2010)

Conference contributions

1. Y. Chen, T. R. Nielsen, N. Gregersen, P. Lodahl, and J. Mørk, Optimizing the spontaneous-emission β factor for single optical plasmon generation, CLEO Europe, Munich, Germany 2009.

2. Y. Chen, S. S. Xiao, T. R. Nielsen, Guided plasmon polaritons for triangular metallic waveguides, Asia-Pacific Optical Communications (APOC), Hangzhou, China 2008.

Some other work,

1. Y. Chen, G. Björk, Generation and detection of the photonic qutrit by linear optics, QUANTUM INFORM. COMPU. **8**, 0386, 2008

2. Y. Chen, Y. Cai, Halil T. Eyyuboğlu and Y. Baykal, Scintillation properties of dark hollow beams in a weak turbulent atmosphere, Applied Physics B: Lasers and Optics, **90**, 87, 2008

3. Y. Cai, Y. Chen, H. T. Eyyuboğlu and Y. Baykal, Propagation of laser array beams in a turbulent atmosphere, Applied Physics B: Lasers and optics, , 467, 2007

4. Y. Cai, Y. Chen, H. T. Eyyuboğlu and Y. Baykal, Scintillation index of elliptical Gaussian beam in turbulent atmosphere, Optical Letter. **32**, 2405, 2007

Contents

Chapter 1

Introduction

Controllably and efficiently extracting photons from single quantum emitters into a well-defined set of modes, or viceversa, is a holy grail for quantum optics, optical quantum computation, as well as single molecule spectroscopy. The conventional approach is to place the emitter inside a high finesse ultrasmall cavity, such as a micropillar [1, 2], microsphere or toroid [3], or photonic crystal cavity [4]. Such ultimate control over single light quanta is of core interest in cavity quantum electrodynamics, and increasingly important in nanophotonics. By virtue of the tremendous interaction strength of free electrons in noble metals with photons, plasmon polaritons offer very tight field confinement over very large frequency bandwidths. Especially plasmonic nanoparticles and nanowires promise the ability to manipulate light at nano-meter scale. In addition to applications in subwavelength optoelectronics and near-field sensors [5, 6, 7], plasmonics hence offers rich perspectives for quantum optics with single plasmons [8], and for designing novel broadband single photon sources based on plasmonic waveguide and plasmon based antennas. Several groups have started to pursue plasmonic systems for quantum optics [9, 8, 10, 11]. Plasmonic systems can provide strong interaction with single quantum dots and single molecules without resorting to ultra narrow-band high-Q structures. For instance, several researchers recently proposed that broadband highly directional single-photon sources can be made using plasmon particle array antennas that mimic directional radio frequency antennas [12, 13, 14, 15].

The thesis concerns the theoretical study of optical plasmons mediated light-matter interaction [11, 16, 17]. Two types of plasmonic effects on spontaneous emission, i.e., freely propagating surface plasmon polaritons (SPPs) and localized

plasmonic resonance are addressed. We study the coupling between a quantum emitter and the freely propagating SPPs in the context of developing efficient and coherent single-photon sources. A 3-dimensional (3D) finite element method (FEM) model is developed. We also study the emitter coupled to free space photons, mediated by plasmon nanoantennas.

This thesis is organized as follows. Chapter 2 outlines the basic concepts that are necessary to discuss the physics and modeling techniques. In Chapter 3, several numerical techniques are presented. A FEM model of calculating the total decay rate and coupling efficiency of a quantum emitter coupled to plasmonic waveguides is detailed. Also the point dipole approximation and a multipoles expansion based multiple scattering approach are briefly discussed. In Chapter 4, we numerically investigate the coupling efficiency of a single self-assembled quantum dot to a metallic slot waveguide in the presence of leaky plasmonic modes. We show that the inhomogeneity of the dielectric environment has serious impact on the coupling efficiency, we further show that by decreasing the index contrast within experimental bounds, we can gain a factor of 2 in the coupling efficiency of the single optical plasmon generation. In Chapter 5, we briefly discuss the basic concepts used for radio wave antenna. We construct an optical Yagi-Uda nanoantenna that yields direction emission, based on the recipe of a radio wave antenna. We also propose a plasmon-based reconfigurable antenna to controllably distribute emission from a single quantum emitter in spatially separated channels. Based on engineering the dispersion relations of plasmon chains, we predict that beam can be switched on and off by switching the host refractive index. A short summary of the conclusions and an outlook are given in Chapter 6.

Chapter 2

Spontaneous emission, local density of states and dispersion relation

2.1 Introduction: ultimate control over light quanta

The concept of light quanta was introduced by Planck to explain the black-body radiation spectrum in the beginning of the 20s century, which initiates the era of quantum mechanics. This pioneering work led Einstein to introduce the photon concept to explain the photoelectric effect. Throughout the 20s century, the quantum nature of light was extensively and thoroughly studied in a variety of quantum optical systems, including resonance florescence, lasers, micromasers, squeezed states and atom optics. On one hand, quantum optics provides a powerful probe for addressing fundamental issues. On the other hand, it also holds promise for new devices and new technologies, i.e., quantum computers and quantum cryptography.

At the turn of the 21st century, exploration of quantum computers and quantum networks is in fashion. All the fantastic technologies rely on the ultimate control over light quanta. The interaction of a single two-level atom and a single quantized radiation mode is a central concept in the textbook of quantum optics in the last century. Due to the advance of ion-trap and fabrication of high-finesse optical cavities, there has been tremendous progresses on cavity quantum electrodynamic (CQED) in the past decade, which pushes the light-matter interaction to the limits

of the single-photon-single-atom level [18, 19, 20]. The ultimate control over a single light quantum is core of CQED, which has been extensively studied both in theory and experiment based on different photonic systems recently, and will continue to attract attention in the future.

In the framework of single-photon-single-atom interaction, there are two physically distinct regimes, namely the strong and weak coupling regimes. In the strong coupling regimes, the single-photon-single-atom coupling is stronger than the dissipation of atomic exciton and photon leakage, so that the excitation between the single atom and photonic mode becomes reversible (Rabi oscillations) [19]. In the weak coupling regime, the spontaneous emission (SE) rate of the atom is modified, as compared to vacuum. This phenomenon is referred to as the Purcell effect [21]. The strong coupling of single-photon-single-emitter constitutes an essential ingredient of a number of quantum computation operations, i.e., quantum state transfer, entanglement distribution, controlled phase gates and so on. At the same time, the physical insights of the single-photon-single-emitter system in the weak coupling regime can lead to new possibilities to boost the efficiency of optoelectronic devices, i.e., single-photon sources, low threshold lasers, and LED-lightening.

Meanwhile, the rapid progress in photonics in the past decades provides many options to manipulate light at very advanced levels, such as photonic crystals [22, 23, 24, 25], plasmonics [26, 27, 5, 6, 7], and metamaterials[28, 29, 30]. The major part of the work aforementioned above in the field focuses on the properties described by electromagnetic theory, still some pioneering work on manipulation of light-matter at single-photon-single-atom level were achieved. In particular, it has recently been proposed and experimentally demonstrated that a single quantum emitter can be efficiently coupled to surface plasmon polaritons [8, 9]. Inspired by this idea, we explore how surface plasmon polaritons can be used to enhance the light-matter interaction. Specially, we model the plasmonic effects to control the single photon emission for developing single photon devices.

2.2 Spontaneous emission

2.2.1 Purcell effect and some history

Spontaneous emission is the process of an initial quantum mechanical state spontaneously decaying into a continuum of final states, which can be applicable for many quantum mechanical systems. Throughout the thesis, we concentrate on the

interaction between light and matter. Spontaneous emission is one of the most prominent effects in the interaction of atoms with radiation, and its explanation has to resort to the fully quantized theory for both the atom and the light. In practice, the spontaneous emission has been interpreted as stimulated emission induced by virtual photons due to vacuum fluctuations. However, the explanation may also lead to "spontaneous absorption" if one is aware that the stimulated emission and absorption have equal Einstein B coefficients [31]. Such dilemma has been resolved by the prescription provided by Dalibard and his coworkers [32, 33]. They argued that radiation reaction and vacuum fluctuations contribute to the spontaneous emission equally for an excited atom at rest, while for an atom in the ground state, the two contributions cancel precisely. It is the balance between vacuum fluctuations and radiation reaction that inhibits transitions from the ground state and ensures its stability.

It has long been realized that the spontaneous emission rate is not an intrinsic property of a quantum emitter itself [21]. The general explanation is that the spontaneous emission rate depends on the transition strength between the upper and lower level of the quantum emitter as well as the local density of optical states. The local density of states (LDOS) measures the available number of electromagnetic modes into which the photons can be emitted at a specific location of the emitter, and can be manipulated by tailoring the photonic environment of the emitter. A number of structures such as interfaces [34, 35], cavities [36, 1], photonic crystals [23, 37] and waveguides [38, 39] have already been used to modify the spontaneous emission rate. Apart from fundamental studies, engineering the spontaneous emission rate of a quantum emitter may improve the efficiency of optoelectronic devices, i.e., single-photon sources, low threshold lasers, and LED-lightening.

As an alternative to dielectric materials, the spontaneous emission rate can be manipulated by subwavelength metallic systems, which support surface plasmon polaritons. Surface plasmon polaritons are electromagnetic excitations associated with charge density waves on the surface of a conducting object. The tight confinement of the electromagnetic field to the metal-dielectric interface due to the boundary condition constraints gives the possibility of inventing new ways to enhance light-matter interaction, such as efficient single optical plasmon generation [8, 9], single molecule detection with surface-enhanced Raman scattering [40, 41], enhanced photoluminescence from quantum wells [42], and nanoantenna modified spontaneous emission [43, 44, 45].

Although limited by the intrinsic losses of the metals in the optical frequency

range, different metallic structures have been extensively studied in the last few years due to the possibilities of integration and miniaturization. The dramatic enhancement of the field intensity due to the field concentration and geometric slowing down of the mode propagation provides an excellent platform to study single photon nonlinear optics [46] and light matter interaction at the single-emitter-single-photon level. There are also considerable interests in surface plasmons for sub-wavelength optics and applications in sensing, near field imaging, waveguiding and switching below the diffraction limit [26, 27, 5, 6, 7]. The study of plasmonic effects to enhance light-matter interaction and the preferential spontaneous emission from, e.g., a quantum dot into a desired mode is currently a hot research topic. It is important for solid-state quantum information devices as well as for improving our understanding of light-matter interaction at the nanoscale. There are also theoretical investigations on this topic [9, 47], with simplified assumptions that limit their applicability for analyzing realistic structures, e.g. by assuming geometrical shapes that are not readily achievable using current fabrication technology and making assumptions that are only valid at some length scales. The realistic description of all competing, radiative and non-radiative, decay channels for an emitter placed in close proximity to a plasmonic waveguide of general geometry is important in order to understand the physics and the fundamental limitations.

2.2.2 Fermi's Golden rule

Spontaneous emission is a purely quantum mechanical phenomenon, which stems from the vacuum fluctuation of the electromagnetic field as well as the radiation reaction. In the semi-classical picture, vacuum fluctuations are phenomenologically added as a harmonic perturbation, which accounts for the transition of the quantum emitter from the excited state to a continuum of final states, as sketched in Fig. 2.1. We consider a combined "atom+field" states, and calculate the transitions from the excite state $|i\rangle$ with the energy of E_i to a set of final states $|f\rangle$ with identical energy of E_f. The final states differ only by the mode wavevector $\boldsymbol{k}$, which is used as a model label to uniquely characterize a specific mode together with the polarization vector of the radiation field. By employing first order perturbation theory, one can use Fermi's Golden Rule [48] to calculate the decay rate of a quantum emitter,

$$\gamma = \frac{2\pi}{\hbar^2}\sum_f |\langle f|\hat{H}_i|i\rangle|^2 \delta(\omega_i - \omega_f), \tag{2.1}$$

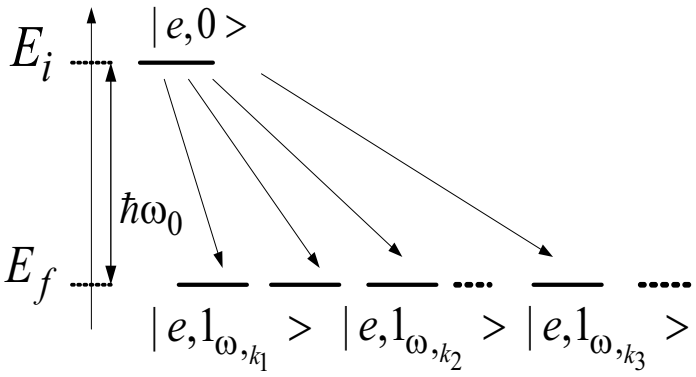

Figure 2.1: Transition from an initial state $|i\rangle = |e,0\rangle$ to a set of final states $|f\rangle = |g,1_{\omega,\boldsymbol{k}}\rangle$. The states are products of atomic states ($|e\rangle$ or $|g\rangle$) and single-photon states ($|0\rangle$ or $|1_{\omega,\boldsymbol{k}}\rangle$).

where $\hat{H}_i = -\hat{\boldsymbol{\mu}} \cdot \hat{\boldsymbol{E}}$ is the interaction Hamiltonian in the dipole approximation. One can represent the single photon electric field operator $\hat{\boldsymbol{E}}$ at $\boldsymbol{r} = \boldsymbol{r}_0$ as,

$$\hat{\boldsymbol{E}} = \sum_{\boldsymbol{k}} [\boldsymbol{E}_{\boldsymbol{k}} \hat{a}_{\boldsymbol{k}} e^{-i\omega_{\boldsymbol{k}} t} + \boldsymbol{E}^*_{\boldsymbol{k}} \hat{a}^\dagger_{\boldsymbol{k}} e^{i\omega_{\boldsymbol{k}} t}], \tag{2.2}$$

where $\boldsymbol{E}_{\boldsymbol{k}}$ ($\boldsymbol{E}^*_{\boldsymbol{k}}$) is the spatially dependent complex field at positive (negative) frequencies, and $\hat{a}_{\boldsymbol{k}}$ ($\hat{a}^\dagger_{\boldsymbol{k}}$) is the annihilation (creation) operator. Assuming all the different mode $\boldsymbol{k}$ occupy the same mode volume V, the normalization factor takes the following form [48],

$$\int_V \varepsilon_0 E_{\boldsymbol{k}} \cdot E^*_{\boldsymbol{k}} dv = 1/2\hbar\omega_0. \tag{2.3}$$

The factor 1/2 in Eq. (2.3) is due to the fact that the magnetic field also stores half of the electromagnetic energy. Substituting the explicit form of the electric field (Eq. (2.2)) into Eq. (2.1), one can obtain,

$$\gamma = \frac{2\pi}{\hbar^2} \sum_{\boldsymbol{k}} [\boldsymbol{\mu} \cdot (\boldsymbol{E}_{\boldsymbol{k}} \boldsymbol{E}^*_{\boldsymbol{k}}) \cdot \boldsymbol{\mu}] \delta(\omega_{\boldsymbol{k}} - \omega_0) \tag{2.4}$$

To factorize the transition rate in an 'atom part' and a position dependent 'field part', we rewrite the expression of the spatially dependent complex field $\boldsymbol{E}_{\boldsymbol{k}}$ for the single photon in terms of normal modes $\boldsymbol{u}_{\boldsymbol{k}}$ defined as,

$$\boldsymbol{E}_{\boldsymbol{k}} = \sqrt{\tfrac{\hbar\omega_{\boldsymbol{k}}}{2\varepsilon_0}} \boldsymbol{u}_{\boldsymbol{k}}, \quad \boldsymbol{E}^*_{\boldsymbol{k}} = \sqrt{\tfrac{\hbar\omega_{\boldsymbol{k}}}{2\varepsilon_0}} \boldsymbol{u}^*_{\boldsymbol{k}}. \tag{2.5}$$

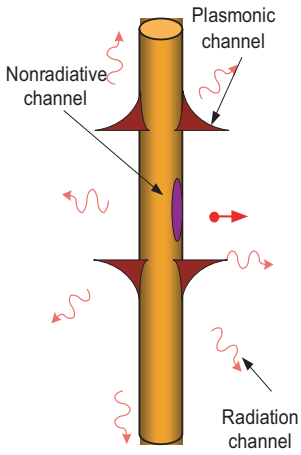

Figure 2.2: Different emission channels involved in the decay process of a quantum emitter (red dot) coupled to a plasmonic waveguide. In the radiation channel the emitted photons are traveling in free space. In the plasmonic channel the plasmonic modes are excited and guided by the metallic nanowire. In the non-radiative channel, electron-hole pairs are generated.

We hence reformulate the spontaneous emission as follows,

$$\gamma = \frac{\pi\omega}{3\hbar\varepsilon_0}|\boldsymbol{\mu}|^2\rho_\mu(\boldsymbol{r}_0,\omega_0), \tag{2.6}$$

where $\rho_\mu(\boldsymbol{r}_0,\omega_0) = 3\sum_{\boldsymbol{k}}[\boldsymbol{n}_\mu\cdot(\boldsymbol{u}_{\boldsymbol{k}}\boldsymbol{u}_{\boldsymbol{k}}^*)\cdot\boldsymbol{n}_\mu]\delta(\omega_{\boldsymbol{k}}-\omega_0)$ is referred to the projected local density states [48], which measures the available number of electromagnetic modes for a dipole located at r_0 with orientation of $\boldsymbol{n}_\mu$. One also notes that $\boldsymbol{u}_{\boldsymbol{k}}\boldsymbol{u}_{\boldsymbol{k}}^*$ denotes the outer product, which produces a dyad.

2.2.3 Multiple decay channels and spontaneous emission β factor

As shown in Fig. 2.2, we consider an ideal quantum emitter coupled to a plasmonic waveguide. The excitation energy of the quantum emitter can be dissipated either radiatively or non-radiatively. Radiative relaxation is associated with the emission of a photon, whereas non-radiative relaxation can be various pathways such as coupling to vibrations, resistive heating of the environment, or quenching by other quantum emitters. The resistive heating of the metallic waveguide is the

only mechanism of non-radiative relaxation considered in our model. The quantum emitter is positioned in the vicinity of the metallic nanowire, thus there are three channels for the quantum emitter to decay into, i.e., the radiative channel, the plasmonic channel, and the non-radiative channel. The corresponding decay rates are denoted by γ_{rad}, γ_{pl}, and γ_{nonrad}, respectively. The radiative channel accounts for the spontaneous emission in the form of far field radiation. The plasmonic channel is the excitation of the plasmonic mode, which is guided by the plasmonic waveguide. The non-radiative channel is associated with the resistive heating of the lossy metals, which is due to electron-hole generation inside the metals. The spontaneous emission β factor is defined by $\beta = \frac{\gamma_{pl}}{\gamma_{total}}$, where γ_{total} is the sum of the three rates, $\gamma_{total} = \gamma_{rad} + \gamma_{nonrad} + \gamma_{pl}$. The β factor gives the probability that the quantum emitter excites a single plasmonic mode.

In order to achieve a larger β factor, one needs to be aware that the local plasmon resonances in the transverse plane of the plasmonic waveguides may be excited according to Mie's theory, which could substantially contribute to spontaneous emission of the quantum emitter and subsequently scatter the emission out of the structure. Hence, in our case such localized plasmonic resonances in the transverse plane need to be suppressed. In chapter 2 and 3, we will concentrate on the regime where the geometric sizes in the transverse plane are far away from the localized resonance conditions, in order to achieve an efficient coupling between the emitter and the freely propagating plasmonic modes.

2.3 Light scattering and dyadic Green's function

2.3.1 Electromagnetic theory of light

Light lies at the special range in the spectrum of electromagnetic radiation, coincided with the atomic transitions in matter. Complete description of light has to incorporate the wave-particle duality of its nature, in which light manifests itself in the form of waves or particles. Nevertheless, the electromagnetic theory forms the necessary basis of interpreting light, which is also the foundation to explore the

quantum nature of light. Hence, we start with Maxwell's equations

$$\nabla \times \boldsymbol{E}(\boldsymbol{r},t) = -\frac{\partial \boldsymbol{B}(\boldsymbol{r},t)}{\partial t}, \tag{2.7a}$$

$$\nabla \times \boldsymbol{H}(\boldsymbol{r},t) = \frac{\partial \boldsymbol{D}(\boldsymbol{r},t)}{\partial t} + \boldsymbol{j}(\boldsymbol{r},t), \tag{2.7b}$$

$$\nabla \cdot \boldsymbol{D}(\boldsymbol{r},t) = \rho(\boldsymbol{r},t), \tag{2.7c}$$

$$\nabla \cdot \boldsymbol{B}(\boldsymbol{r},t) = 0, \tag{2.7d}$$

where $\boldsymbol{E}$ denotes the electric field, $\boldsymbol{D}$ the electric displacement, $\boldsymbol{H}$ the magnetic field, $\boldsymbol{B}$ the magnetic inductions, $\boldsymbol{j}$ the current density, and ρ the charge density. The constitutive relations for a non-magnetic, non-dispersive linear and isotropic dielectric composite are

$$\boldsymbol{D} = \varepsilon_0 \varepsilon(\boldsymbol{r}) \boldsymbol{E}, \tag{2.8a}$$

$$\boldsymbol{B} = \mu_0 \boldsymbol{H}, \tag{2.8b}$$

It it well known that Eq. (2.7) combined with Eq. (2.8) will yield a wave equation for, *e.g.*, the electric field $\boldsymbol{E}$

$$\nabla \times \nabla \times \boldsymbol{E}(\boldsymbol{r}) - k_0^2 \varepsilon(\boldsymbol{r}) \boldsymbol{E}(\boldsymbol{r}) = i\omega\mu_0 \boldsymbol{j}(\boldsymbol{r}), \tag{2.9}$$

assuming harmonic time dependence which, be specific with frequency ω, with $k_0 = \omega/c$ denoting the vacuum wavenumber. Throughout the thesis, $\varepsilon(\boldsymbol{r})$ is the complex dielectric constant at frequency ω.

2.3.2 Dyadic Green's function and local density of states

The solutions to many problems in electromagnetics can be obtained by solving the second-order uncoupled partial differential equation, i.e., the wave equation defined by Eq. (2.9), with appropriate boundary conditions. Alternatively, one can calculate the solution to Eq. (2.9) for a driving source constituting a point source (impulse, Dirac delta function). Using the principle of linear superposition implied by the linearity of wave equation, one hence can obtain the solution to a general source by convoluting the point source solution with a real source. The point source solution is called the Green's function, and the method is denoted the Green's function method. In engineering terminology, the Green's function is the impulse response of a system, which is also called the transfer function in system theory. Due to the fact that the electric field is a vector, the Green's function for the wave equation is

a dyad, and is called as dyadic Green's function throughout the thesis. The electric dyadic Green's function $\bar{\boldsymbol{G}}(\boldsymbol{r}, \boldsymbol{r}', \omega)$ is defined by

$$[\nabla \times \nabla \times -k_0^2 \varepsilon(\boldsymbol{r})]\bar{\boldsymbol{G}}(\boldsymbol{r}, \boldsymbol{r}', \omega) = \bar{\boldsymbol{I}}\delta(\boldsymbol{r} - \boldsymbol{r}'), \tag{2.10}$$

where $\bar{\boldsymbol{I}}$ is the unit dyad. The electric field induced by a current source $\boldsymbol{j}(\boldsymbol{r})$ is equal to the convolution of the dyadic Green's function with $\boldsymbol{j}(\boldsymbol{r})$,

$$\boldsymbol{E}(\boldsymbol{r}) = i\omega\mu_0 \int_V \bar{\boldsymbol{G}}(\boldsymbol{r}, \boldsymbol{r}', \omega)\boldsymbol{j}(\boldsymbol{r}')d\boldsymbol{r}'. \tag{2.11}$$

Apart from the field excitation due to a current source, scattering of light from inhomogeneities can also be presented as an integral equation where the kernel is the dyadic Green's function [49]. Considering a number of scattering sites embedded in a background medius described by $\varepsilon_B(\boldsymbol{r})$, the variation in permittivity compared with the background is $\triangle\varepsilon(\boldsymbol{r}) = \varepsilon(\boldsymbol{r}) - \varepsilon_B(\boldsymbol{r})$. Subsequently, the wave equation in the absence of any source currents and charges can be reformulated as,

$$\nabla \times \nabla \times \boldsymbol{E}(\boldsymbol{r}) - k_0^2 \varepsilon_B(\boldsymbol{r})\boldsymbol{E}(\boldsymbol{r}) = i\omega\mu_0 \boldsymbol{j}_e(\boldsymbol{r}), \tag{2.12}$$

where $\boldsymbol{j}_e = -i\omega\varepsilon_0 \triangle\varepsilon(\boldsymbol{r})\boldsymbol{E}(\boldsymbol{r})$ is the volume distribution of the induced electric current density. In the presence of an incident field of $\boldsymbol{E_0}(\boldsymbol{r})$, the total field consisting of the incident field and the scattered field can be presented as

$$\boldsymbol{E}(\boldsymbol{r}) = \boldsymbol{E_0}(\boldsymbol{r}) + k_0^2 \int_V \bar{\boldsymbol{G}}(\boldsymbol{r}, \boldsymbol{r}', \omega)\triangle\varepsilon(\boldsymbol{r}')\boldsymbol{E}(\boldsymbol{r}')d\boldsymbol{r}', \tag{2.13}$$

where $\bar{\boldsymbol{G}}(\boldsymbol{r}, \boldsymbol{r}', \omega)$ denotes the dyadic Green's function for the background medium. The electric field $\boldsymbol{E}(\boldsymbol{r})$ in Eq. (2.13) is implicit, the Eq. (2.13) is conventionally referred as Lippmann-Schwinger equation [49]. Several variants of scattering theory based on Eq. (2.12) were successfully applied to model near-field optical phenomena and nanophotonic devices [50, 51, 52, 53, 54]. The purpose of such models is to predict the fundamental state of the electromagnetic waves called local density of states (LDOS). The imaginary part of the dyadic Green's function evaluated at its origin ($\mathtt{Im}\{G\}$) is proportional to LDOS [48], the computation of which is an underlying theme in modeling nano-photonic devices. The aforementioned normal modes bridge the gap between the dyadic Green's function and LDOS, and the norm modes are defined as follows,

$$\nabla \times \nabla \times \boldsymbol{u_k}(\boldsymbol{r}, \omega_{\boldsymbol{k}}) - k_0^2 \varepsilon(\boldsymbol{r})\boldsymbol{u_k}(\boldsymbol{r}, \omega_{\boldsymbol{k}}) = 0, \tag{2.14}$$

with the orthogonality relation and the completeness relation satisfying

$$\int_V \boldsymbol{u}_{\boldsymbol{k}}(\boldsymbol{r},\omega_{\boldsymbol{k}})\cdot\boldsymbol{u}^*_{\boldsymbol{k}'}(\boldsymbol{r},\omega_{\boldsymbol{k}'})dV=\delta_{\boldsymbol{k}\boldsymbol{k}'}, \tag{2.15a}$$

$$\sum_{\boldsymbol{k}}\boldsymbol{u}_{\boldsymbol{k}}(\boldsymbol{r},\omega_{\boldsymbol{k}})\cdot\boldsymbol{u}^*_{\boldsymbol{k}}(\boldsymbol{r}',\omega_{\boldsymbol{k}})=\bar{\boldsymbol{I}}\delta(\boldsymbol{r}-\boldsymbol{r}'). \tag{2.15b}$$

Resting on the orthogonality relation and completeness relation, one could construct the dyadic Green's function accordingly [48],

$$\bar{\boldsymbol{G}}(\boldsymbol{r},\boldsymbol{r}',\omega)=\sum_{\boldsymbol{k}}c^2\frac{\boldsymbol{u}^*_{\boldsymbol{k}}(\boldsymbol{r}',\omega_{\boldsymbol{k}})\boldsymbol{u}_{\boldsymbol{k}}(\boldsymbol{r},\omega_{\boldsymbol{k}})}{\omega^2_{\boldsymbol{k}}-\omega^2_0}. \tag{2.16}$$

To proceed with the help from complex contour integration one can further prove $\mathtt{Im}\{G\}$ as follows,

$$\mathtt{Im}[\bar{\boldsymbol{G}}(\boldsymbol{r},\boldsymbol{r}',\omega)]=\frac{\pi c^2}{2\omega}\sum_{\boldsymbol{k}}\boldsymbol{u}_{\boldsymbol{k}}(\boldsymbol{r},\omega_{\boldsymbol{k}})\cdot\boldsymbol{u}^*_{\boldsymbol{k}}(\boldsymbol{r}',\omega_{\boldsymbol{k}})\delta(\omega_0-\omega_{\boldsymbol{k}}) \tag{2.17}$$

Then the projected LDOS can be calculated from the dyadic Green's function accordingly,

$$\rho_\mu(\boldsymbol{r}_0,\omega_0)=\frac{6\omega_0}{\pi c^2}[\boldsymbol{n}_\mu\cdot\mathrm{Im}\{\bar{\boldsymbol{G}}(\boldsymbol{r}_0,\boldsymbol{r}_0;\omega_0)\}\cdot\boldsymbol{n}_\mu]. \tag{2.18}$$

2.3.3 Quantization of light: a multiple modes scheme

The essence of the quantum theory of light is to associate a quantized simple harmonic oscillator to each mode of the radiation field, labeled by $\alpha=\{\boldsymbol{k},\lambda\}$, which consists of indices for wave vector $\boldsymbol{k}$ and polarization vector λ [55]. The destruction and creation operator, initially defined for a quantum mechanical harmonic oscillator, can be applied for mode α and takes the following forms,

$$\hat{a}_\alpha\left|n_\alpha\right\rangle=n_\alpha^{1/2}\left|n_\alpha-1\right\rangle, \tag{2.19a}$$

$$\hat{a}^\dagger_\alpha\left|n_\alpha\right\rangle=(n_\alpha+1)^{1/2}\left|n_\alpha+1\right\rangle. \tag{2.19b}$$

Different modes are independent, and their associated operators commute, so the basic commutation relation is generalized as

$$[\hat{a}_\alpha,\hat{a}^\dagger_{\alpha'}]=\delta_{\alpha,\alpha'}. \tag{2.20}$$

The physical electric field is real, and a monochromatic field can be written as

$$\boldsymbol{E}(\boldsymbol{r},t)=\frac{1}{2}[\boldsymbol{E}(\boldsymbol{r})e^{-i\omega t}+\boldsymbol{E}^*(\boldsymbol{r})e^{i\omega t}], \tag{2.21}$$

Due to its measurable properties, the electric field is reformulated as a Hermitian operator, with positive and negative frequency part corresponding to the destruction and creation operator, respectively. Following the Loudon [31], the complete electric field operator is

$$\hat{\boldsymbol{E}}(\boldsymbol{r},t)=\sum_{\alpha}\boldsymbol{e}_{\alpha}(\hbar\omega_{\alpha}/2\varepsilon_{0}V)^{1/2}[\hat{a}_{\alpha}e^{-i\chi_{\alpha}(\boldsymbol{r},t)}+\hat{a}_{\alpha}^{\dagger}e^{i\chi_{\alpha}(\boldsymbol{r},t)}] \tag{2.22}$$

where $\boldsymbol{e}_{\alpha}$ denotes the unit polarization vectors, V the mode volume, and $\chi_{\alpha}(\boldsymbol{r},t)=(\omega_{\alpha}-\boldsymbol{k}\cdot\boldsymbol{r}-\pi/2)$ is defined as the phase angle for the mode α. The Hamiltonian of the radiation field is obtained by summation of the harmonic-oscillator (modes) contributions,

$$\hat{H}=\sum_{\alpha}\hbar\omega_{\alpha}(\hat{a}_{\alpha'}^{\dagger}\hat{a}_{\alpha}+\frac{1}{2}). \tag{2.23}$$

2.3.4 Rate of energy dissipation of a classical dipole

"Weak coupling regime" is a terminology used in quantum electrodynamics, whose counterpart in classic electrodynamics is the oscillating dipole with negligible damping introduced by the radiation reaction force. The classical theory will not give the right result for the spontaneous decay rate [1], nevertheless, the transition rate is well modeled by the damping dipole when it is correctly normalized [48].

According to Eq. (2.7), we can obtain the following for a non-magnetic material with some simple algebra,

$$\begin{aligned}&\int_{\partial V}(\boldsymbol{E}\times\boldsymbol{H})\cdot\boldsymbol{n}da+\frac{1}{2}\frac{\partial}{\partial t}\int_{\partial V}(\boldsymbol{D}\cdot\boldsymbol{E}+\boldsymbol{B}\cdot\boldsymbol{H})dV\\&=-\int_{V}(\boldsymbol{j}^{\star}\cdot\boldsymbol{E})dV-\frac{1}{2}\int_{V}(\boldsymbol{E}\cdot\frac{\partial\boldsymbol{P}}{\partial t}-\boldsymbol{P}\cdot\frac{\partial\boldsymbol{E}}{\partial t})dV,\end{aligned} \tag{2.24}$$

where ∂V denotes the surface that encloses the volume V, and $\boldsymbol{n}$ denotes the outward unit normal vector to the surface ∂V. $P=\varepsilon_{0}\chi_{e}\boldsymbol{E}$ is the macroscopic polarization with the electric susceptibility of χ_{e}. The left hand sides are the total change of electromagnetic energy, including the net energy flow in or out of the volume V (first term on the left side) and the time rate of change of electromagnetic energy inside V (second term on the left side). The sum of all the terms on the right side are equal to the rate of the energy dissipation and can be considered to be the energy source or energy sink. If the medium is linear, the last term on the right side equals zero, and the only term accounting for the energy dissipation is $\boldsymbol{j}^{\star}\cdot\boldsymbol{E}$.

[1] The classical decay rate gives half the quantum decay rate.

Eventually the current term $\boldsymbol{j}$ can be formulated in terms of an oscillating dipole, as explained in the following.

For a harmonic time dependent field in the linear medium, Eq. (2.24) can be simplified to,

$$\int_{\partial V} < \boldsymbol{S} > \cdot \boldsymbol{n} da = -\frac{1}{2} \int_{V} \mathrm{Re}(\boldsymbol{j}^{\star} \cdot \boldsymbol{E}) dV, \tag{2.25}$$

where the term on the right hand side defines the mean energy dissipation with volume V. $\langle S \rangle$ represents the time average of the Poynting vector: $\langle \boldsymbol{S} \rangle = \frac{1}{2}\mathrm{Re}(\boldsymbol{E} \times \boldsymbol{H}^{\star})$. Replacing the current term $\boldsymbol{j}$ by a dipole current current density $\boldsymbol{j}(r) = -i\omega\boldsymbol{\mu}\delta(r - r_0)$, one obtains the relationship between the power flux and the emission or absorption rate for a dipole source,

$$\frac{dW}{dt} = -\frac{\omega}{2} \mathtt{Im}\{\boldsymbol{\mu}^{\star} \cdot \boldsymbol{E}(r_0)\}, \tag{2.26}$$

where $\boldsymbol{\mu}$ is the dipole moment of the point source, which can be any two level system that emits and absorbs light, such quantum dots, molecules.

Using Eq. (2.26), one can calculate the decay rate of an emitting dipole in an inhomogeneous environment, such as a quantum dot in a photonic crystal cavity. The field can be decomposed into two components, one is the field without the influence of the inhomogeneous environment, the other one is the reflected field induced by the inhomogeneity of the environment:

$$\boldsymbol{E}(r_0) = \boldsymbol{E}_0(r_0) + \boldsymbol{E}_s(r_0). \tag{2.27}$$

Here $\boldsymbol{E}_0(r_0)$ and $\boldsymbol{E}_s(r_0)$ are the primary dipole field and the scattered field, respectively. Accordingly, we can split the energy dissipation rate $P = dW/dt$ into two parts. The contribution of $\boldsymbol{E}_0(r_0)$ is the decay rate of the dipole in the homogeneous medium [48], and is given as follows,

$$P_0 = \frac{|\boldsymbol{\mu}|^2}{12\pi} \frac{\omega}{\varepsilon\varepsilon_0} k^3, \tag{2.28}$$

which can be used to normalize the total rate of the energy dissipation,

$$\frac{P}{P_0} = 1 + \frac{6\pi\varepsilon\varepsilon_0}{|\boldsymbol{\mu}|^2} \frac{1}{k^3} \mathtt{Im}\{\boldsymbol{\mu}^{*} \cdot \boldsymbol{E}_s(r_0)\}. \tag{2.29}$$

The same result can also be derived by considering both the undriven harmonically oscillating dipole and the driven harmonically oscillating dipole in classical picture [48, 56]. An important relationship collects the classical picture and the quantum picture is the following,

$$\frac{\gamma}{\gamma_0} = \frac{P}{P_0}, \tag{2.30}$$

where γ is the decay rate in the photonic environment, and γ_0 are the decay rate in vacuum. Finally we have the correct expression for the decay rate of the dipole in an inhomogeneous environment,

$$\frac{\gamma}{\gamma_0} = 1 + \frac{6\pi\varepsilon\varepsilon_0}{|\vec{\mu}|^2}\frac{1}{k^3}\mathtt{Im}\{\boldsymbol{\mu}^* \cdot \boldsymbol{E}_s(r_0)\}. \tag{2.31}$$

2.4 Surface plasmon polaritons

2.4.1 Overview of surface plasmon polaritons

Surface plasmon polaritons (SPPs) are electromagnetic excitations in association with charge density waves on the surface of metals, the existence of which is characteristic of the interaction of metallic structures with light. The interaction of metals with electromagnetic fields is primarily determined by the free conduction electrons in the metals, and essentially governed by the macroscopic Maxwell equations.

Due to the free electron behavior inside the metals, SPPs possess two main features, i.e., the tight confinement of electromagnetic waves, even below the diffraction limit, and the pronounced field enhancement [57]. The theoretical foundations of SPPs, a particular type of surface wave, was established around 1900 in the context of radio waves propagating along the surface of a conductor with finite conductivity [58, 59]. Throughout the 20th century, SPPs have been rediscovered in different contexts. However, the unique properties of SPPs and the possible applications were far from appreciated until the end of 20th century, in accordance with the advance of nano-technology as well as the approaching to fundamental physical limits of some crucial technological areas, such as optical lithography, optical data storage, high electronics manufacturing and so on.

Especially in recent years, a flurry of activity in fundamental research and development of surface plasmon based structures and devices is going on, ranging from the freely propagating SPPs to localized SPPs [60]. The tight confinement of the electromagnetic field of SPPs enables to manipulate and route "light" on the nano meter scale which is far below the diffraction limit, such as light guiding [7], enhanced optical transmission [61] and high resolution optical image [60, 48]. Meanwhile, the field enhancement due to the small mode volume opens new ways to enhance light-matter interactions, which might have potential applications in energy harvesting [62] or biosensing [63]. Different metallic structures have been extensively studied in the last few years due to the possibilities of integration and miniaturization, though limited by the intrinsic losses of the metals in the opti-

cal frequency range. The dramatic enhancement of the field intensity due to the field concentration and geometric slowing down of the mode propagation provides an excellent platform to study single photon nonlinear optics [46] and light matter interaction at the single-emitter-single-photon level. The thesis will be solely concentred on the single photon emission by a single quantum emitter, which is mediated by optical plasmons.

2.4.2 Drude model

The basic optical properties of metals can be obtained by a complex dielectric function from so-called Drude model theory [64]. The Drude model developed in 1900 is based on the kinetic gas theory, which assumes a gas of non-interacting free electrons that have an effective mass m_e and a damping term γ. The equation of motion for the free electrons gas subjected to external electric field $\boldsymbol{E}_0 e^{-i\omega t}$ is

$$m_e \frac{\partial^2 \boldsymbol{r}}{\partial^2 v} + m_e \gamma \frac{\delta \boldsymbol{r}}{\delta x} = e\boldsymbol{E}_0 e^{-i\omega t}, \tag{2.32}$$

where m_e and e are the effective mass and the charge of the free electrons. A typical solution to Eq. (2.32) can be formulated as $\boldsymbol{r} = \boldsymbol{r}_0 e^{-i\omega t}$. The accumulation of the induced dipole moment $\boldsymbol{\mu}$ of the free electrons gives a macroscopic polarization per unit volume $\boldsymbol{P} = n\boldsymbol{\mu}$, where n is the number of the electrons per unit volume. The constitutive relation [65] also gives $\boldsymbol{P} = \varepsilon_0(\varepsilon(\omega) - 1)\boldsymbol{E}_0 e^{-i\omega t}$. With simple algebra, one obtains the following results,

$$\varepsilon_{Drude}(\omega) = 1 - \frac{\omega_p^2}{\omega^2 + i\gamma\omega}, \tag{2.33}$$

where $\omega_p = \sqrt{ne^2/(m_e\varepsilon_0)}$ is the volume plasmon frequency. Equation (2.33) can be split into the real part and imaginary part,

$$\varepsilon_{Drude}(\omega) = 1 - \frac{\omega_p^2}{\omega^2 + \gamma^2} + i\frac{\gamma\omega_p^2}{\omega(\omega^2 + \gamma^2)}. \tag{2.34}$$

As a classical model, the Drude model captures the main features of interaction between metals and light, with a remarkable accuracy of the optical properties of metals in the infrared regime. For high frequencies in the visible range, the response of the bound electrons, i.e., the interband transitions, might need to be included. Nonetheless, for many metals at optical frequencies the Drude model generally gives quite accurate results for the optical properties, as compared with experiments. Similar behavior is not reproducible in other spectral ranges using the scale

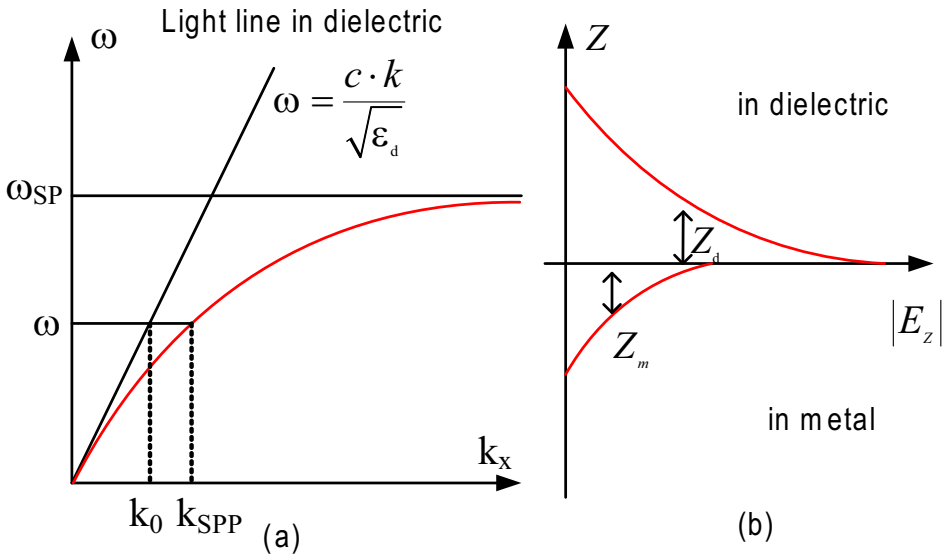

Figure 2.3: (a) The dispersion relation of SPPs at a metallic-dielectric interface. (b) The field profiles of the E_z component of the SPP in the metals and dielectric. Z_m (Z_d) is the penetration length (field amplitude $1/e$ length) in the metals (dielectrics).

invariance of Maxwell's equations, since material parameters change considerably with frequency.

2.4.3 SPPs on a flat metal-dielectric interface

The simplest plasmon based device is a flat metallic-dielectric interface, at which the evanescent electromagnetic waves coupled to coherent oscillations of free charges at the metal surface can be supported. Assuming that the interface is normal to z and the SPPs propagate along the x direction, the dispersion relation of such surface bound SPP waves, which relates the real part of wave vector k_x and the optical frequency ω, is given by [64],

$$k_x = k_0 \sqrt{\frac{\varepsilon_d \varepsilon_m}{\varepsilon_d + \varepsilon_m}}, \tag{2.35}$$

where ε_d and ε_m are the dielectric constants for the dielectric and metal respectively, and k_0 is the free space wave vector. The requirement for surface waves propagating along the surface is that k_x^2 should be real, i.e, $\varepsilon_d + \varepsilon_m < 0$ and $|\varepsilon_m| > \varepsilon_d$. Such

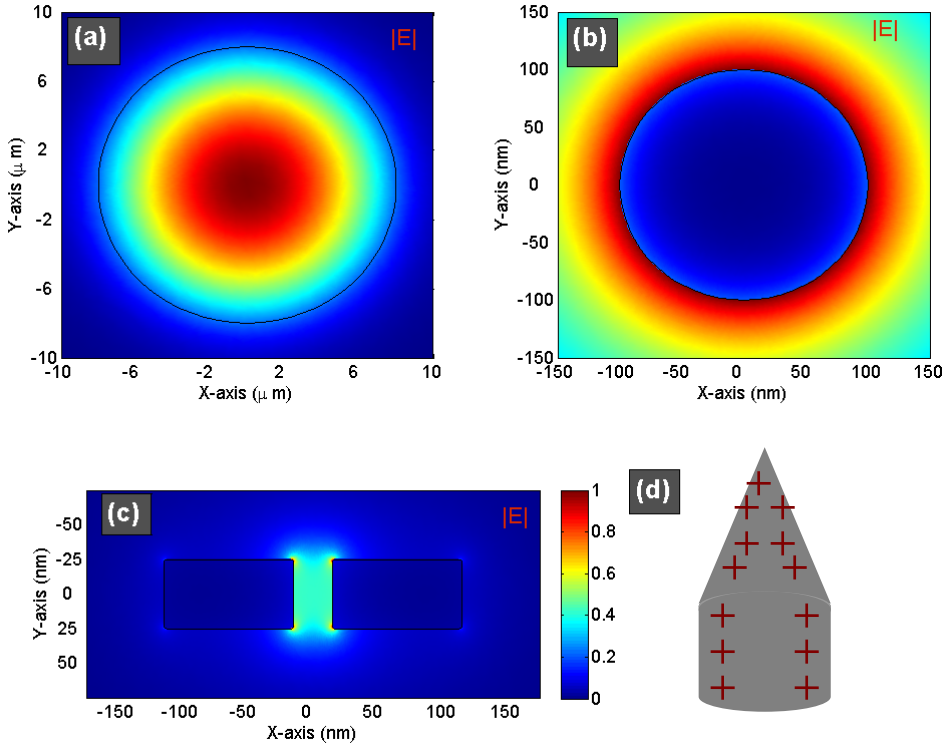

Figure 2.4: Magnitude of electric field $|E| = \sqrt{E_x^2 + E_y^2 + E_z^2}$ *in the transverse plane of (a) the standard single mode optical fiber, (b) 100 nm radius metallic nanowire and (c) the metallic slot waveguide. (d) Sketch of tapered metallic nanowire.*

condition can be fulfilled for metals or highly doped semiconductor in the visible and infrared region.

Under the aforementioned condition, the SPP wavevector is larger than the light line $k_0\sqrt{\varepsilon_d}$, as shown in Fig. 2.3 (a). Hence, the wave vectors along the z direction both in metals and dielectric are purely imaginary, which indicates that the field amplitude of the SPPs decreases exponentially, cf. Fig. 2.3 (b). Such exponential decaying behavior of the field reveal the relevance of the interface and the "trapped", non-radiative nature of SPPs. One distinctive feature is the tight confinement along the z direction, which provides the possibilities of manipulating, i.e., guiding light below the diffraction limit. Due to the large momentum associated with SPPs,

light cannot be coupled to SPP waves directly. To compensate the momentum mismatch between the optical plasmons and photons, several techniques, such as prism coupling, grating coupling and defects scattering coupling have been proposed and experimentally realized [64, 66].

2.4.4 Evanescent waves, field concentration and field enhancement

Evanescent waves can be induced by the inhomogeneities of the photonic environment. The simplest case of an inhomogeneity is a plane interface, i.e, the air-glass interface. The presence of such air-glass interface will give rise to reflection and refraction due to the boundary condition constraints, the ratio and phase shift of which with respect to the incident light are described by Snell's law. When a plane wave of light is incident from the denser medium (i.e., glass) and has an angle of incidence beyond a critical angle, the light can be totally reflected. Meanwhile, an evanescent wave is created from such plane wave incidence, which is usually referred to as total internal reflection. Since the evanescent waves do not transport energy along the direction perpendicular to the interface, there will be no power flux detected for the refracted part of the light, especially when the observation point is far away from the interface, saying larger than several hundred optical cycles. However, the evanescent waves in the total internal reflection phenomena transport energy along the surface, similar to the SPPs supported by a metallic-dielectric interface.

In the photonic environments, the corresponding eigenmodes can be decomposed into the plane waves characterized by the wave vector $\boldsymbol{k}$. In a cartesian coordinate system, the three components of the wave vector $\boldsymbol{k} = [k_x \quad k_y \quad k_z]$ satisfy the following relation,

$$\varepsilon(\boldsymbol{r})k_0^2 = k_x^2 + k_y^2 + k_z^2, \tag{2.36}$$

where $\varepsilon(\boldsymbol{r})$ is the spatially dependent dielectric constant with spatial dependence. Depending on various optical systems, k_x, k_y and k_z can be real or imaginary, as long as the condition defined by Eq. (2.36) is fulfilled. For an imaginary value of k_i, $i \in (x, y, z)$, the field along the i-axis has an evanescent feature and decays exponentially. Usually, the field for evanescent waves decays exponentially along the direction which is perpendicular to the interface between two different media. In optical imaging systems, evanescent waves induced by a conventional lens can not reach the image plane and functions as an obstacle, which fundamentally limits the minimum size of the image spot. The essence of near-field optical microscopy

is to convert such evanescent waves into the measurable form of far-field radiation before it becomes really evanescent. On the other side, from waveguiding point of view, the evanescent waves in the transverse plane induced by the inhomogeneity in the index contrast waveguides, i.e., optical fibers and plasmonic waveguides, are essential for guiding light and avoiding the leakage in the transverse plane.

The field concentration by the metallic-dielectric interface is qualitatively measured by the penetration length $\mathtt{Z}_j$ of the evanescent wave in medium j, $j \in (m, d)$, which can be obtained from Eq. (2.35) and Eq. (2.36),

$$\mathtt{Z}_j = \frac{1}{k_0} \frac{\varepsilon_j}{\sqrt{\varepsilon_d + \varepsilon_m}}. \tag{2.37}$$

For example, for a silver-air interface at a wavelength of 1 μm with $\varepsilon_m = -48$, $\varepsilon_d = 1$, the penetration lengths are on the order of 650 nm in air and 14 nm in silver. The confinement of the field can be substantially improved by introducing another dimensional confinement, i.e., one additional imaginary component of $\boldsymbol{k}$ by changing the waveguide geometry, like metallic nanowire and metallic slot waveguide, as shown in Fig. 2.4. For such 3 dimensional waveguides with translation invariance along propagation direction, the effective mode area in the transverse plane ($\mathtt{X} - \mathtt{Y}$ plane) is usually defined as the region, on the border of which the field amplitude is $1/e$ of the maximum. For a 100 nm radii metallic nanowire, one can estimate the effective area is around $300 \times 300\,\mathtt{nm}^2$, shown in Fig. 2.4 (b). For the standard single mode optical fiber, the effective mode area approximately equals to $16 \times 16\ (\mu m)^2$, cf. Fig. 2.4 (a). With the same power flux, the field on average is enhanced by a factor of 50. The effective mode area can further be squeezed in the metallic slot waveguide, shown in Fig. 2.4 (c), and approximately equals to $50 \times 50\,\mathtt{nm}^2$, which indicates an enhancement of the averaged field by a factor of 160. It was reported that using a tapered metallic nanowire, the propagating SPP can be adiabatically transformed into localized surface plasmons without major losses [67], as sketched in Fig. 2.4 (d). Apart from the tight confinement of optical field in the transverse plane, the geometric slowing effect gives rise to the accumulation of the SPP energy at the very end of the tip and the corresponding enhancement of local field by more than 3 order of magnitude. Such significant increase of local field is valuable for nonlinear optics, and can also potentially merit the efficiency of many optical devices.

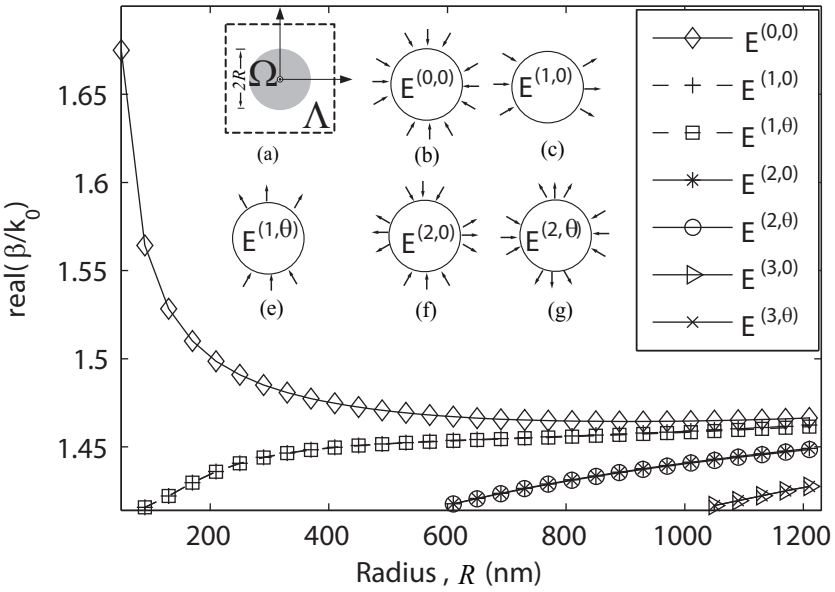

Figure 2.5: Dispersion relation versus radius for the cylindrical gold nanowire with the background medium of PMMA (n=1.414) at the wavelength of 1 μm. Inset (a) shows the waveguide structure. Inset (b-g) show electric field orientation of the possible eigenmodes supported by the waveguide.

2.4.5 Dispersion relation of metallic wires and square plasmonic waveguides

One of the major purposes of the thesis is to study the coupling between an quantum emitter and the freely propagating SPPs, hence it is essential to study the dispersion relations of the propagating plasmonic modes for an efficient coupling. The starting point of the numerical analysis of the plasmonic waveguide is the wave equation for the electric field with j=0 in Eq. (2.9),

$$\nabla \times (\nabla \times \boldsymbol{E}) - k_0^2 \varepsilon_r \boldsymbol{E} = 0, \tag{2.38}$$

where $k_0 = \omega\sqrt{\varepsilon_0 \mu_0}$ is the vacuum wave number, ε_r denotes the dielectric function relative to vacuum and μ_r represents the relative permeability constant, which is assumed to be 1 throughout the thesis. Due to the invariance along the z-axis, the Z-dependence of the solution to the wave equation must be that of a plane wave

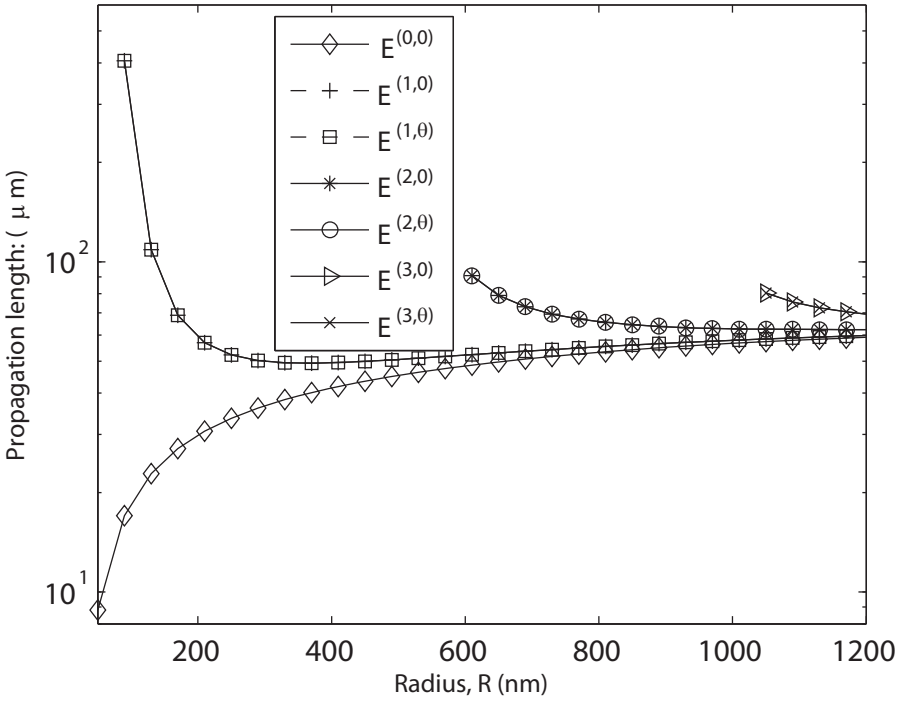

Figure 2.6: Propagation length versus radius for the cylindrical gold nanowire at the wavelength of 1 μm.

(complex exponential),

$$\boldsymbol{E}(x,y,z) = \boldsymbol{E}_\alpha(x,y)e^{-j(\omega t-\beta z)}. \tag{2.39}$$

For the guided plasmonic modes, at a specific frequency ω, two quantization indices are needed to specify a complete set of orthogonal modes, i.e., $\alpha = \{p, \beta\}$. β denotes the propagation constant (the component of the wave vector along the z-axis), and the index p represents the polarization of the mode. The waveguide structure examined consists of two regions Ω and Λ. Ω is the lossy metal core, which is surrounded by an infinite lossless dielectric medium Λ. The transverse component of the wave vector, defined as $k_{i\perp} = j\kappa_{i\perp}$, fulfills $j\kappa_{i\perp} = \sqrt{\frac{\omega^2}{c^2}\varepsilon_i - \beta^2}$ with $i \in [\Omega, \Lambda]$, where ε_i is the relative permittivity. FEM is utilized as a numerical tool to calculate the guided plasmonic modes. The infinite dielectric medium is trun-

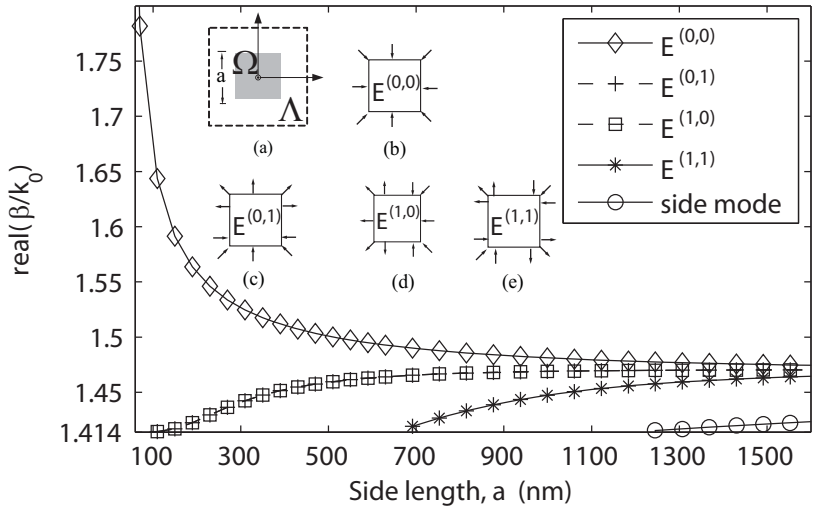

Figure 2.7: Dispersion relation versus side length of square plasmonic waveguides with background medium of PMMA (n=1.414) at a wavelength of 1 μm. The metal core is gold. Inset (a) shows the waveguide structure. Inset (b-e) show electric field orientation of the possible eigenmodes supported by square plasmonic waveguides.

cated to perform the finite element analysis of the waveguide structure by placing the structure inside a computational window, which is large enough to guarantee the field vanishing at the boundary. Here, we consider an optical wavelength of 1 μm and the relative optical permittivities of the waveguide are $\varepsilon_\Omega = -50 + 3.85j$ and $\varepsilon_\Lambda = 2$, corresponding to gold [68] and an ordinary polymer, i.e., polymethylmethacrylate (PMMA). The dispersion and the field orientation of the possible modes for cylindrical [47] and square waveguides [69] are presented in Fig. 2.5 and Fig. 2.7 respectively. As shown in the inset of Fig. 2.5, these modes can be represented by two indices, where the first index corresponds to the mode with angular moment of m, and the second index describes the polarization degenerate mode with the same m. For example, if $E^{m,0}$ denotes a mode related with angular moment of m, then $E^{m,\theta}$ denotes the corresponding degenerated mode, the field distribution of which is rotated by θ along the Z axis compared with $E^{m,0}$, where $\theta = \pi/2m$. As pointed out by Takahara et al. [6], the fundamental mode $E^{(0,0)}$ does not have a cutoff size of the radius, which is confirmed by the dispersion relation in Fig. 2.5. The modes supported by the metallic nanowire preserve the cylindrical symmetry

of the waveguide. Due to the constraints from the boundary condition, only TM modes exist.

The propagation length $L = [\mathtt{Im}(\beta)]^{-1}$ with the radius of the gold wire is shown in Fig. 2.6. The two modes $E^{(1,0)}$ and $E^{(1,\theta)}$ are long range propagating modes, with propagating lengths around few hundred μm. The fundamental mode $E^{(0,0)}$ has the shortest propagation length, compared with other higher modes. The shorter propagation length indicates larger losses of $E^{(0,0)}$ mode, which is due to the stronger confinement and larger fraction of SPP energy penetrating into the lossy metals. For a specific SPP based application, one has to take into account the tradeoff the between the confinement and propagation to achieve the best the performance.

For the square surface plasmon polariton waveguides, the fundamental modes, which were studied by Jung et al.[69], can be labeled in terms of two indices, which denote the number of sign changes in the dominant component of the electric field along the x and y axes, respectively. Both plasmonic waveguides support one fundamental mode ($E^{0,0}$) without any cutoff size of the metal core, and the corresponding propagation constants increase when the size of the metal core is further shrunk, which slows down the propagating plasmonic mode. Such geometric slowing down enhances the LDOS and the coupling efficiency to a nearby quantum emitter. We note that plasmonic modes supported by the metallic strips attracted considerable interest recently, due to the tight confinement of the field as well as the long range propagation [70, 71, 72, 73]. In the following calculations, the size of the metal core is restricted to be below the cutoff size of higher order modes so that only a single mode is supported. We note that apart from the highly localized mode, a weakly localized mode also exists. However, since the contribution to the total decay rate from such a weakly guided mode is small, we simply treat this mode as one of the radiation modes in our model.

2.4.6 Infinite long plasmon chains

Apart from the propagating SPPs, localized surface plasmons can also be excited in many cases. Such localized modes can be excited from the scattering problem of a small, sub-wavelength conductive particles in the presence of an oscillating electromagnetic waves. For frequencies close to the localized plasmon resonance of a single particle, the periodic nano-particle chains can also give rise to coherent transport of electromagnetic excitation below the diffraction limit. The nano-particle chain is sketched in Fig. 2.8 (a). Such effect is well modeled by dipole-dipole coupling between resonant particles on the chain for frequencies near the dipolar resonance,

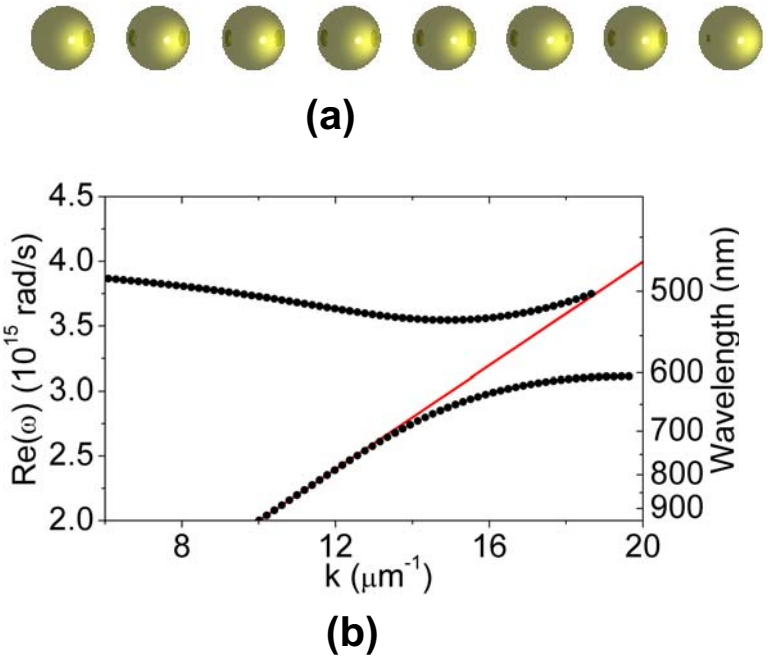

Figure 2.8: Black curves: real part of dispersion relation for the transverse modes of the infinite long plasmon particle array waveguide (pitch between two particle equals 160 nm, radius 50 nm)in glass with index of 1.5*. The red line denotes the "light line" in glass.*

as long as the sphere separation d is more than about three times the radius [74, 75]. Due to the dipolar interactions with the near-field term which is proportional to d^{-3}, the nanoparticle chain supports longitudinal and transverse propagating polarization waves. The dispersion relation for the transverse modes supported by the infinite long plasmon chain is relevant for the reconfigurable plasmon based single photon sources which is explored in chapter 5. Hence we will briefly discuss the dispersion relation for the transverse plasmonic mode on an infinite array of plasmon particles, calculated from a point dipole approximation. The method of the point dipole approximation and its validation will be explained in Chapter 3.

It is shown that the radiation damping, retardation effects can dramatically affect the loss and dispersion of the plasmon particle chain [75, 76]. It is also reported that retardation causes the dispersion to split into two anticrossing branches for

transverse modes [77]. As shown in Fig. 2.8 (b), the real part of the corresponding infinite chain dispersion relation for the traverse mode calculated from point dipole model, which includes the radiation damping as well as the retardation effects, is split into two branches by the "light line". The anticrossing of the two branches with the "light line" in glass is due to the coupling between the plasmons and the free photons. The upper branch corresponds to highly leaky modes due to the huge radiation losses, while the lower branch is essentially dark plasmons subjected only to ohmic damping [77]. Such polariton behavior is generic for the resonant nano-particle arrays.

Chapter 3

Modeling techniques

3.1 Overview of numerical techniques

Substantial efforts have been made to solve a more general form of the wave equation defined by Eq. (2.9), namely with arbitrary time dependence, which is also a central task in modeling nano-photonic devices. However, only for a few geometries such as spheres and cylinders, one is able to obtain analytical solutions, by the assistance of, e.g., Mie's theory [78] and other modal descriptions [79]. For many other geometries, one has to resort to numerical methods, like finite-difference time-domain (FDTD) method, FEM, or other methods. These numerical methods are indispensable in modern photonics, especially in modeling complex photonic devices. The advance in the electronic computers enable us to design, analyze and optimize photonic devices in a much cheaper way, with respect to that of constructing a prototype physically and measuring it in reality. More importantly, numerical simulations provide enormous amount of physical insight.

Among various types of numerical simulation tools, many are based on the method of moments (MOM) [80], the FDTD method [81], and the FEM method [82, 83]. Other methods, such as the point dipole method and finite integrate techniques, can be identified as either a variation or an equivalent of one of the first three [48]. The MOM has its origin in electromagnetic practice with special emphasis on antenna theory. The method casts the solution for the induced current in the form of an surface or volume integral equation where the unknown induced current density is part of the integrand. Once the induced current is known, the field at arbitrary position can be calculated with assistance of the Green's function.

Hence the MOM is very useful in solving radiation and scattering problem, typically when the electromagnetic sources are the quantities of interests [80]. However, the capability of MOM is challenged when the photonic environment is complex, i.e., anisotropic and inhomogeneous, where the Green's function is hard to obtain. Moreover, the MOM generates a fully populated matrix whose computation and solution are associated with a high degree of computational complexity. In spite of these drawbacks, the MOM is a powerful tool and a preferential choice for analyzing antennas.

The FDTD method, invented in the mid-1960s, is a popular computational electromagnetic modeling technique [81]. In FDTD, the space and time partial derivatives in Maxwell's equations are approximated by finite differences. The resulting finite-difference equations are solved in a leaping frog manner. The method can easily handle material anisotropy and inhomogeneity and has become very powerful and increasingly popular due to its simplicity in formulation, implementation, and grid generation. It is also a highly efficient method due to the fact that it yields a broadband solution with one time-domain simulation through Fourier transformation.

Though FDTD can model dielectric structures reasonably well, i.e., photonic crystals, it has severe drawbacks for modeling plasmonic structures [84]. Firstly, the rectangular grids typically used in FDTD are not suitable for complex plasmonic structures due to the high localization of the field at the metal-dielectric interfaces, which requires much finer grid resolution than modeling of dielectric structures. The piecewise constant approximation of the fields within grids in FDTD poses difficulties in applying boundary condition at the metal-dielectric interfaces, which is crucial for modeling the plasmonic structures. Secondly, in FDTD and other time domain methods the dielectric functions of the material need to be approximated by proper analytical expressions which give rise to considerable error in broadband calculations. Apart from these general drawbacks, the LDOS calculations present additional challenges for FDTD, due to difficulties in accurately transforming $j \cdot E$ from the time to frequency domain, as explained in Koenderink et al [85, 86, 87].

However, FEM does not have such challenges due to the more advanced discretization strategy for complex geometric structures by using a variety of elements of different shapes, and FEM is a frequency method which can handle arbitrary material dispersion. One might consider other options, i.e., the Green dyadic function method [49] or point dipole method [88], however, the Green dyadic function method encounters difficulties in constructing Green's functions for complex geome-

tries, and the point dipole model is limited to homogenous dielectric environments in which the metals are embedded. Since we want to develop a generally applicable quantitative method of modeling spontaneous emission for complex plasmonic structures, FEM is chosen as the numerical tool to attack the problem. Therefore in the chapter we will concentrate on the implementation of finite element modeling to calculate the decay rates of quantum emitters coupled to plasmonic waveguides. In the end of this chapter, the point dipole approximation and a multipole expansion multiple scattering approach called MESME are briefly discussed. The point dipole approximation is employed to calculate the dispersion of the infinite long plasmon particle embedded in homogenous medium in Chapter 2, and MESME is used to calculate the far field emission pattern and the quantum efficiency of a finite long plasmon chain in Chapter 5.

3.2 FEM modeling of spontaneous emission enhanced by a plasmonic waveguide

We focus on the modeling of the spontaneous emission of a quantum emitter at nanoscale proximity to realistic plasmonic waveguides by using a FEM approach, with special emphasis on calculating the spontaneous emission β factor. The β factor describes the fraction of the emitted energy that is coupled to the plasmonic mode. Subwavelength waveguiding of plasmons in metallic structures has been studied theoretically [6, 89] and has also been observed in a number of recent experiments [7]. Enhanced spontaneous emission of an emitter coupled to plasmonic waveguides has been proposed [9, 10] and experimentally demonstrated [8] recently. Chang et al. [47] studied the spontaneous emission of an emitter coupled to a metallic nanowire by exploiting, except for a single example, the quasistatic approximation. In the quasistatic approximation, it is assumed that the magnetic field vanishes. Hence the wave equation defined by Eq. (2.9) can be reduced to a poisson equation by using the scale potential. Their model qualitatively shows that, *for small nanowire radii,* it is possible to obtain efficient coupling without taking into account the wave properties of the plasmonic mode. Jun et al. [10] employed an FDTD numerical method to study the different spontaneous emission decay rates of an emitter coupled to a metallic slot waveguide, but using simplifying assumptions for the LDOS calculations of the plasmonic mode. A self-consistent model with a rigorous treatment of all the spontaneous decay rates involved, i.e. radiative as well

as non-radiative is desirable for modeling realistic nano-photonic devices. The aim of this section is to provide such a detailed modeling and to extend earlier results to realistic structures. Before we go to the details of modeling plasmonic waveguides coupled to a quantum emitter, we will study a simple FEM example to illustrate the basic procedures to solve a differential equation by using FEM.

3.2.1 A simple FEM example based on variational formulation

The finite element method is a numerical technique for finding approximate solutions to boundary-value problems of mathematical physics with assistance of an electronic computer. Given a boundary-value problem defined by the differential equation

$$\mathcal{L}\phi = f, \tag{3.1}$$

if the differential operator $\mathcal{L}$ is self-adjoint,

$$\langle \mathcal{L}\phi, \psi \rangle = \langle \mathcal{L}\psi, \phi \rangle, \tag{3.2}$$

and positive definite,

$$\langle \mathcal{L}\phi, \phi \rangle = \begin{cases} > 0 & \phi \neq 0, \\ = 0 & \phi = 0, \end{cases} \tag{3.3}$$

then its solution can be obtained by minimizing the functional given by [82],

$$F(\phi) = \frac{1}{2}\langle \mathcal{L}\phi, \phi \rangle - \frac{1}{2}\langle \phi, f \rangle - \frac{1}{2}\langle f\phi \rangle, \tag{3.4}$$

where f denotes an arbitrary function satisfying the same boundary functions as ϕ does. The angular brackets denote the inner product defined by

$$\langle \phi, \psi \rangle = \int_{\Omega} \phi\psi^* d\Omega, \tag{3.5}$$

where Ω and asterisk denote the modeling domain and complex conjugate operation, respectively. Equation (3.4) is one of the two methods usually employed to formulate the finite element solutions, the so-called variational form. Because of its several advantages, such as the well-established mathematical foundations, convenience of description, and elegance of formulation, the variational form was usually preferred over Galerkin's method to construct the finite element solution in the past, which is also the reason that the variational form is adopted in the thesis.

To outline the basic procedures, let us consider a simple problem defined by a second-order differential equation

$$\tfrac{d^2\phi}{dx^2} = x + 1, \quad 0 < x < 1, \tag{3.6}$$

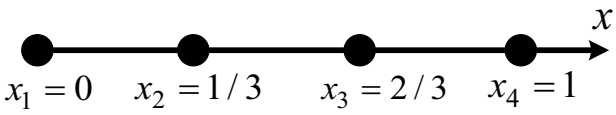

Figure 3.1: Discretization of the modeling domain $x \in [0, 1]$.

in conjunction with the boundary condition given by

$$\begin{aligned} \phi_{x=0} &= 0, \\ \phi_{x=1} &= 1. \end{aligned} \tag{3.7}$$

The exact solution to the problem is

$$\phi(x) = \frac{1}{6}x^3 + \frac{1}{2}x^2 + \frac{1}{3}x. \tag{3.8}$$

Here we approximate the finite element solution to Eq. (3.6) to outline the basic procedures of implementing FEM modeling based on the variational formulation.

Firstly, the functional corresponding to Eq. (3.6) can be constructed as follows,

$$F(\tilde{\phi}) = \frac{1}{2}\int_0^1 (\frac{d\tilde{\phi}}{dx})^2 dx + \int_0^1 (x+1)\tilde{\phi} dx, \tag{3.9}$$

The solution to Eq. (3.6) can be obtained by minimizing the functional Eq. (3.9) with respect to $\tilde{\phi}$, where $\tilde{\phi}$ is the trial function. Secondly, the solution domain $(0, 1)$ is divided into three subdomains, as sketched in Fig. 3.1.

The subdomains defined by (x_1, x_2), (x_2, x_3), (x_3, x_4) are equally spaced, which is not essential. For instance, the values of $x_2 = \frac{1}{4}$, $x_3 = \frac{3}{5}$ can also be used. Subsequently, we could assume a linear variation of $\tilde{\phi}$ over each subdomain defined by

$$\tilde{\phi} = \phi_i \frac{x_{i+1} - x}{x_{i+1} - x_i} + \phi_{i+1} \frac{x - x_i}{x_{i+1} - x_i}, \tag{3.10}$$

for $x_i \leq x \leq x_{i+1}$ and $i = 1, 2, 3$, where ϕ_i are the unknown coefficients to be determined. The approximation of the unknown solution with each segment (element) is called selection of interpolation function. Normally the interpolation is chosen to be a polynomial of first, second and higher order. Higher order polynomials give more accurate results, and also require more a complicated formulation. The simple linear interpolation hence is used here, and still widely used in practice.

We can obtain the finite element formulation by substituting Eq. (3.10) into

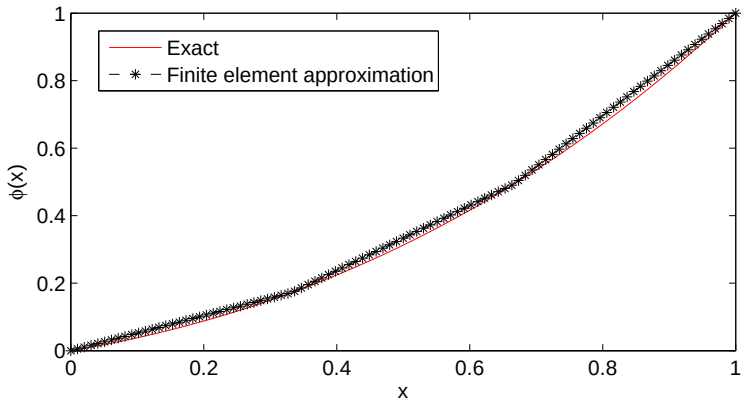

Figure 3.2: Numerical results compared with the exact values.

Eq. (3.9) as follows,

$$F = \sum_{i=1}^{3} [\frac{1}{2} \int_{x_i}^{x_{i+1}} (\frac{\phi_{i+1} - \phi_i}{x_{i+1} - x_i})^2 dx + \int_{x_i}^{x_{i+1}} (x+1)(\phi_i \frac{x_{i+1} - x}{x_{i+1} - x_i} + \phi_{i+1} \frac{x - x_i}{x_{i+1} - x_i}) dx]. \tag{3.11}$$

A close examination will reveal that ϕ_i denotes the value of $\phi(x)$ at x_i. From the boundary condition we find $\phi_1 = 0$, $\phi_4 = 1$. Evaluating the integrals yields

$$F = 3(\phi_2^3 + \phi_3^3) - 3\phi_2\phi_3 + \frac{4}{9}\phi_2 - \frac{22}{9}\phi_3 + \frac{49}{27}. \tag{3.12}$$

By minimizing F we can calculate $\phi_2 = \frac{14}{81}$, $\phi_3 = \frac{40}{81}$. Once we obtain the solution at x_i, the solution at the other points is obtained from the linear interpolation based in Eq. (3.10). The finite element solution is plotted in Fig. 3.2 with comparison with the exact solution. As can be seen, the exact values were obtained at x_i, there is a small discrepancy at other points between the exact solution and the finite element approximated values. The discrepancy can be decreased by using more segments or employing higher order polynomials.

The simple example above reveals the essential ingredients of the finite element modeling, including discretization of the modeling domain, construction of the interpolation function, formulation of the system of equations combined with the boundary conditions, and solving the system of equations. Conventionally, the trial function in the classic variational method is formulated as a combination of a set of basis functions defined over the entire domain, while in FEM, the trial function

is a combination of a set of basis functions defined over subdomains that comprise the entire domain.

3.2.2 Modeling of plasmonic decay rate: 2D

Initially we calculate the electric field for a plasmonic waveguide numerically using FEM, subsequently we construct the dyadic Green's function based on the numerical data. Then the imaginary part of electric-field dyadic Green's function for a specific guided plasmonic mode can be used to extract the spontaneous emission decay rate of the emitter into that mode. In the following part we will explain how to construct the electric-field dyadic Green's function as defined in Eq. (2.10) for one guided plasmonic mode [90, 11].

Rigorously speaking, the operator defined by $L = \left[\nabla \times \nabla \times -k_0^2 \varepsilon(\boldsymbol{r})\right]$ does not have a set of complete and orthogonal eigenmodes due to its non Hermitian character if $\varepsilon(\boldsymbol{r})$ is complex. Without loss of generality, we adopt biorthogonality to form a complete set of "orthogonal" modes of the waveguides initially, and then we will end up with an approximation from the power orthogonality for the plasmonic waveguides. Suppose that $\boldsymbol{E}_n$ is a set of eigensolutions defined by $\hat{L}$, the biorthogonal modes $\boldsymbol{E}_m^\dagger$ are defined as the eigensolutions of the adjoint operator denoted by $\hat{L}^\dagger$, which is obtained from the operator $\hat{L}$ by replacing $\varepsilon(\boldsymbol{r})$ with its complex conjugate. The biorthogonality condition is then given by

$$\int \varepsilon(\boldsymbol{r}) \boldsymbol{E}_n(\boldsymbol{r}) \cdot [\boldsymbol{E}_m^\dagger(\boldsymbol{r})]^* d^3 r = \delta_{nm} N_n, \tag{3.13}$$

with the completeness relation $\sum_n \frac{\varepsilon(\boldsymbol{r}) \boldsymbol{E}_n(\boldsymbol{r}) [\boldsymbol{E}_n^\dagger(\boldsymbol{r}')]^*}{N_n} = \boldsymbol{I}\delta(\boldsymbol{r} - \boldsymbol{r}')$. From the biorthogonal completeness relation, the dyadic Green's function $\bar{\boldsymbol{G}}(\boldsymbol{r}, \boldsymbol{r}', \omega)$ can be constructed from the eigenfunction expansion as follows [90],

$$\begin{aligned} &\bar{\boldsymbol{G}}(\boldsymbol{r}, \boldsymbol{r}', \omega) = \bar{\boldsymbol{G}}_{GT}(\boldsymbol{r}, \boldsymbol{r}', \omega) + \bar{\boldsymbol{G}}_{GL}(\boldsymbol{r}, \boldsymbol{r}', \omega) \\ &= \sum_n \frac{\boldsymbol{E}_n(\boldsymbol{r}) [\boldsymbol{E}_n^\dagger(\boldsymbol{r}')]^*}{N_n \lambda_n} + \sum_n \frac{\nabla \phi_n(\boldsymbol{r}) [\nabla \phi_n^\dagger(\boldsymbol{r}')]^*}{M_n k_0^2}, \end{aligned} \tag{3.14}$$

where the generalized transverse part of the dyadic Green's function, $\bar{\boldsymbol{G}}_{GT}$, is constructed from the complete set of transverse eigenfunction $\boldsymbol{E}_n(\boldsymbol{r})$ given by,

$$\begin{aligned} &-\nabla \times \nabla \times \boldsymbol{E}_n(\boldsymbol{r}) + k_0^2 \varepsilon(\boldsymbol{r}) \boldsymbol{E}_n(\boldsymbol{r}) = \lambda_n \varepsilon(\boldsymbol{r}) \boldsymbol{E}_n(\boldsymbol{r}), \\ &\nabla \cdot [\varepsilon(\boldsymbol{r}) \boldsymbol{E}_n(\boldsymbol{r})] = 0. \end{aligned} \tag{3.15}$$

with the eigenvalue λ_n. The longitudinal or quasistatic part $\bar{\boldsymbol{G}}_{GL}$ is constructed from longitudinal eigenfunctions that can be found from a complete set of scalar

eigenmodes $\phi_n(\boldsymbol{r})$ satisfying

$$\nabla \cdot [\varepsilon(\boldsymbol{r}) \nabla \phi_n(\boldsymbol{r})] = \sigma_n \phi_n(\boldsymbol{r}), \tag{3.16}$$

with the biorthogonality relation, $\int \varepsilon(\boldsymbol{r}) \nabla \phi_n(\boldsymbol{r}) \cdot [\nabla \phi_n^\dagger(\boldsymbol{r})]^* d^3r = \delta_{nm} M_n$. Since we are studying the guided plasmonic mode, which describes the field solution in the absence of electric charges ($\nabla \cdot [\varepsilon(\boldsymbol{r}) \boldsymbol{E}_n(\boldsymbol{r})] = 0$), the longitudinal component will vanish in the following calculations.

By applying the principle of constructing the electric-field dyadic Green's function to the case of a plasmonic waveguide, we find the contribution to the dyadic Green's function from the plasmonic modes as

$$\bar{\boldsymbol{G}}_{pl}(\boldsymbol{r}, \boldsymbol{r}') = \sum_p \int_{-\infty}^{+\infty} \frac{\varepsilon_\Lambda \boldsymbol{E}_\alpha(\boldsymbol{r}) [\boldsymbol{E}_\alpha^\dagger(\boldsymbol{r}')]^* e^{j\beta(z-z')}}{[k_0^2 \varepsilon_\Lambda - (\beta^2 - \kappa_{\Lambda\perp}^2)] N_\alpha} d\beta, \tag{3.17}$$

where the normalization factor is given by

$$\begin{aligned} \delta(\beta - \beta') \delta_{pp'} N_\alpha &= \int \varepsilon(\boldsymbol{r}) \boldsymbol{E}_\alpha(\boldsymbol{r}) \cdot [\boldsymbol{E}_{\alpha'}^\dagger(\boldsymbol{r})]^* d^3r \\ &= 2\pi \delta(\beta - \beta') \delta_{pp'} \int \varepsilon(x,y) \boldsymbol{E}_\alpha(x,y) \cdot [\boldsymbol{E}_\alpha^\dagger(x,y)]^* dxdy, \end{aligned} \tag{3.18}$$

which can be further simplified as $N_\alpha = 2\pi \int \varepsilon(x,y) \boldsymbol{E}_\alpha(x,y) \cdot [\boldsymbol{E}_\alpha^\dagger(x,y)]^* dxdy$, if one realizes that α and α' are required to denote the same mode in Eq. (4.5). For one plasmonic mode, the Eq. (4.5) is evaluated in closed form by the method of contour integration as the integrand decays to zero at infinity in the upper and the lower β plane,

$$\begin{aligned} \bar{\boldsymbol{G}}_{pl}(\boldsymbol{r}, \boldsymbol{r}) &= j2\pi \frac{\varepsilon_\Lambda \boldsymbol{E}_{\alpha_0}(x,y) [\boldsymbol{E}_{\alpha_0}^\dagger(x,y)]^*}{\frac{d(k_0^2 \varepsilon_2)}{d\beta} N} \\ &= \frac{j\pi c^2 \boldsymbol{E}_{\alpha_0}(x,y) [\boldsymbol{E}_{\alpha_0}^\dagger(x,y)]^*}{\omega N v_g}, \end{aligned} \tag{3.19}$$

where v_g is the group velocity, defined by $v_g = d\omega/d\beta$. The corresponding projected LDOS for one plasmonic mode can be calculated from the dyadic Green's function according to Novotny [48], cf. Eq. (2.18). If the dipole emitter is oriented along the X axis, the projected LDOS for the plasmonic mode is given by $\rho_{pl}(\boldsymbol{r}, \omega) = 6|E_{\alpha,x}(\boldsymbol{r})|^2/(N v_g)$. The spontaneous emission decay rate into the plasmonic mode can be calculated by $\gamma_{pl} = \frac{\pi \omega_0}{3\hbar\varepsilon_0} |\mu|^2 \rho_{pl}(\boldsymbol{r}, \omega)$. Normalized by the spontaneous emission decay rate in the vacuum, the emission enhancement due to the

plasmonic excitation is

$$\frac{\gamma_{pl}}{\gamma_0} = \frac{6\pi^2 c^3 E_{\alpha_0,X}(x,y)[E^{\dagger}_{\alpha_0,X}(x,y)]^*}{\omega_0^2 N \upsilon_g}. \tag{3.20}$$

Eq. (3.20) gives a general expression for the spontaneous emission decay rate into a guided mode, supported by a lossy or lossless waveguide. In dielectric waveguides, losses are generally small, and the biorthogonal modes $\boldsymbol{E}_m^{\dagger}$ can to a good approximation be replaced by the orthogonal mode $\boldsymbol{E}_m$. Such an approximation is also valid for our plasmonic waveguide, where the imaginary part of the propagation constant for the fundamental mode is around 1% of the real part. According to Snyder[91], the group velocity can be calculated by $\upsilon_g = \frac{\int_{A_\infty}(\boldsymbol{E}\times\boldsymbol{H}^*)\cdot\boldsymbol{z}dA}{\int_{A_\infty}\varepsilon_0\varepsilon(x,y)|\boldsymbol{E}(x,y)|^2 dA}$, where A_∞ denotes integration over the transverse plane. By applying the power orthogonality approximation and plugging the explicit form of the group velocity into Eq. (3.20), we obtain the following expression for the plasmonic decay rate of the fundamental mode,

$$\frac{\gamma_{pl}}{\gamma_0} = \frac{3\pi c\varepsilon_0 E_{\alpha_0,X}(x,y)E^*_{\alpha_0,X}(x,y)}{k_0^2\int_{A_\infty}(\boldsymbol{E}\times\boldsymbol{H}^*)\cdot\boldsymbol{z}dA}. \tag{3.21}$$

3.2.3 Modeling of total decay rate: 3D

As described in the previous subsection, the well defined field components in the transverse plane of the waveguide give the possibility of constructing the plasmonic part of the dyadic Green's function numerically. The reason is that the field is concentrated around the metallic core and decays to zero on the borders when the modeling domain is reasonably large. Hence, the perfect electric conductor boundary condition is implemented to truncate the 2D modeling domain. However, for the radiation modes, the field components in the transverse plane of the waveguide do not vanish no matter how large the modeling domain is. Hence, it is extremely difficult to construct the dyadic Green's function numerically for the radiation modes in a similar way as for the guided mode. Therefore, we implement a 3D model to include the radiation modes, as well as the nonradiative contributions, by solving the wave equation with a harmonic (time dependent) source term,

$$[\nabla\times\frac{1}{\mu_r}\nabla\times - k_0^2\varepsilon(\boldsymbol{r})]\boldsymbol{E}(\boldsymbol{r},\omega) - j\omega\mu_0\boldsymbol{J}(\omega) = 0. \tag{3.22}$$

In this section, we introduce the FEM method to calculate the LDOS in a 2D model and solve an equivalent problem in a 3D model. We found that the

LDOS can be efficiently extracted from the FEM numerical calculations, without the numerical difficulties encountered in FDTD, when the boundary condition of the modeling domain is properly handled. Concerning implementation of a FEM calculation, Eq. (3.22) needs to be reformulated. If we introduce a test function $\boldsymbol{F}(\bar{r},\omega)$, we can construct the functional corresponding to the wave equation in the following way[92],

$$\begin{aligned} L &= \int_V [\nabla \times \frac{1}{\mu_r} \nabla \times -k_0^2 \varepsilon(\boldsymbol{r})] \boldsymbol{E}(\boldsymbol{r},\omega) \cdot \boldsymbol{F}^*(\boldsymbol{r},\omega) dV - \int_V j\omega\mu_0 \boldsymbol{J}(\omega) \cdot \boldsymbol{F}^*(\boldsymbol{r},\omega) dV \\ &= \int_V \frac{1}{\mu_r} \nabla \times \boldsymbol{E}(\boldsymbol{r},\omega) \cdot \nabla \times \boldsymbol{F}^*(\boldsymbol{r},\omega) dV - \int_V k_0^2 \varepsilon(\boldsymbol{r}) \boldsymbol{E}(\boldsymbol{r},\omega) \cdot \boldsymbol{F}^*(\boldsymbol{r},\omega) dV \\ &\quad - \int_V j\omega\mu_0 \boldsymbol{J}(\omega) \cdot \boldsymbol{F}^*(\boldsymbol{r},\omega) dV + \oiint_{\partial V} \boldsymbol{F}^*(\boldsymbol{r},\omega) \cdot [\frac{1}{\mu_r} \boldsymbol{n} \times \nabla \times \boldsymbol{E}(\boldsymbol{r},\omega)] ds. \end{aligned} \tag{3.23}$$

where ∂V denotes the surface that encloses the volume V, and $\bar{n}$ denotes the outward unit normal vector to the surface of the modeling domain. This is the variational formulation of the wave equation, which is required to hold for all test functions. Eq. (3.23) enables us to formulate the finite element solution for such a boundary-value problem by employing the standard finite element solution procedures, including discretization and factorization of a sparse matrix [92]. The boundary-value problem defined by Eq. (3.23) was solved by utilizing a commercial software package, COMSOL Multiphysics [1].

It is crucial to truncate the computational domain properly. As shown in Fig. 3.3, we use two techniques for truncating the modeling domain: I) In the X-Y plane, the computation domain is truncated by the perfectly matched layers with thickness of half a wavelength in vacuum. II) Along the Z-axis, the computation domain is terminated by a mode matching boundary condition, which will induce a certain amount of reflection from the radiation modes and the higher order plasmonic modes if they exist. Essentially, the mode matching boundary is an absorbing wall, which behaves as a sink of electromagnetic waves. There are different options for realizing the mode matching boundary to absorb a single mode, depending on whether the absorbed mode is TE, TM or a hybrid mode. For a pure

[1] http://www.comsol.com

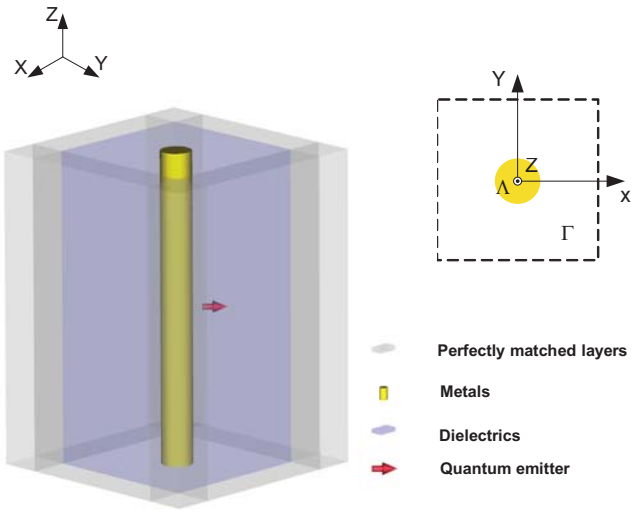

Figure 3.3: A single quantum emitter coupled to a metallic nanowire. The grey transparent region represents the perfectly matched layers, the mode matching boundary condition is applied on the top and the bottom of the structure. The quantum emitter is implemented by an electric line current.

TM or TE mode, it can be matched by simply applying the conditions,

$$\frac{1}{\mu_r}\boldsymbol{n}\times\nabla\times\boldsymbol{E}(\boldsymbol{r},\omega)=-\frac{k_0^2\varepsilon_r\boldsymbol{E}_t(\boldsymbol{r},\omega)}{j\beta}, \qquad TM; \tag{3.24a}$$

$$\frac{1}{\mu_r}\boldsymbol{n}\times\nabla\times\boldsymbol{E}(\boldsymbol{r},\omega)=-j\beta\boldsymbol{n}\times\frac{1}{\mu_r}\boldsymbol{n}\times\boldsymbol{E}_t(\boldsymbol{r},\omega), \qquad TE; \tag{3.24b}$$

on the boundary, where β is the propagation constant, and $\boldsymbol{E}_t(\boldsymbol{r},\omega)$ is the tangential components of the dependent variable $\boldsymbol{E}(\boldsymbol{r},\omega)$ on the boundaries in the numerical model. The mode matching boundary condition for the hybrid mode can be implemented as

$$\frac{1}{\mu_r}\boldsymbol{n}\times\nabla\times\boldsymbol{E}(\boldsymbol{r},\omega)=j\omega\mu_0\boldsymbol{n}\times\boldsymbol{H}_0, \tag{3.25}$$

where $\boldsymbol{E}(\boldsymbol{r},\omega)$ is the dependent variable solved in the 3D model, and $\boldsymbol{H}_0$ denotes the matched mode that is applied. In our model, $\boldsymbol{H}_0$ corresponds to the fundamental hybrid mode supported by the plasmonic waveguide. It is calculated from the 2D eigenvalue problem, and is given by

$$\boldsymbol{H}_0=\sqrt{\frac{\gamma_{pl}P_0}{P_{2d}}}\boldsymbol{H}_{2d}e^{j\beta L_0}=(H_{0x},H_{0y},H_{0z}). \tag{3.26}$$

Table 3.1: The relations between the 6 field components for the fundamental hybrid mode

Description	Relation
Tangential electric field, $s \in [x, y]$	$E^s_{2D,t} = -\frac{\beta}{\omega\varepsilon}(\boldsymbol{n} \times H_{2D,t})_s - \frac{j}{\omega\varepsilon}(\nabla_t \times \boldsymbol{n} H^n_{2D})_s$
Normal electric field	$E^n_{2D} = -\frac{j}{\omega\varepsilon}\boldsymbol{n} \cdot (\nabla_t \times H_{2D,t})$
Tangential magnetic field, $s \in [x, y]$	$H^s_{2D,t} = H^s_{2d,m}$
Normal magnetic field	$H^n_{2D} = jH^z_{2d,m}$

Here, P_{2d}, $\boldsymbol{H}_{2d}$ and β are the time averaged power flow, the magnetic field, and the propagation constant, respectively calculated from the 2D model, while P_0 denotes the normalization factor of the power emission in the 3D model, and L_0 represents the half length of the 3D model. Due to the losses of the metals, the magnitude of the magnetic field is a complex number. In order to guarantee that the phase of E_x at the position of the emitter is zero when the emitter is oriented horizontally, the extra phase $\phi = \arctan(\frac{imag(E^x_{2D})}{real(E^x_{2D})})$ needs to be compensated, i.e., $\boldsymbol{H}_0 = \sqrt{\frac{\gamma_{pl} P_0}{P_{2d}}}\boldsymbol{H}_{2d} e^{j(\beta L_0 + \phi)}$. In the 2D eigenvalue calculations, there are 6 components involved for the hybrid fundamental model, the relations of which are tabulated in Table 3.1. The magnitudes of the magnetic field, $\left(H^x_{2d,m}, H^y_{2d,m}, H^z_{2d,m}\right)$, are the dependent variables, which are calculated directly from the 2D numerical model.

The total decay rate, γ_{total}, is extracted from the total power dissipation of the current source coupled to the nearby metallic waveguide, $\gamma_{total}/\gamma_0 = P_{total}/P_0$, where $P_{total} = 1/2 \int_V Re(\boldsymbol{J}^* \cdot \boldsymbol{E}_{total}) dV$ is the power dissipation of the current source coupled to the metallic waveguide, and $P_0 = 1/2 \int_V Re(\boldsymbol{J}^* \cdot \boldsymbol{E}_0) dV$ is the emitted power by the same current source in vacuum. P_0 is a normalization factor, which is also used to normalize the power flow on the boundaries in Eq. (3.26). As demonstrated in Fig. 4.4, the field is generated by the current source, namely, the dipole emitter, which is implemented by a small electric line current. In our model, the dipole is oriented horizontally. For an electric current source with finite size of l ($l \ll \lambda_0$), and linear distribution of current I_0, the dipole moment of the source [65] is, $\mu = jI_0 l/\omega$. In order to avoid higher order multipole moments, the size of the current source should be restricted below a certain value. Our numerical tests

show that the variation of the total power dissipation from the size dependence of the emitter is negligible when the size of the emitter is smaller than 2 nm.

Basically, the accuracy of γ_{total}/γ_0 depends on the length of the plasmonic waveguide, which is studied in APPENDIX A (APPENDIX B) for the metallic nanowire (square plasmonic waveguide). Accordingly we estimate the relative error on the computed data of γ_{total}/γ_0 for the metallic nanowire (square plasmonic waveguide) to be $\pm 2.5\%$ ($\pm 2.0\%$) in the following calculations for L_0 larger than 1 μm.

3.2.4 Validation check of 3D FEM modeling

In order to check the validity of the mode matching boundary condition we studied the length dependence of the total decay rate for two different plasmonic waveguides. The length dependence of the total decay rate γ_{total} for the metallic nanowire is shown in Fig. 3.4. The fundamental mode supported by the metallic nanowire is TM, hence the mode matching boundary condition defined by Eq. (3.24a) is implemented. As can be seen from Fig. 3.4, the variation in the total decay rate is reduced by increasing L_0, and the damped oscillation of the total decay rate with L_0 indicates a certain amount of reflection from radiation modes, which is confirmed by the period of the oscillation (equal to the wavelength in a media with $\varepsilon = 2$). We also see that the variation of the total decay rate due to the length dependence is below $\pm 2.5\%$ due to the dominating excitation of the plasmonic mode for L_0 larger than 1.0 μm. The relative error on the computed data is even smaller, less than $\pm 1.0\%$ for L_0 larger than 1.75 μm.

Regarding the square plasmonic waveguide, the condition defined by Eq. (3.25) is applied on the boundary to absorb the hybrid mode supported by the waveguide, where $\boldsymbol{H}_0$ is the magnetic field for the matched field. As shown in Fig. 3.5, there is also a damped oscillation of the total decay rate with the length of the computation domain, and the tendency of achieving higher accuracy for γ_{total} when L_0 is lengthened, which is similar to the length dependence study of the total decay rate for the nanowire. Nevertheless, there are two distinctions between the two plots: I) The variation of the total decay rate for the square plasmonic waveguide is much larger than that for the metallic nanowire; II) The variation of the total decay rate for the square plasmonic waveguide with L_0 primarily stems from the reflection of two different modes, which are indicated by two different periods in the damped oscillation. The reflection of the fundamental mode, which is supposed to be absorbed at the boundaries, is responsible for the oscillation with the period of

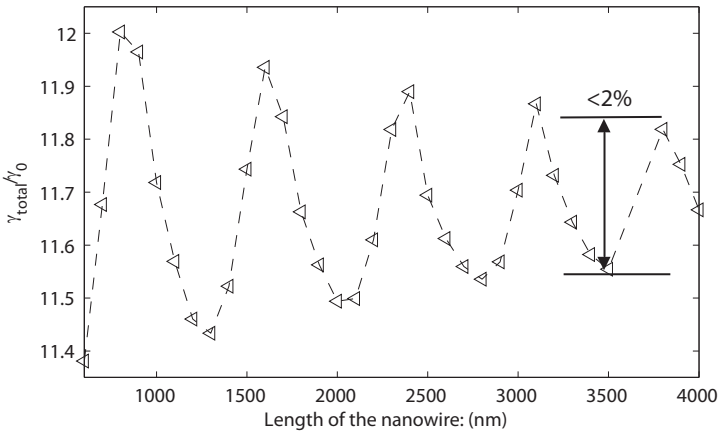

Figure 3.4: Length dependence study of the total decay rate for the metallic nanowire. The radius of the metallic nanowire is 20 nm, the distance of emitter to the wire edge is 30 nm.

400 nm, the other oscillation with the period of 740 nm results from the reflection of a quasi guided mode, denoted by E_{qg}. The explanation is the following: The boundary condition defined by Eq. (3.24a) can completely absorb the matched pure TM mode, while it is not true for the boundary condition defined by Eq. (3.25) for the hybrid mode, and a significant reflection from a quasi guided mode also exists for the square plasmonic waveguide. For the hybrid mode the last term in Eq. (3.23) relies not only on the tangential components of the electric (magnetic) field, but also on the normal component of the electric (magnetic) field, which is intrinsically lost on the boundary in the vector element formulation of the 3D numerical model [92]. Our interpretation is that even though the normal component of the electric field can be included on the boundaries by Eq. (3.25), the normal component of the magnetic field is essentially missing in our 3D FEM model that employs a vector finite element formulation [93, 94], resulting in the reflections in the total decay calculations for the square plasmonic waveguide. However, in Fig. 3.5(a), it appears that the points for which $real(e^{j(\beta L_0+\phi)}) = 0$ holds approximately converge quickly with minimum impact of the reflection from the fundamental hybrid mode. The mode E_{qg}, with effective wavelength of 740.07 nm, is characterized by the material properties of the waveguide and is rather insensitive to the size of the metallic core. Compared with other quasi guided modes or radiation modes, the mode E_{qg} has

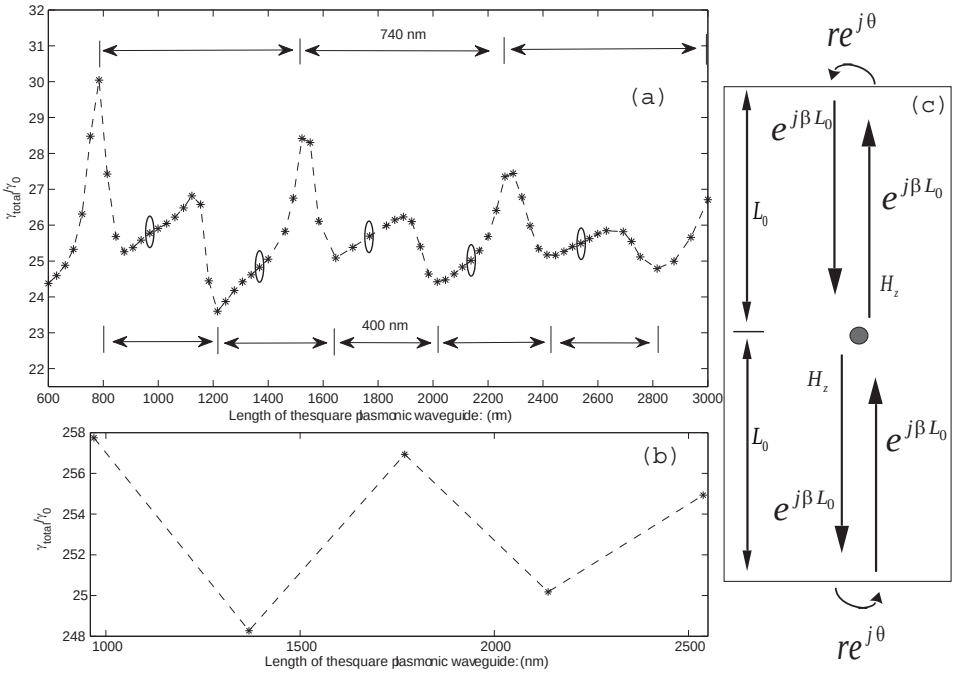

Figure 3.5: (a)Length dependence of the total decay rate for the square plasmonic waveguide. The side length is 30nm, the distance of the emitter to the edge of the square metal core is 20 nm. (b) Length dependence for the points from (a) (marked by ellipses) where $real(e^{j(\beta L_0+\phi)}) = 0$ *holds approximately. (c) Illustration of the reflection of the normal magnetic field of the fundamental hybrid in the 3D model, with* r *and* θ *being the reflection coefficient and phase shift respectively.*

a relatively significant contribution to γ_{total}, the normalized spontaneous emission rate is 0.107. Since no extra effort is made to prevent the reflections of other components of the mode E_{qg}, it is understandable that the induced reflections give rise to several peaks in Fig. 3.5(a).

The normal component of the magnetic field of the fundamental mode in the 3D model can be obtained by a 2D eigenvalue calculation, $H_{n,l} = \sqrt{\frac{\gamma_{pl}P_0}{P_{2d}}}H^n_{2d}e^{j(\beta l+\phi)}$, where l is the distance from the observation plane to the emitter. Similarly, the reflected normal component of the magnetic field at the position of the emitter can be obtained by taking into account the phase shift due to propagation and reflection, $H^r_{n,0} = r\sqrt{\frac{\gamma_{pl}P_0}{P_{2d}}}H^n_{2d}e^{j(2\beta L_0+\phi+\theta)}$, as shown in Fig. 3.5 (c). The reflected normal component of the magnetic field will "generate" a perturbation term E^r_x to the original E_x component, the real part of which is integrated to calculate the total power dissipation. According to Table 3.1, the reflected term E^r_x from the fundamental hybrid mode is given by

$$E^r_x = -\frac{1}{\omega\varepsilon_0\varepsilon(\bar{r})}(\nabla_t \times \bar{n}(r\sqrt{\frac{\gamma_{pl}P_0}{\gamma_0 P_{2d}}}H^z_{2d,m}e^{j(2\beta L_0-\phi+\theta)}))_x. \tag{3.27}$$

The real part of E^r_x can be zero when L_0 is appropriately chosen, therefore, the obtained total decay rates are expected to approach the true values more closely due to the vanishing contribution of E^r_x to the total decay rate. In Fig. 3.5(a), at the points with marked ellipses, the half model length L_0 fits the requirement $(real(E^r_x) = 0)$, and we also found that the phase shift θ is required approximately to be $\pi/2$. Further investigation of the phase shift θ involves technical details regarding the implementation of the vector element formulation of the finite element method, which is beyond the scope of the thesis, we refer to the references [92, 93, 95, 94].

3.2.5 Comparison with quasi-static approximation for metallic nanowire

Due to the tight confinement of the plasmonic mode as well as the geometric slowing down of the mode propagation [47], one can achieve very efficient coupling of a single quantum emitter to metallic nanowires [47], which was previously studied mainly by employing a quasistatic approximation [56]. Here, we quantitatively study the spontaneous emission of an emitter in nanoscale proximity to a plasmonic waveguide beyond the quasistatic approximation, which is necessary when one is concerned with realistic plasmonic waveguides that are compatible with current

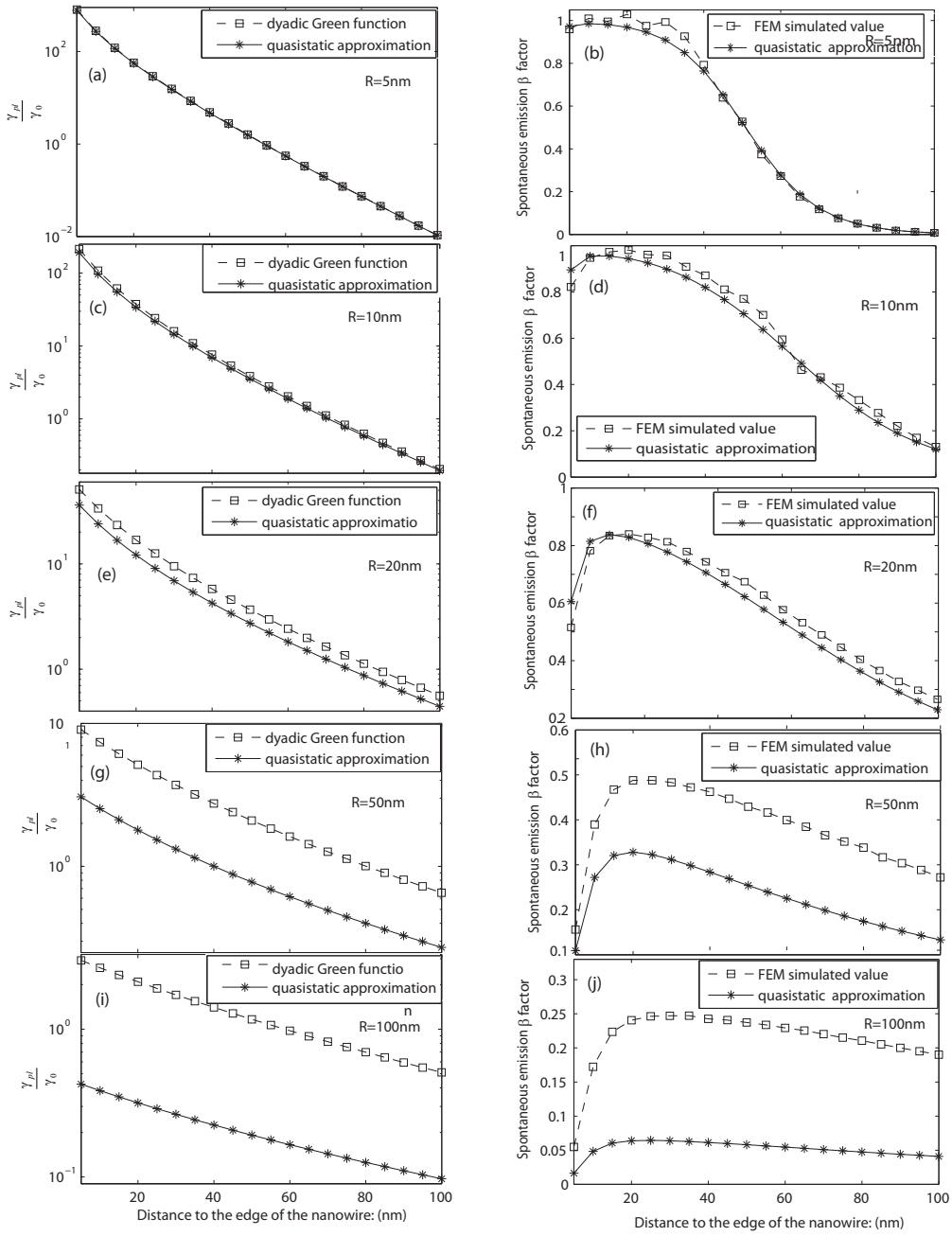

Figure 3.6: Comparison of FEM simulated results based on the dyadic Green's function with the quasistatic approximation for the metallic nanowire.

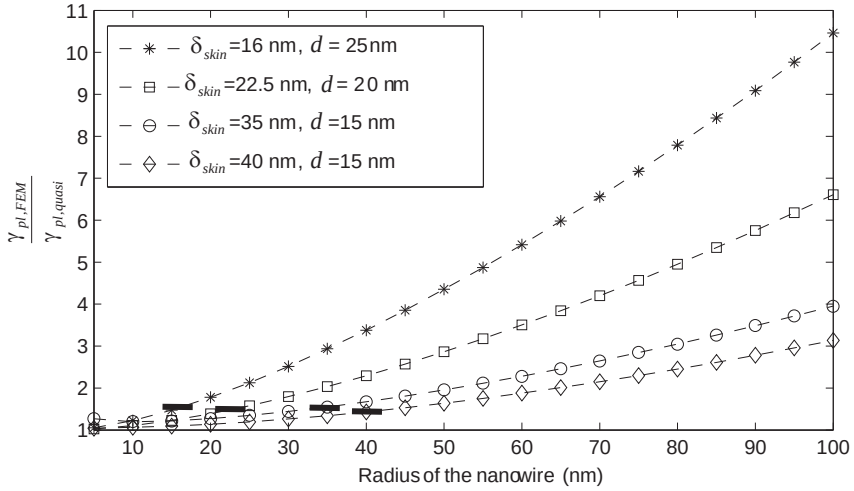

Figure 3.7: The radius dependence of $\frac{\gamma_{pl,FEM}}{\gamma_{pl,quasi}}$ *for four different metals. The skin depths of the four different metals are* 16 *nm*, 22.5 *nm*, 35 *nm*, 40 *nm*, *the corresponding relative optical permittivities are* $-100+3.85i$, $-50+3.85i$, $-20+3.85i$, $-15+3.85i$. *The vacuum wavelength is 1* μ*m.*

nanofabrication technology. Normally it is claimed that the quasistatic approximation is valid when the size of the structure and the distance of the emitter to the surface are substantially less than the radiation wavelength. To resolve this ambiguous criterion, we compare our numerics with the results obtained within the quasistatic approximation and give a qualitative assessment regarding the validity of the quasistatic approximation.

We calculate the full electrodynamic solutions by using the rigid full-vectorial three-dimensional finite element method, as detailed previously. Our numerical values and the quasistatic values of the plasmonic decay rate and spontaneous emission β factor of the gold nanowire with different radius are plotted in Fig. 3.6. The radius of the gold nanowire varies from 5 nm to 100 nm. Fig. 3.6 shows the transition of the quasistatic approximation from approximate to inadequate, depending on the size of the radius, with a cross indicating $R = 20$ nm. According to the deviations between the numerical values and the quasistatic approximated values, the ten subplots associated with different radius in Fig. 3.6 are grouped into three different regimes, namely, the quasistatic approximation regime, the skin depth regime, and the full wave regime in which the quasistatic approximation breaks down. The qua-

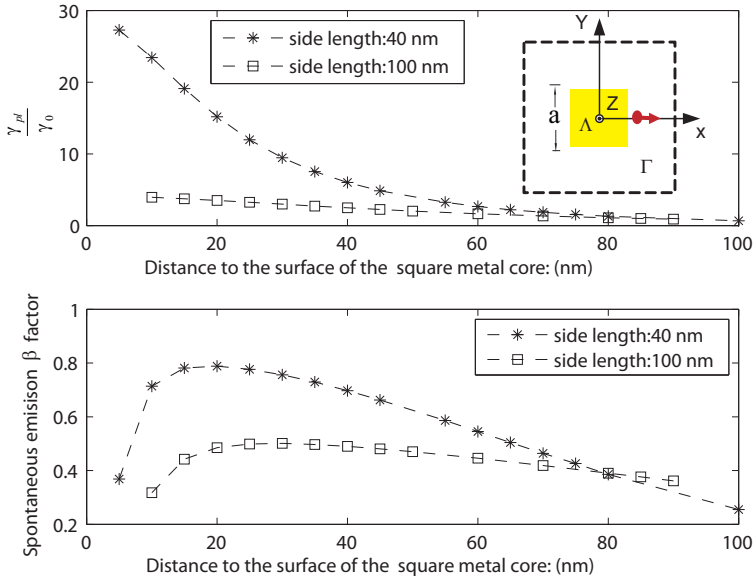

Figure 3.8: Distance dependence of the plasmonic decay rates and spontaneous emission β factors for the square plasmonic waveguide.

sistatic approximation regime is limited to radii of the nanowire less than 10 nm, as shown in Fig. 3.6 (a, b, c, d), where we observe a good agreement between our numerical values and the quasistatic approximated values. In this regime, the radius of the wire is 100 times smaller than the vacuum wavelength, meanwhile the field is strongly localized to an area on the order of the cross section of the gold nanowire, which results in the vanishing of the wave properties in the transverse plane and the applicability of the quasistatic approximation. We also note that in Fig. 3.6 (b) there is a few percent deviation between the FEM simulated spontaneous emission β factor and the quasistatic approximated values due to numerical artifacts, since it is not easy to obtain a good convergence when both the radius of the wire and the distance of the emitter to the wire are very small. For large wires, as indicated in Fig. 3.6 (g, h, i, j), we find significantly larger values of γ_{pl}/γ_0 and the β factor compared to those obtained in the quasistatic approximation. The break down of the quasistatic approximation is due to the incapability of describing the coupling between the electric field and the magnetic field that form the propagating waves,

since the quasistatic approximation assumes that the magnetic field vanishes. One may suspect that one can still obtain reasonable results from the quasistatic approximation if the radius of the nanowire is $\frac{1}{20}$ of the vacuum wavelength, namely 50 nm in our case, since 20 sampling points in one period normally is good enough to resolve the wave properties. However, our numerical calculations, shown in Fig. 3.6 (g, h), indicate that this assumption is incorrect. Even for wires as small as 50 nm, the quasistatic approximation breaks down, consistent with Akimov's experimental work [8]. The full electrodynamic solutions predict significantly larger values, up to 5-10 times, compared with the quasistatic approximation, even though the radius of the nanowire is $\frac{1}{10}$ or $\frac{1}{20}$ of the vacuum wavelength.

Fig. 3.6 (e, f) and others with the size of the radius close to the skin depth are grouped into the skin depth regime. In this regime, the deviation between the full electrodynamic solutions and the quasistatic approximation is somewhere in-between, compared with Fig. 3.6 (a, b, c, d) and Fig. 3.6 (g, h, i, j). To further study the influence of the skin depth and the limitations of the quasistatic approximation, we investigate the radius dependence of $\frac{\gamma_{pl,FEM}}{\gamma_{pl,quasi}}$, which denotes the ratio of the plasmonic decay rate obtained from our numerical method and that of the quasistatic approximation, for metals with different skin depth, cf. Fig. 3.7. In Fig. 3.7, the distance of the emitter to the surface of the metals, i.e., d, is a fixed value for each curve. As can be seen from Fig. 3.7, the deviation between the two results strongly depends on the size of the radius as well as the optical properties of the metals, namely the skin depth. Coincidentally, the ratio of the plasmonic decay rate obtained from our numerical method and the quasistatic approximation for the four different metals is around 1.5 when the radius of the nanowire equals the skin depth. In other words, one can qualitatively assess the validity of the quasistatic approximation by considering the ratio between the radius of the metallic nanowire and the skin depth. The electric field is severely depleted in the center of the metallic nanowire when the radius is larger than the skin depth, and for the fundamental mode the electric field is mediated by the magnetic field, which reaches its maximum in the depletion area of the electric field. However, in the quasistatic approximation there is no magnetic field to couple with the electric field, which significantly impacts the field distribution and reduces the plasmonic decay rate and the spontaneous emission β factor. Based on our numerical calculations, we conclude that the quasistatic approximation is valid only when the radius is smaller than the skin depth of the metals.

3.2.6 Square plasmonic waveguide

To extend the cylindrical wire to other structures, i.e., rectangular metallic waveguide or slot waveguides which are more compatible with current lithographic fabrication technology, we studied the coupling of the quantum emitter with a square plasmonic waveguide as an example. As shown in the inset in Fig. 3.8, the quantum emitter is oriented along the X axis, and the distance dependence of the plasmonic decay rates and spontaneous emission β factors is calculated as function of distance from the emitter to the metal surface along the X axis. For the square plasmonic waveguide, though the electric field of the fundamental mode is concentrated around the four corners, one can achieve an efficient coupling between the plasmonic mode and a horizontally oriented quantum emitter. With optimized side length of the waveguide and distance of the emitter to the edge of the waveguide, the β factor can reach 80%.

3.3 Point dipole model and MESME

The point dipole model is a general method to compute scattering and absorption of electromagnetic waves by point dipole scatterers, which in reality can be particles with arbitrary geometry and composition [88, 96]. The point dipole model is also called the discrete dipole method or coupled dipole method in the literature [48]. In the framework of point dipole approximation, the field inside the discrete scatterers is assumed to be constant so that the excitation of higher-order multiple components in the scattering field can be neglected, which requires that the physical size of each scatter or the discrete volume element inside the scatter should be sufficiently small in comparison both with the light wavelength and distance between the center of the scatterers. For a single particle, the local field corresponds to the incident field. For an ensemble of particles, the local field is a superposition of the incident field and all the scattered field from the rest of particles. To solve such problem, a formalism is needed for solving self-consistently the fields of an arbitrary number of coherently interacting dipoles.

The particles are not necessarily separated. They can also be joint together to form a macroscopic object. Hence, the response of matter to the incident field can be formulated as a collective response of individual point dipoles, each of them occupying a volume element. To illustrate the basic concepts of the point dipole approximation, we consider a chain of separated metallic particles driven by the field $\boldsymbol{E}_{ext}e^{-i\omega t}$, as sketched in Fig. 3.9. We consider a chain of point dipoles spaced

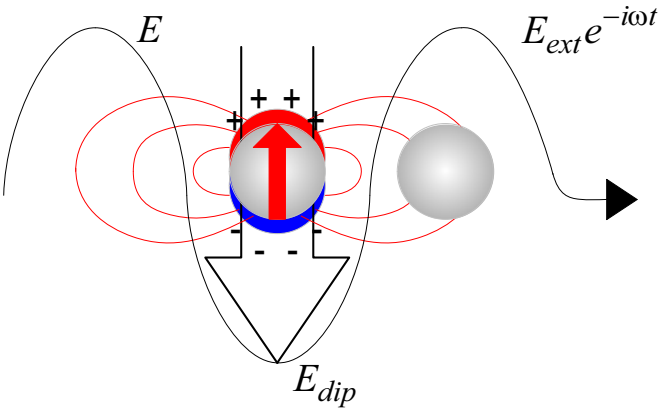

Figure 3.9: Sketch of the point dipole model. The induced field from the polarizability of one point dipole due to the external illumination of light will contribute to the polarizability of other point dipoles.

by a distance d. The electric field generated by a single dipole $\boldsymbol{p}e^{-i\omega t}$, oscillating with frequency ω can be determined as follows [75],

$$E(\boldsymbol{p},\boldsymbol{r},\omega)=\frac{1}{4\pi\epsilon}[(1-\frac{i\omega r}{v})\frac{3(\boldsymbol{r}_0\cdot\boldsymbol{p})\boldsymbol{r}_0-\boldsymbol{p}}{r^3}+\frac{\omega^2}{v^2}\frac{\boldsymbol{p}-(\boldsymbol{r}_0\cdot\boldsymbol{p})\boldsymbol{r}_0}{r}]e^{i\omega r/v-i\omega t}, \quad (3.28)$$

where $\boldsymbol{r}_0$ is the unit vector from the dipole to the field point at distance $\boldsymbol{r}$, $\epsilon=\epsilon_0 n^2$ is the permittivity of the homogenous medium in which the dipole is embedded, and $v=c/n$ is the corresponding speed of light. The polarization induced on nth dipole localized at a position of $\boldsymbol{r}_n$ equals the polarizability $\alpha(\omega)$ times the local field (omitting the frequency factors $e^{-i\omega t}$),

$$\boldsymbol{p}_n=\alpha_n(\omega)\cdot E_{loc}(\boldsymbol{r}_n). \quad (3.29)$$

$\boldsymbol{E}_{loc}(\boldsymbol{r}_n)$ is the sum of the incident field and a contribution from all the other dipoles, described as follows,

$$\boldsymbol{E}_{loc}(\boldsymbol{r}_n)=\boldsymbol{E}_{loc,n}=\boldsymbol{E}_{ext,n}+\sum_{m\neq n}\boldsymbol{E}_{dip}(\boldsymbol{r}_n-\boldsymbol{r}_m) \quad (3.30)$$

where $\boldsymbol{E}_{dip}(\boldsymbol{r}_n-\boldsymbol{r}_m)$ is the electric field on site n scattered by dipole scatter m, i.e., $\boldsymbol{p}_m$. Explicitly the coupled linear equations for the dipole moments $\boldsymbol{p}_n$ for N

dipoles [75] can be written as

$$\begin{aligned}\boldsymbol{p}_n = \alpha(\omega)\{E_{ext,n} + \frac{1}{4\pi\epsilon}\sum_{m\neq n}[(1-\frac{i\omega|n-m|d}{v}) \\ \frac{3(\boldsymbol{r}_0\cdot\boldsymbol{p}_m)\boldsymbol{r}_0-\boldsymbol{p}_m}{|n-m|^3d^3} + \frac{\omega^2}{v^2}\frac{\boldsymbol{p}_m-(\boldsymbol{r}_0\cdot\boldsymbol{p}_m)\boldsymbol{r}_0}{|n-m|d}]e^{i\omega|n-m|d/v}\}.\end{aligned} \tag{3.31}$$

Within the Drude model, the polarizability of a metallic particle in the quasistatic approximation is

$$\alpha_{Drude} = 4\pi R^3\epsilon\frac{\omega_0^2}{\omega_0^2-\omega^2-i\omega\gamma}, \tag{3.32}$$

where R is the radius of particle, $\omega_0 = \omega_P/\sqrt{3}$ is the resonant frequency for the metallic particle, with the bulk plasmon frequency of ω_P and damping term γ defined as in Eq. (2.33). In such dipole limit, i.e., the particle being described by the polarizability α, and the particle is polarized by the external field and in turn is radiates a scattered field. Usually the effective polarizability $\alpha_{eff}(\omega)$ is introduced to account for the radiation reaction to maintain the energy conservation between extinction, scattering and absorption. Hence the radiation damping of itself is included in the polarizability of each nanosphere by [75]

$$\frac{1}{\alpha_{eff}(\omega)} = \frac{1}{\alpha_{Drude}(\omega)} - \frac{i}{6\pi\epsilon}\frac{\omega^3}{c^3}. \tag{3.33}$$

The second term in Eq. (3.33) describes the radiation reaction. It arises from spontaneous emission of radiation by the induced dipole. Equation (3.31) can be reformulated in a compact form as follows

$$\bar{\boldsymbol{M}}\cdot\boldsymbol{p} = \boldsymbol{E}_{ext}. \tag{3.34}$$

For n dipole scatters, $\boldsymbol{p}$ and $\boldsymbol{E}$ is a $3n$-rowed column vector of the dipole moments and $\bar{\boldsymbol{M}}$ is a $3n\times 3n$ matrix. By solving these $3n$ complex linear equations, the polarization $\boldsymbol{p}$ is obtained, and with this, the extinction cross-sections and other properties may be calculated.

Compared with other volume integral methods calculating light scattering, the distinctive feature of the point dipole method is that the solution for the "physically meaningful" internal field, i.e., without the self term for each volume element, is the polarization, which plays an integral role. In other words, any scatters in the framework of point dipole approximation can be replaced by a set of interacting dipoles. However, for larger particles or smaller separation between two neighboring particles, the dipole approximation is not accurate. The accuracy can be substantially improved by employing multipoles expansion for each scatterer.

In the thesis, a multipoles expansion multiple scattering code called "MESME" is also used to calculate light scattering for optical nano-antenna structures [97, 98, 15]. MESME allows to obtain accurate solution to Maxwell's equation for a cluster of objects, including the near field and far field calculations of the scattered field. In MESME, the incident field is first decomposed into multipoles around each object of the cluster, meanwhile the scattered field of and in each object is also expanded in multipoles. Subsequently, the multiple scattering between the objects can be carried out based on the multipoles expansion, which yields a self-consistent solution to scattered field. The self-consistent field can be solved by using a recursion method or an iteration procedure. In the thesis the details of implementing MESME are not explored, since the principle is similar to the point dipole approximation except that a multipoles field other than a dipole field for each scatterer is used. In Chapter 5 MESME is applied directly to calculate the far field emission pattern and the local field at the position of the emitter for predicting the quantum efficiency.

3.4 Conclusion

In this chapter, we have studied several modeling techniques to model single photon devices. First, we have developed a self-consistent model to quantitatively study the spontaneous emission of a quantum emitter at nanoscale proximity to a plasmonic waveguide using the finite element method, which is more precise than the quasistatic approximation. The dyadic Green's function of the guided modes supported by the plasmonic waveguide can be constructed numerically from the eigenmode analysis, and subsequently the normalized decay rate into the plasmonic channel can be extracted. The 3D FEM model has been implemented to calculate the total decay rate, including the radiative decay rate, nonradiative decay rate, and the plasmonic decay rate. In the 3D model, it is assumed that only one guided plasmonic mode is dominatingly excited, which is normally true when the size of the cross section of the plasmonic waveguide is below 100 nm. Under such condition, the spontaneous emission β factor was calculated.

We have discussed the effect of different skin depth on the plasmonic coupling. The skin depth is used as a physical basis for the discussion on comparison between our numerical approach with the quasistatic approximation for the gold nanowire. For the cylindrical metallic nanowire we have observed good agreement with the quasistatic approximation for radii below 10 nm, but for increasing radius the spontaneous emission β factor and the plasmonic decay rate deviate substantially, by

factors of up to 5-10 for a radius of $\sim$ 100 nm, from the values obtained in the quasistatic approximation. We have shown that the quasistatic approximation is typically valid when the radius is less than the skin depth of the metals at optical frequencies. For the square metallic waveguide we have estimated an optimized value for the spontaneous emission β factor up to 80%. In second part, we have briefly discussed the point dipole approximation and MESME.

Chapter 4

Single optical plasmon generation based on single quantum dot coupled to metallic slot waveguide

In this chapter, first we give an overview of the single photon sources, including the special properties of such non-classical light, different light sources (emitters) for generating single photons. In particular, we give a special emphasis on one type of emitter, i.e., the self assembled quantum dot. The electronic structures and the optical properties of the InAs/GaAs quantum dots are briefly discussed. In the second part, we study the spontaneous decay and waveguide mode coupling of a self-assembled quantum dot coupled to a metallic slot waveguide for the single optical plasmons generations, which can be coupled out as efficient single photon sources. We focus on the coupling efficiency, i.e., the SE β-factor, of the quantum dot coupled to the single plasmonic mode with special emphasis on analyzing the impact of the inhomogeneity of the surrounding material. We numerically calculate both the plasmonic decay rate and the total decay rate of the QD using the full 3D FEM model as detailed in Chapter 3. Our results show that the presence of leaky modes due to the inhomogeneity fairly affects the plasmonic decay rate, while the SE β-factor is substantially reduced. We find that by decreasing the index contrast

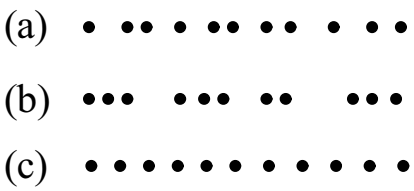

Figure 4.1: Comparison between the photon streams for (a) coherent light sources, (b) chaotic light sources and (c) the single photon light sources.

within realistic experimental bounds, the SE β-factor can be increased by more than a factor of 2.

4.1 Single photon sources and optical properties of self-assembled quantum dots

4.1.1 Properties of single photon states

In order to better grasp the original features of single photon sources with respect to standard light sources, it is necessary to compare the statistic properties of the light produced by a lamp (chaotic light) or by a laser (coherent light). The "grainy" nature of light yields some quantum effects which have to resort to the full quantization theory of light. In the quantum picture of light, a light beam is considered as a stream of photons. A light beam will nevertheless have random photon number fluctuations at short time intervals, though the beam may have a well defined power-flux, which is essentially due to the discrete nature of the photons. Such fluctuations in photon number is dubbed photon statistics of the light [99]. The first serious attempt to measure the fluctuations in the light intensity on short time scales was made by Brown and Twiss [100]. Their experiments on correlations between the star-light intensities recorded on two separated detectors opened the door to more advanced experiments that would utterly lead to genuine quantum phenomenons, e.g., single photon states [101], and other squeezed light [102]. Depending on the distinctions among the different light sources, the photon statistics of the corresponding emitted light presents a clear different behavior [103], as shown in Fig. 4.1.

A perfectly coherent light beam emitted by an ideal single-mode laser can be represented as an electromagnetic wave with a fixed amplitude, frequency and phase,

which is defined as follows,

$$E(t) = \boldsymbol{E}_0(\boldsymbol{r})\mathtt{sin}(\boldsymbol{k}\cdot\boldsymbol{r} - \omega t + \phi). \tag{4.1}$$

The average photon flux, i.e., the intensity of such beam is perfectly constant. However, the photon statistics of such beam has a Poissonian distribution, which is uniquely characterized by the mean value $\bar{n}$. The fluctuations of a statistical distribution from the mean value are quantified in terms of the variance. It is well-known that for Poissonian distribution that the variance is equal to the mean value [31]. Based on Poissonian properties, Glauber constructed the quantum representation of such a wave called a coherent state $|\alpha\rangle$, which is expanded in the basis of number-states, i.e., $|\alpha\rangle = e^{-|\alpha|^2/2}\sum_n \frac{\alpha^n}{\sqrt{n!}}|n\rangle$ [55]. Coherent states are also called quasi-classical states, since its quantum-mechanical average approaches that of the classical wave with stable amplitude and fixed phase defined by Eq. (4.1) in the limit of strong excitation. While for a thermal light from a black-body sources or the chaotic light from discharge lamps, the fluctuation in photon number is larger than its mean value, which is normally referred as super-Poissonian distribution. Number-states, single-photon states in particular are non-classical states. More specifically, they are special cases of squeezed light, the quantum fluctuation of which on the photon number component has been squeezed. An ideal amplitude-squeezed source would be one delivering a regular stream of photons at regular time intervals, and a single-photon source is a good example of it, cf. Fig. 4.1 (c). Thus the fluctuations of the number of the photon emitted from a squeezed light sources are weaker than those of a coherent light sources.

A rigorous treatment of classifying a light beam in terms of photon statistics is called $g^2(\tau)$ function, which measures the probability of detecting a second photon at time $t = \tau$ given the occurrence of detecting one photon at $t = 0$ [31, 99]. The $g^2(\tau)$ function is also called the intensity correlation function, or conditional photon probabilities in quantum picture. Neglecting spatial coherence aspects, one can simplify the $g^2(\tau)$ function as follows [99],

$$g^2(\tau) = \frac{\langle \bar{I}(t)\bar{I}(t+\tau)\rangle}{\bar{I}^2} = \frac{\langle E^*(t)E^*(t+\tau)E(t)E(t+\tau)\rangle}{\langle E^*(t)E(t)\rangle^2}. \tag{4.2}$$

where $\bar{I}$ is the long-time average intensity, and $\langle \bar{I}(t)\bar{I}(t+\tau)\rangle$ is defined as $\langle \bar{I}(t)\bar{I}(t+\tau)\rangle = \frac{1}{T}\int_T dt\bar{I}(t)\bar{I}(t+\tau)$. For a chaotic light, the value $g^2(\tau = 0) = 2$ indicates that thermal light has larger intensity fluctuations, and the total field strongly fluctuates around zero, its most likely vale [31]. Such statistical tendency of photons

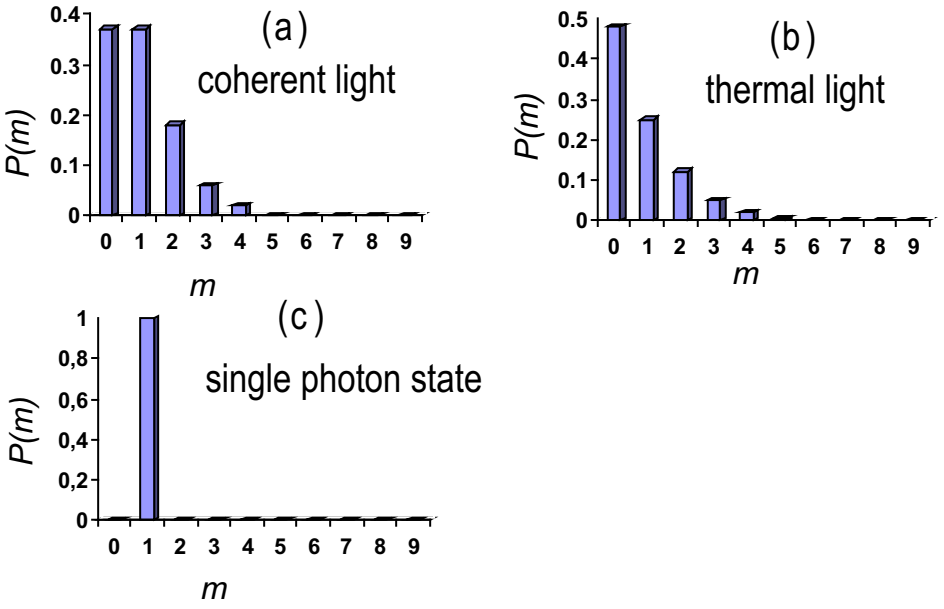

Figure 4.2: Comparison of probability distribution of the number of photons with a mean photon number $\langle n \rangle = 1$ for (a) coherent light sources, (b) chaotic light sources and (c) the single photon light sources.

to accumulate in photon stream of chaotic light beam is called photon bunching. For a coherent light, there is non intensity fluctuations in classical picture, and thus no photon bunches in the quantum pictures either. The complete randomness of the timing between the photons, cf. Fig. 4.1 (a), follows from the random nature of the Poissonian statistics. The fact that $g^2(\tau) = 1$ for coherent light can be interpreted as a manifestation of the randomness of the Poissonian photon statistics. For the perfect single photon states, shown in Fig. 4.1 (c), the spacing of photons in the flow is completely regular and thus $g^2(\tau) = 0$. Figure 4.2 shows the probability distribution of photons for three sources with an average photon number $\langle n \rangle = 1$. The chaotic light sources indicates large number fluctuations. The coherent light source presents a Poissonian distribution, narrower than the chaotic light. A single photon source can match this distribution by delivering single photons at regular time intervals.

There are a broad ranges of applications that substantially relies on the single

photon sources [104]. In quantum cryptography, two partners can exchange an encryption key as a stream of quantum bits (photons) and detect eavesdropping on their communication line via the perturbation caused by the spy's measurements [105, 106]. Single-photon sources improve the degree of security of the quantum transmission by making it more difficult for the spy to hide her measurement actions. Another potential use for single photons exploits entanglement, a key feature of quantum mechanics [107]. In the last 15 years, a more and more precise roadmap for all-optical quantum computing has been traced by a series of pioneering theoretical papers [108, 109]. The schemes they propose are based on linear optics, the only nonlinearity required for computing being contained in the measurement process itself. Single-photon states play a central part in these linear optical quantum computers. Bright and reliable sources of single photons would greatly help to explore and demonstrate their working principles and, more generally, those of quantum teleportation, quantum networks and other fascinating quantum phenomena. Efficient single photon sources also have significant impacts on the single molecule spectroscopy and weak absorption measurements.

The potential ability of quantum computing relies on interference between two single photons. In order to give rise to a fully destructive interference, the two photons must be completely undistinguishable. For two identical photons described by the same wavepacket, and with the same the arrival time on the beam splitter, the two photons will emerge together at the output port of the beam splitter due to the quantum interference [110, 111], which are rather essential for quantum computing and is ultimately determined by the indistinguishability of the two photons. Therefore, it is desirable to develop efficient and coherent single photon sources for quantum information technology.

4.1.2 Light sources for single photon generation

There are two major categories of generating single photon states, i.e., using macroscopic sources or using microscopic sources [103]. Strongly attenuated light beams generated from a single mode laser and spontaneous parametric down-conversion sources in nonlinear crystals fall into the first category. The photon statistics from such faint lasers obeys Poissonian distribution, hence the two-photon rate grows as the single-photon rate squared. To reduce the multi-photon rate, the single-photon rate must be kept small, which fundamentally limits the repetition rate and the efficiency of the single-photon emission [106]. Lütkenhaus also pointed out there is also an optimal mean value when the transmission loss is included [112]. Another

type of pseudo single photon states called heralded single photon sources is the photon pairs generated from spontaneous parametric down conversion in a non-linear crystal. Since the photons are created in pairs, the detection of one photon can be used to announce of the existence of the other photon [113].

The second category of generating single photon states is to use various microscopic single emitters, such as atoms, ions, organic molecules, polymers, color centers and semiconductor nanocrystals. By collecting the fluorescence photons from such single quantum emitter, one can ensure that one single photon is generated. In the following, we will briefly study their photophysical properties, as well as their advantages and weaknesses of these different emitters. There are two criteria for evaluating the figure of merit of the single photon sources: (I) The quantum yield of the emitters needs to be as high as possible for an efficient single photon sources; (II) In order to produce identical temporal profiles of the single photon wavepackets, the exciton of the emitter should be solely radiatively broadened and there is no jitter in the emission time [114].

Atoms and ions, e.g., the cold atoms and the trapped ions, are characterized by purely electronic eigenstates with hyperfine structure, the transitions of which are narrow and life-time limited [115, 116]. Besides, the emission on the vibrational sidebands can be negligible. Hence, the emitted single photon wavepackets are transformed-limited, and can be perfectly indistinguishable. However, producing single photon sources from such type of emitter requires advanced and expensive setup to isolate, manipulate and trap single atoms. The operation time of such atom-based single photon sources is also challenged by the dwell time of the atom in the cavity mode.

Organic molecules can also provide a high quantum yield in the fluorescence and were the first condensed-matter system for the antibunching demonstration [117]. Compared with atoms, the eigenstates of molecules in condensed matter involve vibrations and phonons, in addition to electronic states. Consequently, a transition to an excited electronic state is distributed over a broad range of frequencies with the creation of additional vibrations and phonons [48]. Under low-temperature conditions, the fluorescence of single molecules shows deep antibunching and damped Rabi oscillation [118]. Aromatic molecules were used for an early demonstration of a single-photon source in condensed matter [117]. At room temperature, the thermal motions cause fast dephasing, which gives rise to very broad absorption and emission bands. Meanwhile, the thermal effect at room temperature also induces the instability of photophysical properties of the molecules. Nevertheless, it was

observed that the fluorescence of single molecules at room temperature also shows very strong antibunching [119, 120]. It was shown that single molecules can operate as single-photon sources [121, 122].

Color centers are defects of insulating crystals. A perfect diamond free from such defects is colorless, it is the defects that give the diamond different colors. It is well known that color centers present strong absorption and fluorescence bands or lines, which stem from localized electronic states around interstitial or substitutional impurities, vacancies, inserted charge carriers or combination thereof. In particular, the nitrogen-vacancy (NV) color centers in diamond show excellent photonstability in their fluorescence emission spectrum, even at room temperature, due to their mechanical stiffness and stability [123]. When optically pumped, an isolated nitrogen-vacancy center emits single photons of visible light, making diamond a promising solid-state room temperature light source for application in quantum information processing. The efficiency of the single photon emission from an isolated nitrogen-vacancy center in bulk diamond is normally limited in the high refractive index, nevertheless, it was shown recently that an efficient single photon source based on an array of nanopillars in diamond can be achieved [124].

Chemical synthesized core-shell nanocrystals, also called colloidal quantum dots, are composed of an inorganic core surrounded by an organic outer layer of surfactant molecules. In such core/shell nanocrystals, the shell provides a physical barrier between the optically active core and the surrounding medium, thus making the nanocrystals less sensitive to environmental changes, surface chemistry, and photooxidation [103]. The shell further provides an efficient passivation of the surface trap states, giving rise to a strongly enhanced fluorescence quantum yield. It was shown under certain condition that the emission quantum yield can be very close to unity. At room temperature, the emission spectrum of the zero phonon line is broadened to 50 meV by dephasing and spectrum diffusion and thus far from the lifetime-limited [103]. At low temperature, the emission line narrows significantly, but has challenges of producing indistinguishable single photons. Besides, the composition of thousands of atoms in such semiconductor nanocrystals can also support multiple excitations. Therefore, the elimination of multi-excitations is crucial in the strong antibunching observed in nanocrystals and enables their use as single photon sources [125, 126].

Apart from the self-assembled quantum dots (QDs) which will be described later, the main features of single quantum system in view of applications as single photon sources are briefly discussed. The choice of a quantum emitter substantially

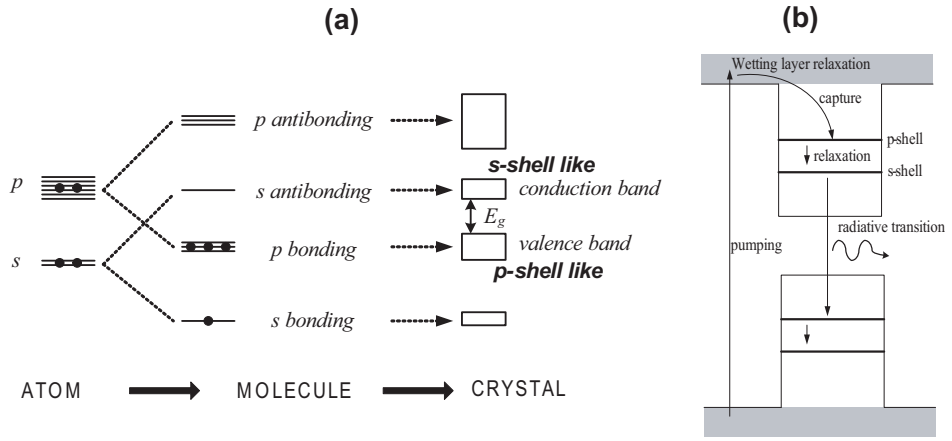

Figure 4.3: (a) Bands in InAs/GaAS semiconductor bulk material formed from hybridization of atomic orbitals. (b) Sketch of energy levels in a QD with two shells for the carriers in the conduction and valence band respectively. The shaded areas indicate the wetting layer.

depends upon the intended application of the single photon sources.

4.1.3 Electronic structure and optical properties of InAs/GaAS self-assembled quantum dots

Self-assembled QDs are islands of a low-band-gap semiconductor embedded in a high-band-gap semiconductor, for example InAs in GaAs [127]. Due to a consequence of lattice-mismatch between the deposited material and the underlying substrate, such self-assembled QDs can be formed spontaneously under certain growth conditions, resulting with three-dimensional islands standing on a two-dimensional wetting layer, which can be subsequently buried to realize quantum confinement. Self-assembled QDs give the possibilities of tailor their size, shape, composition and location to a larger extent, compared with others, e.g., chemically synthesized QDs. In addition, they can be embedded naturally during growth into more complex structures for advanced optoelectronic devices.

The energy levels of electrons in the semiconductor crystal InAs/GaAS predetermine part of the electrons' behavior in the InAs/GaAS self-assembled QDs. As shown in Fig. 4.3 (a), the isolated energy level of the electron is split into two levels when two atoms are in close proximity and have to be treated as a coupled system.

When N atoms are bound and coupled together, then each atomic energy level of the constituent atoms splits into a band of N discrete energy levels. One also notes the conduction band minimum is built from atomic orbitals with s-like symmetry, while the valence band maximum is built from atom orbitals with p-like symmetry [128]. Due to the nanometer scale potential confinement of the electrons inside InAs/GaAS self-assembled QDs, the energy levels become discrete [129]. A sketch of energy levels of conduction and valence band states in the vicinity of the optical band gap is shown in Fig. 4.3 (b).

The electronic properties of InAs/GaAS self-assembled QDs are determined by the confined electrons' wave functions. The crystal potential of the electrons inside of the QDs can be approximately split into (I) a complex atomic-scale potential which is periodic with the crystal lattice of InAs and (II) a macroscopic potential imposed by the heterostructure between InAs and GaAs. Hence, the electron (hole) wave function can be written as the the product of two functions [128],

$$\psi_{e/h}(\boldsymbol{r}) = F_{e/h}(\boldsymbol{r}) \cdot u_{e/h}(\boldsymbol{r}), \tag{4.3}$$

where $F_e(\boldsymbol{r})$ ($F_h(\boldsymbol{r})$) is the envelope function of the electron (hole) and $u_e(\boldsymbol{r})$ ($u_h(\boldsymbol{r})$) is the Bloch function of the conduction band electron (valence band hole). The properties of Bloch function $u_{e/h}(\boldsymbol{r})$ are primarily determined by the crystal structures as sketched in Fig. 4.3 (a), while the envelop function $F_{e/h}(\boldsymbol{r})$ is determined by the nanometer scale potential confinement, cf., Fig. 4.3 (b). Thus $u_e(\boldsymbol{r})$ for the conduction band electron has the s-like symmetry, while $u_h(\boldsymbol{r})$ valence band hole has the p-like symmetry. The overlap of the electron wave function with the hole wave function determines the intrinsic coupling strength of the QDs coupled to light.

The optical properties of InAs/GaAS self-assembled QDs can be understood by considering the electronic shell structure, the spin structure, and the many-body interaction between the electrons and the holes [130]. For neutral QDs, the exciton (one electron and one hole), biexciton (two electrons and two holes) and multi-exciton can be observed [131]. For charged QDs, the transition presents different features due to the Coulomb correlations between the carriers [132]. In principle, optical emission from the such a nanoscale object can be used as single photon sources by spectral filtering. The properties of the emitted single photons from such nanocrystals, e.g., internal quantum efficiency, jitter, coherence time, critically depend on the excitation process. As sketched in Fig. 4.3 (b), the QDs are optically pumped by generated electron-hole pairs in the wetting layer, which subsequently are captured by the QDs and relax to the lowest energy level within a

short time scale (1-100 ps) [129]. The pumping technique sketched Fig. 4.3 (b) is called non-resonant excitation. Besides, the QDs can also be excited by pumping p-shell or s-shell directly, which are referred as quasiresonant excitation and resonant excitation. Each excitation technique has its own advantages and drawbacks [129], regarding development of a perfect single photon source. Recently, self-assembled QDs based single photon sources coupled to various photonic structures have been demonstrated [133, 134, 135, 2, 9, 136], indicating a promising future of self-assembled QD based devices for quantum information technology.

4.2 Single optical plasmon generation based on quantum dot coupled metallic slot waveguide

4.2.1 Overview of QDs coupled to metallic slot waveguides

Due to their strong carrier confinement, small size, and long coherence time, semiconductor QDs are expected to have significant impact on scalable quantum computing systems [137] and non-classical light sources employed in quantum communication technology. It is thus important to develop solid-state solutions, and the semiconductor technology benefits from an existing industry and possibility of integration with other functionalities. Whatever kind of quantum mechanical degree of freedom is used, it is always desirable to achieve a very efficient coupling between a flying photonic qubit and a stationary qubit, which might function as an interface between the quantum communication system and the quantum computation system. Recently it has been proposed and experimentally demonstrated that a single quantum emitter can be efficiently coupled to surface plasmon polaritons [8, 9]. The plasmonic enhancement of light-matter interaction provides new possibilities for developing efficient single-photon sources and for mapping a quantum dot based qubit to a photonic qubit, or vice versa. We investigate such plasmonic induced enhancement of light-matter interaction, especially the preferential emission from semiconductor QDs into a desired mode supported by a realistic plasmonic waveguide, for developing efficient single-photon sources. The structure under examination is illustrated in Fig. 4.4 (a), showing a single self-assembled QD coupled to lithographically fabricated metallic slot waveguides [89]. Compared with other chemically grown metallic nanowires with a distribution of length and radius, the lithographic wires mainly have two advantages: (1) the self-assembled QDs can be positioned in the plane (X-Z plane) [138], as well as along the vertical direction

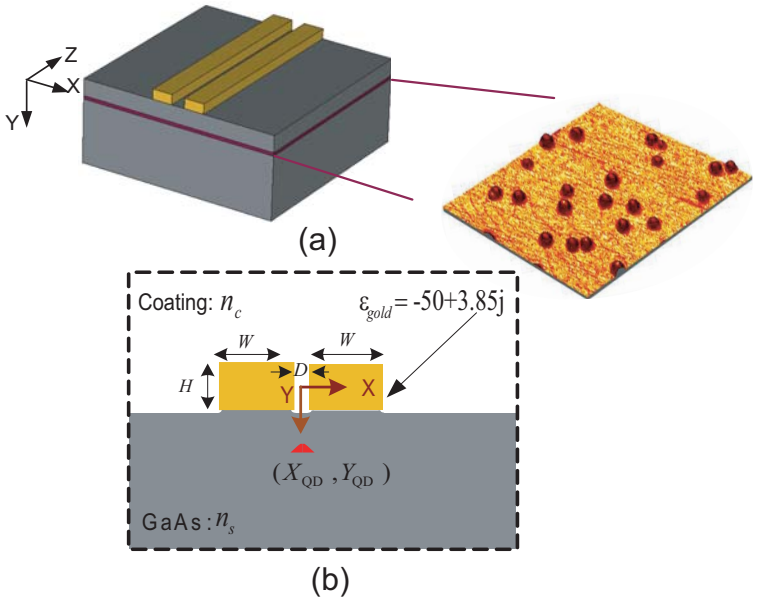

Figure 4.4: (a) Sketch of QDs coupled to a metallic slot waveguide. The inserted AFM image illustrates self-assembled InAs/GaAs QDs. (b) Cross section of the metallic slot waveguide with width, height, and gap width denoted by W, H, and D, respectively.

(Y-axis); (2) the metallic slot waveguide can be fabricated lithographically [139] with controllable sizes W, H, D, as illustrated in Fig. 4.4 (b). Meanwhile, such structures also lead to challenges since the QD emission can be quenched at interfaces [140] thus limiting how close to the plasmonic waveguide the QDs can be positioned, and in addition any inhomogeneity due to different refractive indices of the substrate and coating material is found to reduce the coupling.

In general, QDs placed near a plasmonic waveguide are subjected to multiple decay channels, namely the radiative decay channel, the non-radiative decay channel, and the plasmonic decay channel. The corresponding decay rates are denoted by γ_{rad}, γ_{nonrad}, and γ_{pl}, respectively. One notes that due to the interference between forward and backward traveling guided plasmonic modes, the localized plasmonic resonant modes in either X or Y directions can also be excited, which could substantially contribute to SE of the QD and subsequently scatter the emission out of the structure. However, the parameters of gap structure used in the section are away

from localized plasmonic resonance conditions. In addition, the measured internal quantum efficiency for the typical QDs that we are considering are 90% according to reference [140], which can be further increased by tuning the sizes. In this section the internal quantum efficiency of the self-assembled QD is assumed to be 100%. Hence the resistive heating of the metallic waveguide is the only mechanism of non-radiative relaxation considered. Therefore, in our case the plasmonic decay channel is dominating over SE from the QDs, and a larger plasmonic decay rate can be used to extract coherent single photons with less influence from dephasing process of the QDs. The SE β-factor, given as the SE decay rate for coupling to the gap mode divided by the total decay rate, i.e., $\beta = \gamma_{pl}/(\gamma_{rad} + \gamma_{nonrad} + \gamma_{pl})$, is the figure of merit of the single-photon source efficiency, which describes the fraction of the emitted energy that is coupled to the single plasmonic mode. Therefore, it is desirable to achieve, simultaneously a high plasmonic excitation rate and a high SE β-factor in the context of developing efficient and coherent single-photon sources.

4.2.2 Geometry and mode properties of the metallic slot waveguide

We study the metallic slot waveguide shown in Fig. 4.4, consisting of two gold strips ($\varepsilon_{gold} = -50 + 3.85j$), a layer of quantum dots and a GaAs substrate, at the wavelength of 1000 nm. The electrodes are covered by a coating material with refractive index n_c. The geometric parameters of the waveguide and position of the single QD are illustrated in Fig. 4.4 (b). Throughout this section, the origin of the coordinate system for the QDs, e.g., ($X_{\mathtt{QDs}}$,$Y_{\mathtt{QDs}}$), is at the very middle of the gap. The calculated effective index of the guided modes versus the width of the metallic strip (W) is shown in Fig. 4.5 (a) with fixed values of the other parameters ($n_c = 1.5$, $H = 40$ nm, $D = 30$ nm), and indicates a cutoff value of W for the higher order modes. Hence, with the typical width and height illustrated in Fig. 4.5 (b,c), such a structure can support only two guided plasmonic modes, one with E-field concentrated in the gap (gap mode) and one with E-field concentrated at the corners outside the gap (separated mode). As shown in the inset of Fig. 4.5 (a), the propagation length of the gap mode is around 1 μm, which only allows to use as short plasmon waveguides. More specifically, the plasmons need to be coupled to dielectric waveguides within a few hundred nano meters ($4 \sim 5$ optical cycles), to avoid excessive propagation damping due to the losses of the metals.

Zia et al. [141] studied a thin Au film mounted on a fused silica substrate with

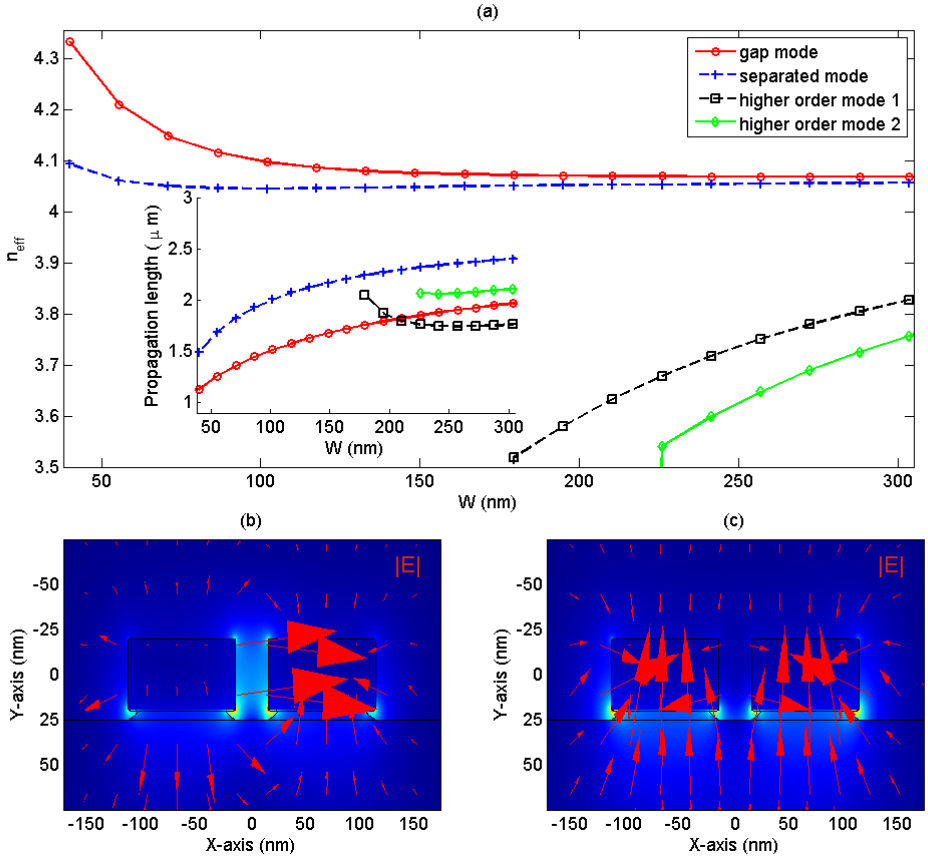

Figure 4.5: (a) Effective mode index (n_{eff}) versus width of the gold strip (W) positioned on top of the GaAs substrate, with the material indices of $n_c = 1.5$, and $n_s = 3.5$. (b,c) Magnitude and orientation of the electric field in the X-Y plane for the gap mode and the separated mode for metallic waveguide with dimensions $W = 100$ nm, $D = 30nm$, $H = 40nm$. The field orientations are given by the red arrows, the length of which give the amplitude of the electric field. Inset in (a): Propagation length (field amplitude $1/e$ lengths) of the guided plasmonic modes versus W.

air on top, which is a typical plasmonic waveguide with inhomogeneous environment examined extensively in both theory and experiment. In [141] it was found that the bounded modes are localized at the glass-Au interface, while the leaky plasmonic modes are localized at the air-Au interface. Similarly, the complete modal description of the metallic slot waveguide studied in this section consists of leaky modes that are characterized by effective mode indices below n_s, in addition to the gap mode and the separated mode. Depending on whether the effective mode index of these leaky modes is smaller or large than n_c, the leaky modes are entitled either radiation modes or leaky plasmonic modes in this section. The radiation modes can penetrate through both the substrate and the coating area and leak away, while the leaky plasmonic modes are still confined in the coating area, and can only leak away through the substrate. Due to the plasmonic features, i.e., the tight confinement of the field in the coating area as well as large field enhancement close to metals, the leaky plasmonic modes are expected to have a larger impact on the SE β-factor than the radiation modes, since the QDs are localized in the area close to the metals.

4.2.3 Theory

In this section we briefly outline the theoretical foundation, for further details see Refs [11, 90]. By employing first order perturbation theory, one can use Fermi's Golden Rule [48] to calculate the decay rate of a quantum emitter,

$$\gamma = \frac{\pi\omega_0}{3\hbar\varepsilon_0}|\mu|^2\rho_\mu(r_0,\omega_0), \tag{4.4}$$

where μ is the transition dipole moment of the quantum emitter, ρ_μ is the projected local density of states, ω_0 is the atomic transition frequency, and ε_0 is the vacuum permittivity. The projected local density of states ρ_μ predicts the available number of optical modes for a dipole located at r_0 with orientation of n_μ. The dyadic Green's function $\bar{\boldsymbol{G}}(\boldsymbol{r},\boldsymbol{r}',\omega_0)\}$, defined by $[\nabla\times\nabla\times-k_0^2\varepsilon(\boldsymbol{r})]\bar{\boldsymbol{G}}(\boldsymbol{r},\boldsymbol{r}',\omega_0)\} - \boldsymbol{I_0}\delta(\boldsymbol{r}-\boldsymbol{r}') = 0$, contains all the classical information of the electromagnetic waves and can be expanded in a set of eigenmodes. The dyadic Green's function can be split into a traverse part and a longitudinal part. Since we are studying the propagating modes, which describe the field solution in the absence of free electric charges, the longitudinal component will vanish in the following calculations. For a typical index contrast waveguide with the cladding material of ε_2, the modal description of the dyadic Green's function, more specifically the transverse part, can be formulated as

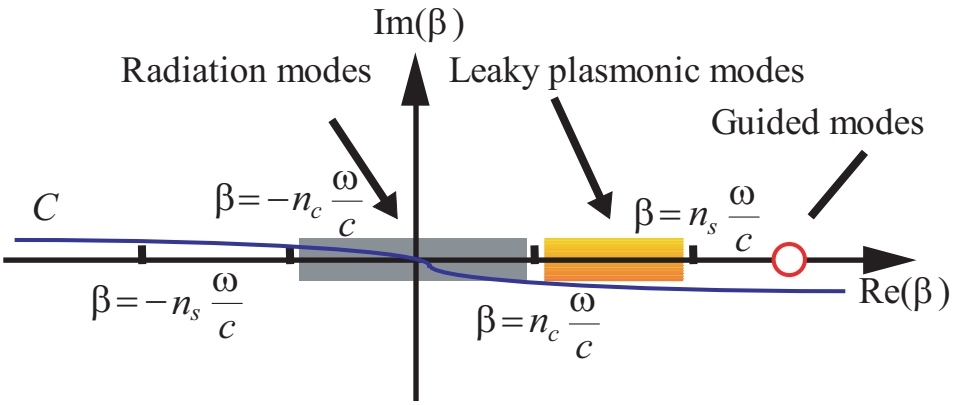

Figure 4.6: Illustration of evaluating the integral representation of the dyadic Green's function. The discrete poles yield the contribution to the decay rates into the guided modes, while the gray and the yellow regions represent the continuum contributions to the radiation modes and the leaky plasmonic modes, respectively. The blue line C denotes the full integration path.

follows,

$$\bar{\boldsymbol{G}}(\boldsymbol{r},\boldsymbol{r}',\omega)=\sum_{p}\int_{0}^{+\infty}\int_{-\infty}^{+\infty}\frac{\varepsilon_2\boldsymbol{E}_\alpha(x,y)[\boldsymbol{E}_\alpha^\dagger(x',y')]^* e^{j\beta(z-z')}}{[k_0^2\varepsilon_2-(\beta^2+k_{2\perp}^2)]N_\alpha}d\beta dk_{2\perp}, \tag{4.5}$$

where $\boldsymbol{E}_\alpha(x,y)e^{-j(\omega_0 t-\beta z)}$ is the waveguide eigenmode labeled by α, found from the wave equation $\nabla\times\nabla\times\boldsymbol{E}(\boldsymbol{r})-k_0^2\varepsilon(r)\boldsymbol{E}(r)=0$. Here, β is the longitudinal wave vector, $k_{2\perp}$ is the transverse wave vector in the cladding materials, and N_α is normalization factor defined by $N_\alpha=2\pi\int\varepsilon(x,y)\boldsymbol{E}_\alpha(x,y)\cdot[\boldsymbol{E}_\alpha^\dagger(x,y)]^*dxdy$. Equation (4.5) gives the complete description of the modes, including guided modes as well as leaky modes, supported by the wave guides. For the leaky modes, β and $k_{2\perp}$ can be chosen independently, while for the guided modes β and $k_{2\perp}$ are not independent.

As can be seen from Fig. 4.6, there are three types of contributions to the full integration range, i.e., the gray region, the yellow region, and the poles, which represent the radiation modes, leaky plasmonic modes and the guided modes, respectively. For a homogenous environment, the region with leaky plasmonic modes ($n_c<\beta<n_s$) vanishes since $n_c=n_s$. By picking up the pole contributions from

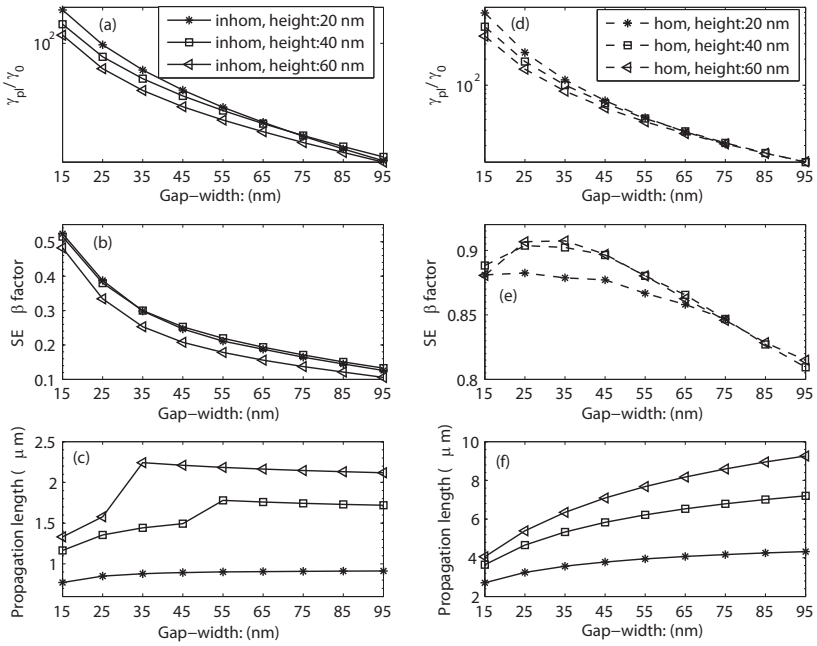

Figure 4.7: Gap-width dependence of the plasmonic decay rates, SE β-factors, and the propagation length of the gap mode for an inhomogeneous dielectric environment (a, b, c) and for a homogenous dielectric environment (d, e, f). In the subplot (a, b, c), $n_c = 1.5$, $W = 100$ nm and $n_s = 3.5$, while for homogenous case in the subplot (d, e, f), the surrounding material is air ($n_{air} = 1.0$), and $W = 100$ nm.

the full integration range C, as illustrated in Fig. 4.6, one can extract the single guided mode contribution. The normalized rate describing decay to a specific guided plasmonic mode denoted by α_0 for a QD with horizontal dipole moment is given by,

$$\frac{\gamma_{pl}}{\gamma_0} = \frac{6\pi^2 c^3 E_{\alpha_0,x}(x,y)[E^{\dagger}_{\alpha_0,x}(x,y)]^*}{\omega_0^2 N_\alpha \upsilon_g}, \tag{4.6}$$

where υ_g is the group velocity, $E_{\alpha_0,x}$ denotes the x component of the electric field of the guided plasmonic mode, and γ_0 is the SE decay rate in vacuum. The plasmonic decay rate is proportional to the field strength divided by the group velocity, which means that the emitter can release the energy to the plasmonic mode faster and more efficiently if the plasmonic mode concentrates and slows down. The total decay rate, γ_{total}, is extracted from the total power dissipation of the current source coupled to the nearby metallic waveguide from a 3D finite element model, $\gamma_{total}/\gamma_0 = P_{total}/P_0$, where $P_{total} = 1/2 \int_V \mathtt{Re}(\boldsymbol{J}^* \cdot \boldsymbol{E}_{total}) dV$ is the power dissipation of the current source coupled to the metallic waveguide, and $P_0 = 1/2 \int_V \mathtt{Re}(\boldsymbol{J}^* \cdot \boldsymbol{E}_0) dV$ is the emitted power by the same current source in vacuum. Using a similar strategy, we study the length dependence of the total decay rate for the 3D finite element model to check the validity of the mode matching boundary condition that is used to absorb the gap mode, as well as the accuracy of our numerical model. We also observe the oscillations of the total decay rate due to the reflections of the radiation modes and the guided mode, as expected. Accordingly, we estimate the relative error in the calculations to be 2.5%. We refer to Chapter 3 for details on the implementation of the 3D finite element model.

4.2.4 Single optical plasmon generation and influence of inhomogeneity

From Fig. 4.5 (b,c), we see that the gap mode is primarily polarized along the X axis, while the separated mode is primarily polarized along the Y axis. Therefore, for a horizontally (vertically) oriented quantum emitter, only the gap (separated) mode will be excited, while emission into the separated (gap) mode will be suppressed. Self-assembled QDs have dominating in-plane transition dipole moments. In particular, the orientation of the QD considered in the this section is taken along X axis to achieve approximately the most efficient coupling between the QD and the gap mode [1]. Hence, light is preferentially emitted to the gap mode. We study

[1] For the guided plasmonic mode, E_x and E_z are in the plane in which the the dipole moment of QDs dominates. However the field strength of the longitudinal component (E_z) is less than 1%

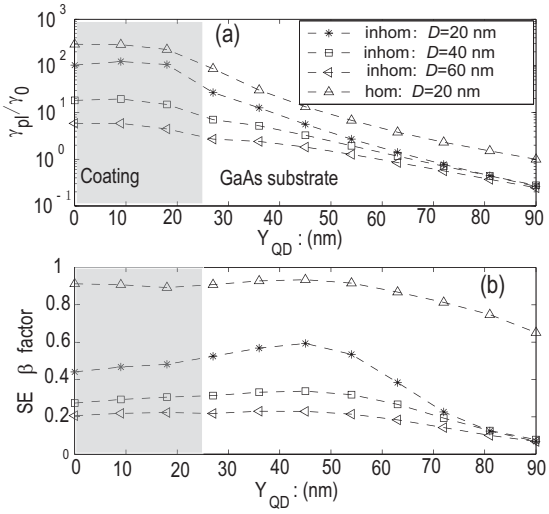

Figure 4.8: Position dependence of the plasmonic decay rates and SE β-factors for the metallic slot waveguide with inhomogenous environment($n_c = 1.5$, $n_s = 3.5$) and the homogenous case ($n_c = n_s = 1.0$) with $X_{QDs} = 0$, $H = 40$ nm, $W = 100$ nm.

the influence of the width of the gap, the height of the metallic strips, and the inhomogeneity on the SE β-factor for the gap mode. To avoid the field singularities induced by sharp metallic corners, the corners are smoothed by an arc with radius of 2 nm, and the substrate is etched 5 nm around the metal.

In the following calculations, the width of the metallic strip is fixed to be 100 nm to ensure operation in the regime of a single (gap) mode. First, we study gap-width dependence of the plasmonic decay rate and SE β-factor for an ideal QD positioned in the middle of the gap ($X_{QDs} = Y_{QDs} = 0$) in Fig. 4.7, for both the inhomogeneous and the homogenous environment. The plasmonic decay rate for the inhomogeneous case, shown in Fig. 4.7(a), is comparable to that of the homogenous case, which indicates that the electric field in the middle of the gap is not much influenced by inhomogeneity, though the overall field distribution for the inhomogeneous case contracts to the substrate-coating interface. However, the SE β-factor for metallic slot waveguide embedded in an inhomogeneous dielectric environment is severely impacted by inhomogeneity. We observe three distinct features: I) The

of the transverse components (E_x), therefore, we only consider the X component of the electric field and the exciton dipole moment for the plasmonic emission enhancement

SE β-factor shown in Fig. 4.7(b) for the inhomogeneous case is significantly reduced compared with the homogenous case shown in Fig. 4.7(e); II) In Fig. 4.7(b), the SE β-factor decreases monotonically with the gap-width, while for the homogenous case Fig. 4.7(d) indicates a maximum value of the SE β-factor for an optimized gap width when $H = 40nm$ and $H = 60nm$. We attribute such a significant reduction of the SE β-factor in Fig. 4.7(b) to the leaky plasmonic modes, arising from the inhomogeneity of the dielectric environment. It is well known that the interaction of light with inhomogeneities induces evanescent waves. When the metallic slot waveguide is embedded in an inhomogeneous dielectric environment, apart from the aforementioned three channels, the evanescent waves induced by inhomogeneity of the dielectric environment will present additional competing channels for the QD, which dissipate a considerable fraction of the emitted power from the source. Secondly, the optimum gap width in Fig. 4.7(e) stems from the compromise of competition between the plasmonic decay channel and the non-radiative decay channel, both of which depend on the distance from the emitter to the edge of the metals. For the optimized gap width, we observe an SE β-factor larger than 90%, which indicates that with 90% success probability a single optical plasmon will be generated, and consequently can be employed as an efficient single-photon source.

From a waveguiding point of view, there is a tradeoff between the confinement of the optical field and the propagation length [142], since the more confined the field of the mode is, the shorter the mode propagates due to the intrinsic losses of the metals. In order to couple the optical plasmons out as single photons, the optical plasmons are required to propagate with a reasonable distance, i.e., a few micro meters. From Fig. 4.7(f), we can see clearly the tradeoff between the plasmonic excitation rate and the propagation lengths, since the plasmonic excitation rate is proportional to the confinement of the field. In the inhomogeneous dielectric environment, shown in Fig. 4.7(c), the tradeoff between the plasmonic excitation rates and the propagation lengths can also be observed for small gap widths, while for larger gaps, the field distribution depends more and more on the dielectric inhomogeneity, which means that the propagation length does not increase any further, although the field is less confined. Apart from the reduction of the plasmonic decay rates and SE β-factor, the dielectric inhomogeneity also decreases the propagation lengths by a factor of 5 compared with the homogenous case, which might make the out coupling of the optical plasmons challenging.

Moreover, as can be seen from Fig. 4.7, the plasmonic decay rate and SE β-factor are rather sensitive to the gap width (D), but not to the height of the metals (H).

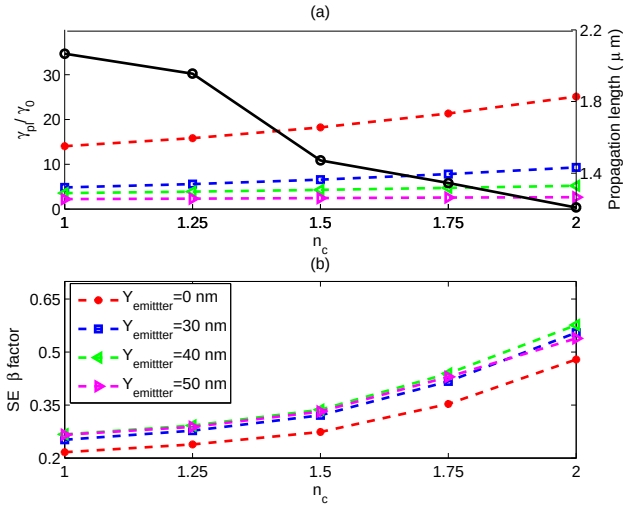

Figure 4.9: Role of inhomogeneous environment, quantified by variation of plasmonic decay rate and SE β-factor with n_c for fixed $n_s = 3.5$, $X_{QDs} = 0$, $H = 40$ nm, $W = 100$ nm, $D = 40$ nm. The black line shows the propagation length of the gap mode.

The interpretation is that the transverse mode profile of the gap mode is mainly determined by the gap-width, rather than the height of the metal. Therefore we take the height H as a fixed value ($H = 40$ nm), and examine the position as well as the gap width dependence of the plasmonic decay rate and SE β-factor, cf. Fig. 4.8. As can be seen from Fig. 4.8, the plasmonic decay rate and the SE β-factor increase when the gap width becomes smaller, which originates from the stronger confinement of the field for the waveguide with smaller gap width. Regarding the position dependence, the plasmonic decay rate drops when the emitter is moved away from the metals, while the SE β-factor remains almost the same when Y_{QDs} is smaller than 50 nm. We also observe that the maximum SE β-factor (close to 60%) is achieved at a position outside the gap for $D = 20$ nm. Another striking difference between the homogenous dielectric environment [10] and the inhomogenous dielectric environment with the same geometric sizes is that the SE β-factor is reduced significantly. The leaky modes that appear due to the inhomogeneity of the waveguide [141], and are confined in the coating region and leak away through the substrate region, thus seriously impact the achievable SE β-factor.

Our interpretation in terms of the significant role played by the leaky plasmonic modes is confirmed by the inhomogeneity dependence study in Fig. 4.9. An increased value of n_c, has three consequences: (I) The field will distribute more homogenously, which results in an increase of the plasmonic decay rate, especially for the emitter positioned in the middle of the gap; (II) The leaky plasmonic modes will contribute less, and we also observe that the SE β-factor is increased to above 50%. As can be seen from Fig. 4.6, decreasing the index contrast of the dielectric environment will narrow the spectral range of leaky plasmonic modes, and consequently their contributions will be suppressed; (III) The propagation length becomes shorter since the increased value of n_c will give rise to a larger value of the effective mode index, consequently the mode will become more confined. When increasing n_c beyond the value of 2, higher order modes will be excited for the particular waveguide in Fig. 4.9, the study of which is outside the scope of the thesis.

4.3 Conclusion

In this chapter, firstly we have briefly discussed the properties of the single photon sources as well as different types of emitters. Secondly we have studied the efficiency with which emission from a single self-assembled quantum dot can be coupled to a realistic metallic slot waveguide. With typical structure sizes, the emitted radiation can be efficiently coupled to a single guided mode supported by the metallic slot waveguides. We have found that the SE β-factor for the excited mode depends strongly on the parameters of the waveguide, especially on the homogeneity of the surrounding structure. Compared to the case of coupling to a metallic slot waveguide with symmetric dielectric environment, the SE β-factor is strongly reduced. We have attributed the significant reduction to the leaky modes induced by the inhomogeneity. By increasing the refractive index of the coating layer to minimize the impact of the leaky plasmonic modes, we have found that the coupling efficiency of the quantum dot to the single mode supported by the metallic slot waveguide can be above 50%. We also found that there is a balance between the coupling efficiency and the propagation length of the optical plasmons, which indicates that in addition to the competition between the three channels of SE decay, the propagation loss of the optical plasmons needs to be taken into account, to achieve a high overall efficiency of a plasmon-based single-photon source.

Chapter 5

Optical nano-antenna based single photon sources

5.1 Introduction

Nano-scales devices that funnel all the light emitted from light sources into a single guided mode of a nanocircuit, or preferential directions are highly desired in a wide range of nanosciences, spanning from quantum optics, single molecules spectroscopy to plasmonics. A practical implementation of such functional devices is the optical analogue of a famous radio wave antenna knows as Yagi-Uda antenna, recently proposed by several group [12, 13, 14, 15]. Such nanoantenna can produce very narrow beam over a broad bandwidth. Independently of the directionality, the optical nanoantennas also provide an excellent platform to control the spontaneous emission of a quantum emitter for efficient single photon sources [143]. Due to the phase matching between the eigenmodes supported by the metallic arrays and the free photons, the emitter can be efficiently coupled to the far field radiation in a very narrow beam, which can be collected simply by an objective lens and further forwarded into an optical fiber. Importantly, the emitter can decay much faster due to excitation of local plasmon resonances. Meanwhile, the emitter can maintain a high quantum efficiency when it is appropriately placed, even though the metals are lossy. In this chapter, we explore the possibilities of using optical nanoantenna to control the spontaneous emission with the target of efficient single photons sources. Firstly, we briefly study basic concepts of antennas. Secondly, we

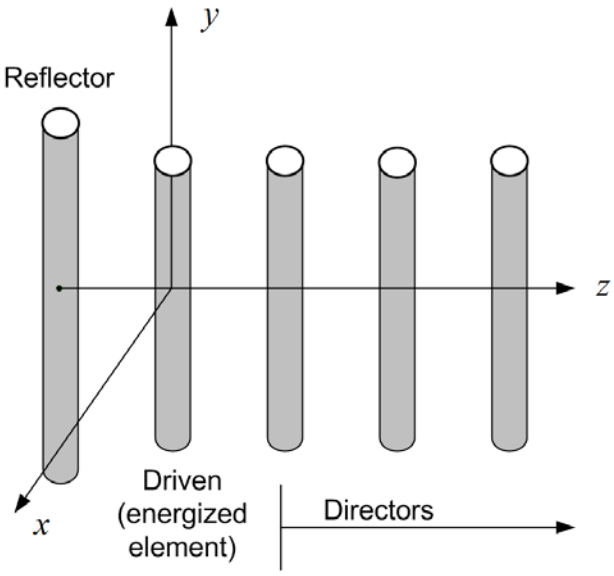

Figure 5.1: Sketch of radio wave Yagi-Uda antenna, consisting of a reflector, a driven element and several directors.

mimic the conventional Yagi-Uda antenna to realize its optical analogy based on an array consisting of several metallic rods. Our calculations show that such an antenna can produce a very narrow beam as well as a pronounced Purcell effect on the emitter. In the end, we propose a plasmon-based reconfigurable antenna to controllably distribute emission from single quantum emitters in spatially separated channels. Our calculations show that crossed particle arrays can split the stream of photons from a single emitter into multiple narrow beams. We predict that beams can be switched on and off by switching the host refractive index.

5.1.1 Radio wave antenna

An antenna is a transducer that receives or transmits electromagnetic waves, particularly for the radio and micro wave radiation [144]. In other words, antennas convert the far field radiation into electric current, or vice versa [144]. Due to the pioneering work carried by Hertz, antennas have been known for more than one century. In the first experiment, Hertz used an end loaded dipole as the transmitting antenna and a resonant square loop antenna as receiver for a complete radio system that operates on meter scale [83]. Nowadays, antennas are the indispensable

components in the communication link for aircraft and ships, cellular phones and various types of wireless devices [145].

Among many different configurations, the Yagi-Uda antenna is very simple and practical, and has been widely used as a home TV antenna due to the cheap cost, robustness, and ease to make [144]. As sketched in Fig. 5.1, a Yagi-Uda antenna consists of a number of linear dipole elements, one of which is energized directly by a feed transmission line while the rest acts as parasitic radiators whose currents are induced by mutual coupling [144]. The Yagi-Uda antenna is a directional antenna designed to maximize reception or delivery of electromagnetic energy along z axis, which is perpendicular to the dipole in the plane of the elements. Due to the dipolar resonance, the lengths of the metallic rods are usually around $\lambda/2$, and all the elements are spaced about $\lambda/4$ apart. All the elements usually lie in the same plane, supported on a single boom or crossbar.

The Yagi-Uda antenna is designed to function as an end-fire antenna, which is realized by having the parasitic elements in the forward beam acting as directors, while the one in the rear as a reflector [144]. The end-fire beam formation is realized by shortening the director elements, compared with the corresponding resonant length. According to the equivalent circuit theory, the impedance of each director is capacitive and its current gives rise to the induced electromagnetic field, while the impedance of the reflector is capacitive and the phases of its current lag the induced electromagnetic field [144]. The Yagi-Uda antenna can be considered as a traveling wave structure, the supported traveling waves finally detach themselves from the last director element. The performance, i.e., directivity, is determined by the current distribution in each element and also the phase velocity of the traveling wave.

5.1.2 Antenna basics

Since the concept of the optical antenna is transplanted from the radio wave antenna, it is necessary to introduce the basic concepts from the radio wave antennas that are going to be applied for the optical antenna in the following sections.

A radiation pattern is a graphical representation of the radiation properties determined in the far field region and is represented as a function of the directional coordinates [144], as shown in Fig. 5.2. Radiation properties can be the power flux density, radiation intensity, field strength, directivity, and so on. The power radiated from an antenna per unit solid angle is called radiation intensity U. The normalized power pattern can be expressed in terms of radiation intensity $U(\theta, \phi)$,

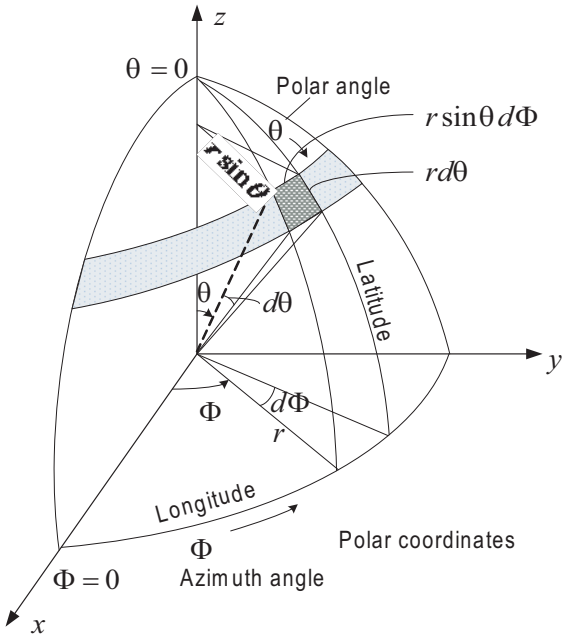

Figure 5.2: Polar coordinates showing the observation points in terms of polar angle θ and azimuth angle ϕ, and the incremental solid angle $d\Omega$.

as a function of angle, to its maximum value [144]. Thus

$$P(\theta, \phi) = \frac{U(\theta, \phi)}{U(\theta, \phi)_{max}} = \frac{S(\theta, \phi)}{S(\theta, \phi)_{max}}, \tag{5.1}$$

whereas the Poynting vector S depends on the distance from the antenna (varying inversely as the square of the distance), and the radiation intensity U is independent of distance, assuming in both cases that we are in the far field of the antenna.

In the radio wave antenna theory, another two basic concepts are the input impedance and radiation resistance of the antenna, which is explored in the framework of equivalent circuit theory. Figure 5.3 shows the antenna in the transmitting mode and the corresponding equivalent circuit model [144]. The input impedance presented by an antenna at its terminals is defined as the ratio of the voltage to current at a pair of terminals or the ratio of the approximate components of the electric to magnetic fields at a point. For instance, shown in Fig. 5.3 (b), the impedance is equal to ratio of the voltage to the current at the terminals a, b without loading.

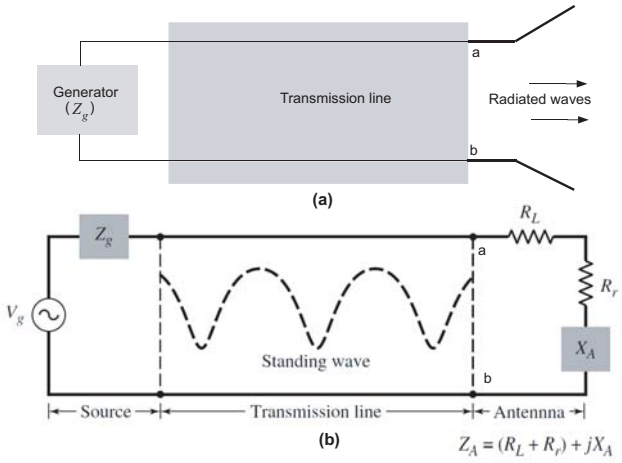

Figure 5.3: Transmission-line Thevenin equivalent of antenna in transmitting mode. (a) antenna in the transmitting mode, (b) the equivalent circuit.

The impedance of the antenna is described as

$$Z_A = R_A + jX_A, \tag{5.2}$$

where R_A is the antenna resistance at terminals $a - b$ consisting of radiation resistance R_r and loss R_L, i.e., $R_A = R_r + R_L$, and X_A is the antenna reactance at terminals $a - b$. In Figure 5.3 (b), the current induced by the generator within the loop is $I_g = V_g/(Z_g + Z_A)$, then the power delivered to R_r for the far field radiation is $I_g^2 R_r/2$, and the amount dissipated in R_L as heat is $I_g^2 R_L/2$. Hence, by combining the two one can calculate the antenna radiation efficiency as

$$\eta_A = \frac{R_r}{R_L + R_r}, \tag{5.3}$$

The maximum power transported to the antenna occurs when we have conjugate matching [144], namely, $Z_g = Z_A^*$. The input impedance of an antenna is normally frequency dependent. Thus the antenna is only matched to the interconnecting transmission line within a certain bandwidth. Moreover, the input impedance of the antenna dependents on many factors, such as its geometry, the method of driving, and surrounding materials. Only for some simple geometry, the input impedance can be investigated analytically, many others need to be determined experimentally or numerically.

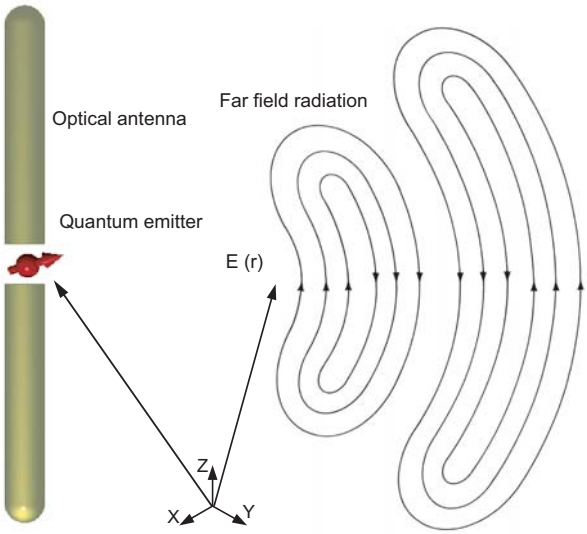

Figure 5.4: The role of optical antenna in the interaction between the local light sources and the far field radiation.

5.2 Optical nanoantenna

5.2.1 General considerations

Usually an antenna is defined as a metallic device, i.e., rod or wire, for radiating or receiving radio waves and microwaves. The radio wavelength is in the range of several centimeter to several hundred meters. Antennas own the characteristic dimension on the order of wavelength, thus the smaller scale and more demanding accuracies make the optical nanoantenna challenging. However, the remarkable advancements in nano-science and nano-technology provide such possibilities. The optical analogue of the radio wave antennas has attracted considerable interests recently [12, 13, 14, 15, 146], due to the ability of surpassing the diffraction limit and manipulating light at the real nanometer scale. In practice, optical antennas can be considered as a bridge between the source/sink of radiation, i.e., molecule or quantum dot, and the far field radiation [146]. Importantly, an optical antenna can make the transfer of energy between the two more efficient. Hence, such nanometer antennas promise broad potential applications such as light-emitting diodes, photovoltaics [62].

Light lies in the frequencies where the electronic transitions of the material take place, the optical antenna is normally driven by an atom, a molecule, or a quantum dot, rather than a transmission line that is used for radio waves antennas. As sketched in Fig. 5.4, the interaction between the local light sources, i.e., different type of emitters, and free space electromagnetic waves is mediated by the optical antenna. Three distinctive features arise due to the presence of optical nanoantenna: (I) the LDOS can be enhanced tremendously. It has been reported that the spontaneous emission decay rate of a quantum emitter embedded in the middle of a bowtie antenna can be enhanced by a factor of 1340 experimentally [147]. (II) The intrinsic properties of the emitter may also be modified, i.e., the polarizability α. It essentially means that the high order moments of the quantum emitter that normally are neglected, apart from the dipole moment, can also contribute to the transition matrix element due to the highly localized field [146]. (III) The far field emission pattern is primarily determined by the optical nanoantenna, which is also the main functionality in the conventional radio and micro wave antennas [12, 13, 14, 15]. The first two features indicate that the pronounced enhancement of the interaction between the emitter and the light can be achieved by using optical antenna at single quanta level.

5.2.2 Optical circuit concept for nanoantenna

Though optical antennas are strongly analogous to their radio and microwave counterpart, they have clear differences from each other, e.g., the different response of metals in the two frequency regimes, which makes a direct downscaling of the conventional antenna design impossible. Nonetheless it is still possible to construct equivalent circuit theory for the optical antenna. Engheta et al, showed that it is possible to transplant the design strategies and concepts into nanoantennas which operate in optical frequency range, such as input impedance, nanocircuit loading, and radiation tuning for optical antennas [148, 149, 150]. Engheta and his group reported that the half-wavelength optical dipole antenna with a finite feed gap in the center, as illustrated in Fig. 5.5 (a), bears a remarkable resemblance to the radio wave dipole antenna in terms of dipole resonance, input impedance and antenna loading [148, 149]. The starting point is to assign the optical "lumped impedance" to nano-antenna by taking the ratio between the averaged optical potential to the displacement current. The impedance of the nano-object depends on its shape, size and also the material property. Depending on the response of material three different types of lumped impedance may exit. If the material is dielectrics (metals)

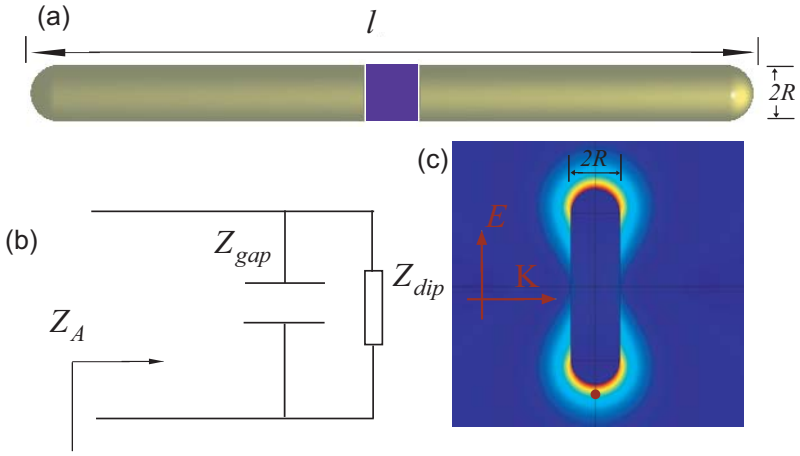

Figure 5.5: (a) the optical dipole antenna with a finite feed gap, (b) the sketch of a circuit model, and (c) Scattering of light by the metallic rod illuminated by a plane wave with incident field parallel with the rod. Red dot denotes observation point. The color scale indicates the field amplitude $|E|$.

with $\mathtt{Re}(\epsilon) > 0$ ($\mathtt{Re}(\epsilon) < 0$), the nano-object will behave as a capacitive (inductive) impedance [150]. For the lossy material $\mathtt{Im}(\epsilon) \neq 0$, the nano-object can be consider as a resistor [150]. As shown the Fig. 5.5 (b), the impedance equals to the parallel combination of the impedance of the dipole itself and the impedance from the contribution of the dielectric in the gap. For a fixed l, it is found that the antenna hits several resonances. At the first resonance where $\mathtt{Im}(Z_A) = 0$, it is essentially the dipole resonance with $l = \lambda_{eff}/2$, which can be seen as a "short-circuit" resonance in which the radio wave dipole antenna operates [148, 149]. On the blue side, the second order resonance $l = \lambda_{eff}$ emerges and Z_A yields an "open-circuit" resonance with large impedance, which is also qualitatively analogous to an radio wave antenna [148, 149]. One remark in terms of the resonances is the effective wavelength, which is shorter than the vacuum wavelength due to the large momentum of optical plasmons. The utilization of effective wavelength also underlies the differences between the optical antenna and the radio wave antenna, which will be further discussed in the following. Moreover, by loading the antenna gap with different materials, one can tune the optical response of the nanodipole antennas with large flexibility [149]. These basic concepts may pave the roadmaps towards future

innovations in nanoscale optical antenna based devices.

5.2.3 Effective wavelength and metallic rods based optical Yagi-Uda antenna

For the radio and micro wave antenna, it is the high conductivity of the metals that gives rise to the currents, which convert the localized energy in the form of far field radiation, or vice versa. While for the optical antenna, it is the plasmonic resonant features that assist the translation of the local electromagnetic energy from the light sources into the propagating waves. Due to the frequency dependence of the optical response of the metals, penetration length of electromagnetic wave into the metals called skin depth for radio waves is negligible, while for light the skin depth is on the order of tens of nanometers. Consequently, such plasmonic effect prevents the prescription of determining the antenna parameters in terms of vacuum wavelength [146], which gives rise to a shorter effective wavelength seen by the antenna. Novotny showed that the effective wavelength for a finite metallic rod with a smoothing in both ends by rod radii R shown in Fig. 5.5 (c) can be approximately given by [151],

$$\lambda_{eff} = \frac{\lambda_0}{n_{eff}} - 4R, \tag{5.4}$$

where λ_0 is the vacuum wavelength, and n_{eff} is the effective mode index of the fundamental mode, which is implicitly assumed to be the only guided plasmonic for the infinite long rod due to the comparable size of rod radii R with the skin depth. The substraction of $4R$ is an approximated value and originates from the apparent increase of the antenna length due to the reactant response of the rod ends [151].

Once the effective wavelength is known, the dipolar resonant length l_d for the finite metallic segment can hence be obtained by halving λ_{eff}. Another option of obtaining the dipolar resonance length is to monitor the length dependence of the field amplitude at a point with fixed distance to one rod end in the presence of a plane wave illumination [152], shown in Fig. 5.5 (c). For a silver rod embedded in polymer (n=$\sqrt{2}$) with radius of 20 nm at the operation wavelength of 1 μm, one can calculate the dipolar resonance length $l_d = 178$ nm from scaled wavelength defined by Eq. (5.4). As shown in Fig. 5.6, the monitored field amplitude calculated by using COMSOL reaches its maximum when the metallic rod is in the dipolar resonance, indicating a value of 171 nm for dipolar resonance length l_d from our numerical calculations. The small difference might arise from the large value of radius (20 nm) used here. Higher order resonances can also be calculated from Fig. 5.6 by

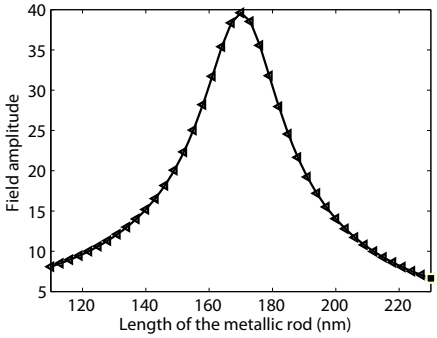

Figure 5.6: Rod length dependence of scattering field amplitude (relative to the magnitude of the incident field). The distance of the observation point is 5 nm away from the rod end.

Table 5.1: Rods lengths and pitches for a radio wave antenna normalized by the operation wavelength

Rod labels	Lr	Ld1	Ld2	Ld3	Ld4	Ld5	Ld6
Rod length	0.4869	0.4367	0.4312	0.4258	0.4203	0.4161	0.412
Spacing labels	Sr	Sd1	Sd2	Sd3	Sd4	Sd5	Sd6
Spacing	0.12	0.1775	0.1992	0.2209	0.2414	0.2579	0.2779

extending the metallic rod longer. The higher order resonances are seldom used in antenna designs, hence we limit ourself to employ the dipolar resonance to construct the optical type of Yagi-Uda antenna.

The dipolar resonance length is the key for construction of the optical type Yagi-Uda antenna from the metallic rods. Following a recipe for an eight-element Yagi-Uda RF antenna, we study its optical analogy by using aforementioned scaling, as shown in Fig. 5.7. The spacing and the length of each rod of the optical nanoantenna are illustrated in Fig. 5.7 (a), and the whole structure is embedded in the ordinary polymer with refractive index of $\sqrt{2}$. The rod lengths and spacings between two adjoint rods of an eight-element Yagi-Uda RF antenna are tabulated in Table 5.1. For the rod lengths, the effective wavelength, i.e., $2l_d = 342$ nm for the 20 nm radii silver wire in our case, should be considered as the operation wavelength. For the spacing, the effective wavelength should be scaled by refractive index of the surrounding material to obtain the real operation wavelength, i.e., $\frac{1}{\sqrt{2}}$ μm.

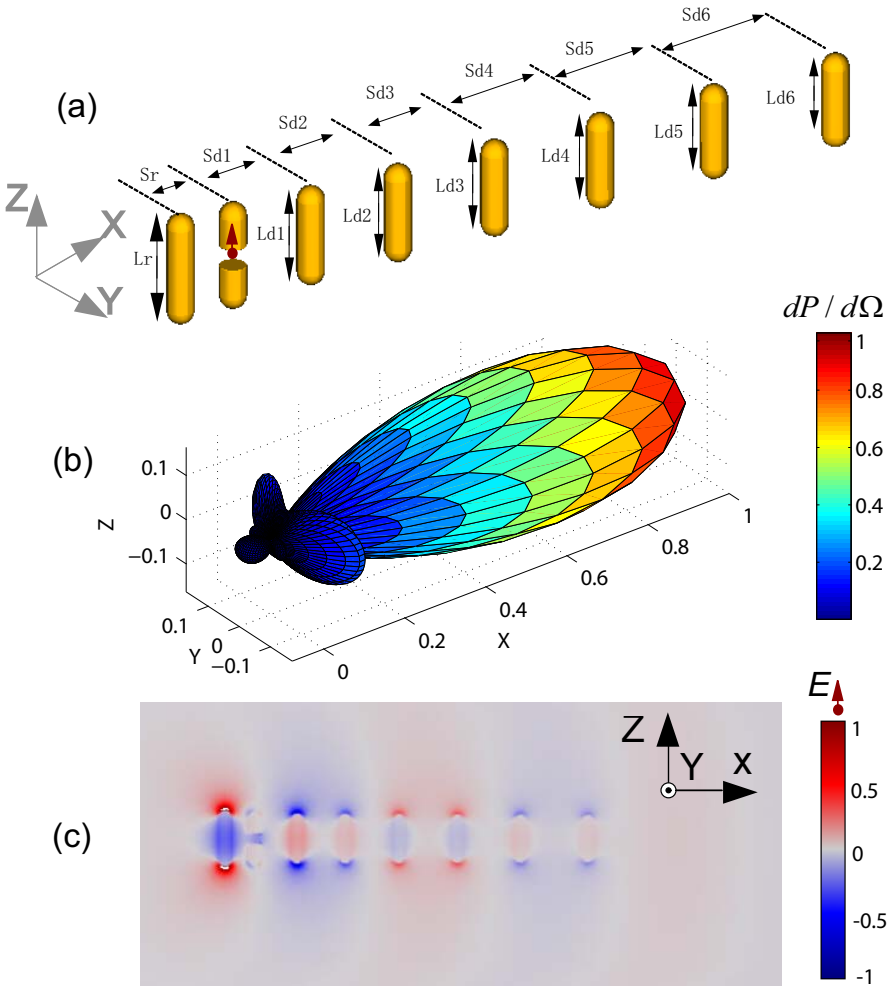

Figure 5.7: (a) Sketch of the nano-optical Yagi-Uda antenna with 8 elements coupled to a quantum emitter. (b) Emission pattern for the emission at λ=1 μm. The emission represents the radiation intensity defined as the power emitted per steradian ($dP/d\Omega$) normalized to its maximum in the forward direction. (c) Snapshot in the $\boldsymbol{X}-\boldsymbol{Z}$ plane of the $\boldsymbol{Z}$-component of the electric field generated by the radiating dipole.

With these concerns in mind, we calculate the far field emission pattern and the near field distribution as shown in Figs. 5.7 (b) and 5.7 (c), the calculation of which is also implemented in COMSOL. We observe an enhanced directional emission due to the presence of metallic rods, cf. Fig. 5.7 (b). The far field emission pattern indicates a 10 times brightness enhancement over a free dipole in the forward direction, and 90% of the emission can be collected in the forward cone by using a objective lens with a numerical aperture of $\sim$0.4. It is also remarkable that such large directionality can be realized with a structure ($\lambda/6$ wide, 1.2 λ long) that is comparable to the wavelength in vacuum. The near field in the antenna excited by the dipole emitter shown in Fig. 5.7 (c) provides the microscopic insight into the predicted beaming. The radiating dipole emitter excites strong transverse dipolar resonances on all the metallic rods, which substantially modify the far field emission pattern of the dipole emitter by itself. Apart from the strong modification of the far field emission pattern, optical nano-antenna can also enhance the spontaneous emission decay rate of the dipole emitter tremendously. Our calculations show that with optimized gap width for energized element the emission rate enhancement can be up to 100 with relative high quantum efficiency. Hence, such Yagi-Uda type of optical nanoantenna can function as efficient single photon sources.

5.3 Reconfigurable directionality for multiple-branch antenna

5.3.1 Mechanism of the reconfigurable directionality

The essence of the optical type of Yagi-Uda antenna is the strong scattering of light due to the antenna elements, which are also required to interact with each other coherently. Such strong scatters can also be replaced by using other shapes, i.e., metallic spheres. It was reported recently that a finite long metallic particle chain coupled to emitters can produce directional emission with narrow beams [14, 15]. In these optical nanoantennas, a feature that would be extremely useful for plasmon-based quantum networks is dynamic reconfigurability. In a quantum network in which several localized qubits interact via emission of photons, one would desire reconfigurable coupling between nodes in the network of qubits. By analogy to radio wave antennas, one might expect that plasmon antennas used to control emitters can be reprogrammed with ease to arbitrarily steer beams. However, programmable radio wave antennas use methods inaccessible to plasmonics, as they usually use

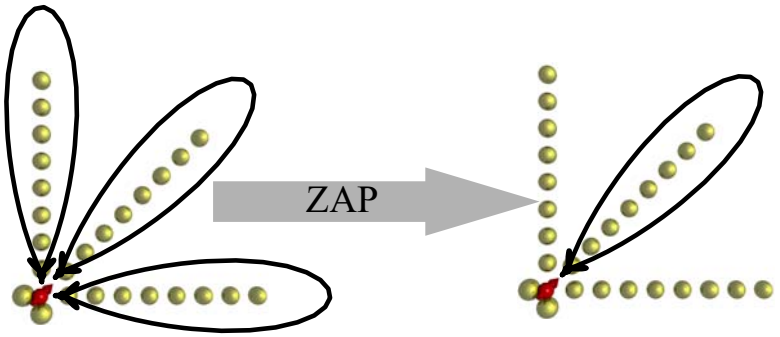

Figure 5.8: Sketch of the reconfigurable nanoantenna concept to control single emitters. We consider a single emitter (red dipole) embedded in a set of linear plasmon antennas (metal particles in yellow) that intersect at the emitter. In its unswitched state (left), such an antenna funnels spontaneous emission into different beams. The beams can be switched on and off (indicated by "ZAP") at will by modifying the particle or host material dynamically.

individual phase control over many active elements. In this section we study a different strategy to obtain control of reconfigurable plasmon antennas for single emitters. Our method rests on controlling the dispersion relation of guided modes in each part of a multi-arm traveling wave plasmon antenna by switching the refractive index of the surrounding medium. Intuitively, the large bandwidth of plasmonic antennas implies that larger index changes are needed to switch than in high Q dielectric cavities. We show that an effective reconfigurable switch can be reached with host index changes that are achievable with liquid crystals [153].

We consider multi-beam antennas that split the stream of photons emitted by a single emitter into several channels, as shown in Fig. 5.8, each corresponding to a narrow beam of $< 30^\circ$ full width at half maximum [12, 13, 14, 15]. We explore the possibility of dynamically switching on and off each beam at will, for instance by controlling the refractive index surrounding the antenna. We envisage that such a dynamically reconfigurable multi-beam antenna can be useful in quantum optics, to controllably couple a local qubit to a select number of other qubits. First, let us consider how the multi-beam antenna works in its unswitched state. Following a proposal by Li et al. [154], we propose that a multi-beam antenna with N beams can be made by combining N antenna arms that each consist of a linear array of metal particles, and essentially act like Yagi-Uda type antennas at optical frequencies.

Recent reports have shown that such antennas can force single emitters to emit into a narrow beam over a broad bandwidth that is demarcated on the blue edge by an abrupt cut-off. The cut-off wavelength depends on antenna geometry [15]. The physics can be understood by considering a Yagi-Uda antenna as a traveling wave antenna, the behavior of which is governed by the dispersion relation for an one dimensional infinite plasmon chain [155]. When the emission frequency is tuned to the lower dispersion branch, the emitter decays into a plasmonic mode bound to the antenna, and with a wave vector beyond the light line, see Fig. 5.9 (b). The finite antenna length causes efficient out-coupling of this mode, which hardly radiates in the case of infinite plasmon chains. For a linear plasmon particle array of length L, momentum conservation is only defined within $\triangle k \approx \pi/L$. This determines the cut-off wavelength of efficient beaming. The wavelength at which the dispersion relation deviates more than $\triangle k$ from the light line, marked by the blue bar in Fig. 5.9 (b), corresponds to the cut-off wavelength. If the operation wavelength denoted by λ_{op}, is longer than the cut-off wavelength, the plasmon chain acts as a directional antenna for single-photon emission. If λ_{op} is shorter than the cut-off wavelength, the emitter decays into dark plasmons [15]. Importantly, the cut-off is very sharp and occurs within a few nanometer spectral bandwidth [15]. Such abrupt on/off behavior is essential for optical switching of reconfigurable plasmon antennas.

5.3.2 Linear array: results and discussion

As a first example, we study the coupling of a single emitter to an antenna with two identical arms, consisting of silver spheres (radius $R = 55$ nm), arranged in a linear array with pitch of $d = 160$ nm, shown in Fig. 5.9 (a). We use tabulated constants from E. D. Palik [68]. The array is embedded in glass ($n = 1.5$) and the dipole emitter is transverse to the arrays. The real part of the corresponding infinite chain dispersion relation for the transverse mode, (black curve in Fig. 5.9 (b)), is calculated from a point-dipole model [155]. Since both arms are identical, they have exactly the same dispersion relation, and the emitted photon is split into two identical beams. As in the case of a single Yagi-Uda antenna, the beams have a full width at half maximum of 30 degrees, as calculated using "MESME". "MESME" is an exact electrodynamic multiple scattering multipole expansion method developed by F. J. García de Abajo for rigorously solving Maxwell's equations for finite clusters of scatters [98, 97, 15]. The fact that we choose a linear antenna (180° between arms) is not essential: we obtain similar splitting into two beams for perpendicular

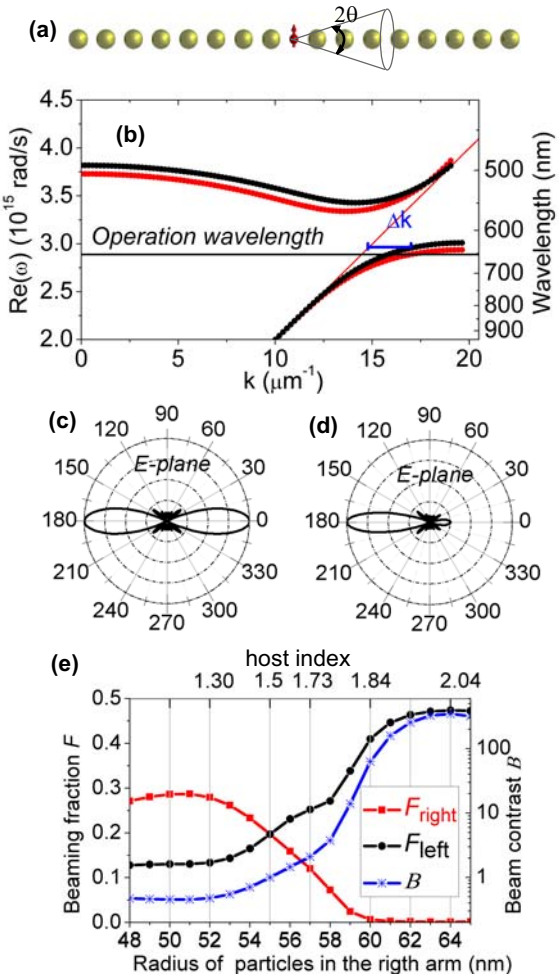

Figure 5.9: (a) Sketch of the emitter-antenna geometry consisting of two identical arms. We consider a single emitter placed in the middle of the antenna, oriented perpendicular to the antenna axis. The emitter is embedded in the middle of the two arms, 80 nm distance away from the front of each arm. (b) The black (red) curve represents the dispersion relation for the transverse plasmon modes of an infinite Ag particle chain in glass (pitch d=160 nm, particle size R=55 (58) nm). The black horizontal line indicates the operation wavelength at 652 nm. (c/d) Emission pattern at $\lambda = 652$ nm for a single emitter embedded in a linear array antenna, with 8 silver particles to each side. In (c) both arms are equal (R=55 nm). In (d) the right arm has R=58 nm. (e) Radius/host index (top axis) dependence of the beaming fraction and beam contrast. The beaming fraction assumes collection in a cone of width $sin(\theta) = 0.32$ ($2\theta = 36°$).

arms.

We consider how much perturbation is required to switch one of the two beams off. Two facts are immediately obvious: First, since we start with a symmetric antenna, we require an asymmetric perturbation to switch only one of the beams. Second, we expect a dramatic change in emission pattern only if the perturbation shifts the cut-off wavelengths through λ_{op}. Therefore λ_{op} is chosen close to the cut-off wavelength. Before focusing on a specific switching mechanism, we note that the key parameter that determines the dispersion is the polarizability α of each particle. In the electrostatic approximation we have $\alpha = 3V(\varepsilon - n^2)/(\varepsilon + 2n^2)$, with particle volume $V = 4\pi R^3/3$, host index n and metal dielectric constant ε. To obtain a first estimate for the amount $\triangle\alpha$ needed to shift the dispersion sufficiently, we artificially vary $\triangle\alpha$ through $\triangle R$, even though this may not be physically realizable in a dynamical manner. We discuss realistic implementations below. We find that at fixed pitch and fixed host index, the dispersion red shifts as particle size increases, c.f the red curve in Fig. 5.9 (b). When the particle size is increased from $R = 55$ nm to $R = 58$ nm, the shift amounts to ~ 20 nm, which moves the cut-off wavelength through λ_{op}. We therefore expect a dramatic change in radiation pattern. Indeed the calculation (Fig. 5.9 (c-d)) shows a single narrow beam emanating from the unswitched arm, and disappearance of the beam from the switched arm.

In order to quantify the quality of the switching behavior, we define two figures of merit. The first figure of merit called the beaming fraction F, quantifies how much of the total emitted power is emitted into the left arm and right arm, respectively $F_{\mathrm{left/right}} = \int_{(\Omega_0,\mathrm{left/right})} P d\Omega / \int_{(4\pi)} P d\Omega$, where P is the power radiated per solid angle. We define a solid angle Ω_0, which we take to correspond to a numerical aperture $\mathtt{NA} = sin(\theta)$, that one would use to collect the radiation of each beam in practice. The second figure of merit called the beam contrast $B = F_{\mathrm{left}}/F_{\mathrm{right}}$ quantifies the on/off contrast, and is defined as the brightness contrast between the two arms. We plot both figures of merit in Fig. 5.9 (e) for different magnitudes of the perturbation of the right hand arm of the antenna. At $R = 55$ nm, both arms are equal and carry equal amounts of energy ($B = 1$). For a fixed $\mathtt{NA} = 0.32$ one would collect a fraction of $\sim 20\%$ of emitted power in each beam. For particle size R=58 nm in the right hand beam, the right beam is strongly reduced to below $\sim 3\%$. At the same time the left beam gains a factor two in brightness. The contrast between the beams hence shifts from $B = 1$ to several hundred. In order to translate the required $\triangle R$ back to a physically realizable switch, we note that $\Delta R/R \sim 10\%$. We hence conclude that a two-beam antenna with identical arms can be reconfigured

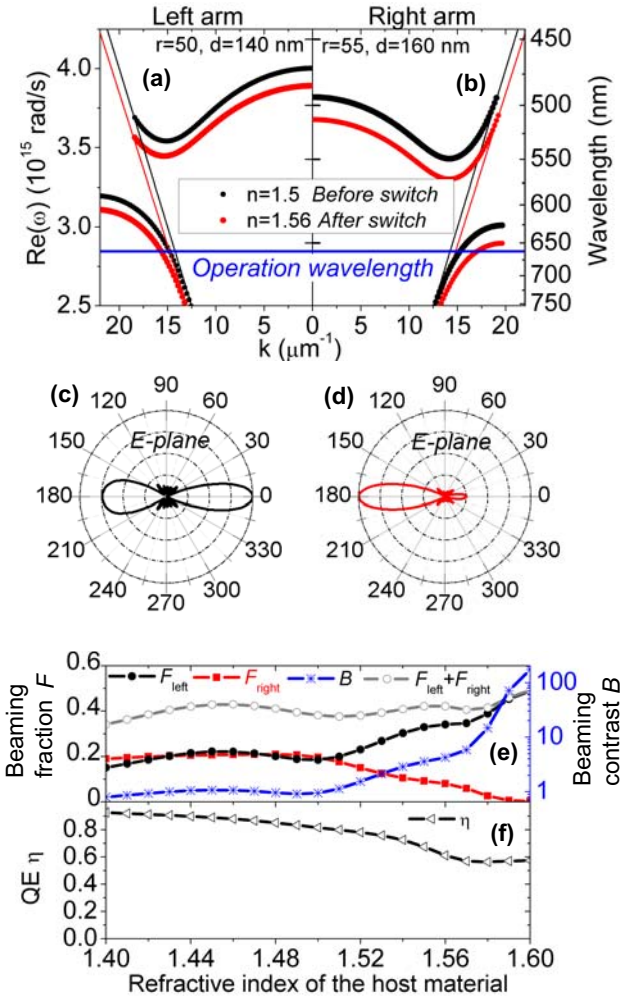

Figure 5.10: Results for an asymmetric two beam antenna, with R=50 nm, d=140 nm in the left arm and R=55nm, d=160 nm in the right arm. (a/b) shows the dispersion relation for transverse plasmons for each arm before (black curve) and after the switch (red curve). (c/d) Emission pattern for a single emitter in the antenna (both arms with 8 particles) before (c) and after (d) switching host index from 1.5 to 1.56. (e) Host index dependence of the beaming fraction and beam contrast at $\lambda = 662$ nm. (f) Quantum efficiency versus the variation of host index at $\lambda = 662$ nm.

provided one finds a way to change the polarizability of particles in one arm of the antenna by 30%. Since the only feasible method to change polarizability is to change the host index, we convert $\triangle\alpha$ into a required change in host index (top axis in Fig. 5.9 (e)). An immense change from $n = 1.5$ to $n = 1.85$ would be required, which is unachievable in any practical material. We conclude that prospects for switching are dim when one starts out from antennas that are symmetric in the unswitched states.

To overcome these challenges, we now consider a two-beam antenna that consists of different arms to begin with. Due to the asymmetric geometry in which particle size and pitch are chosen smaller ($R = 50$ nm, $d = 140$ nm) in the left arm already at the fabrication stage, the dispersion relation for the two arms are shifted already in the unswitched states, shown in Fig. 5.10 (a). In the right hand branch, λ_{op} is much closer to the cut-off than in the left branch. This yields the possibility of switching just one beam off selectively by a homogenous switch in host material index, provided that the cut-off of the right hand branch shifts beyond λ_{op}, while λ_{op} remains to the red side of the cut-off in the left arm. Figure 5.10 (c) shows that in the unswitched ($n = 1.5$) state, the emission from the emitter is indeed split into two beams. Due to the intrinsic asymmetry in geometry, both beams do not have equal angular width, although they carry comparable power. As the host index is raised from 1.5 to 1.56, the dispersion curves bend further away from the light line, shifting the cut-off wavelength in both branches to the red (Fig. 5.10 (b)). Figure 5.10 (d) confirms that the left beam remains, while the right beam switches off, in accordance with with the shift in cut-off wavelengths.

Figure 5.10 (e) allows us to assess the figures of merit of the proposed switch, assuming $\lambda_{op} = 662$ nm. We plot the dependence of the beaming fraction, and the beam contrast as a function of host index. While the beam contrast is approximately equal at $n = 1.5$, we see a marked contrast between left and right beams at $n > 1.56$. Hence we conclude that beams in a multi-beam antenna can be switched at will with a manageable index change, provided we carefully choose the dispersion relation for each antenna branch. The role of the dispersion relation is further confirmed in Fig. 5.11, which shows the beaming fraction for the two arms as a function of both operation wavelength and host index. There is a band throughout which each arm shows pronounced directional emission with approximately equal power. To the blue side of the cut-off of the right hand arm, the right hand beam has very low intensity, and the intensity of the left arm is increased by a factor of 2. To the blue of the cut-offs of both waveguides, neither arm generates a bright and directional

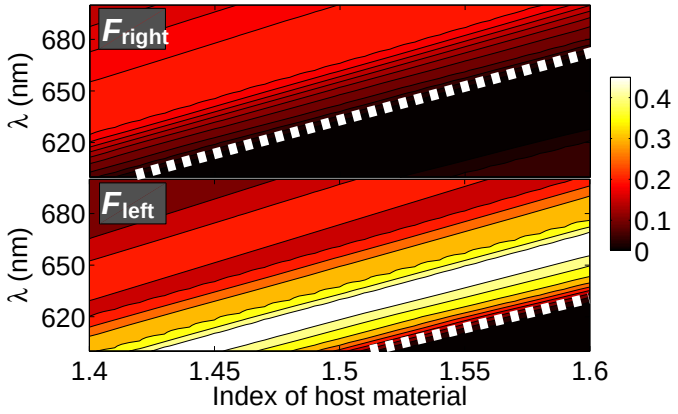

Figure 5.11: Contour plot of beaming fraction F versus host index and wavelength. The dashed white lines denote the cut-off wavelengths for the directional emissions. In a 30 nm band to the red of the cutoff of the right arms, both beams have comparable power. In between the cutoffs, the right beam becomes extinct, while the left beam becomes brighter.

beam. This result shows that the switch can be optimized for any λ_{op} in a wide band, by antenna geometry and host index, and that due to the sharp antenna cut-off only modest index changes are required, which are achievable in practice. We believe that the design philosophy presented here is generally valid in any traveling wave antenna system in which the dispersion relation imposes a sharp and tunable cut-off for each antenna arm. The figures of merit can hence be expected to improve as new traveling wave antenna designs are proposed in the field of plasmonics.

5.3.3 Outlook of the reconfigurable plasmon-based single photon sources

we have proposed a method to realize reconfigurable plasmon antennas, e.g., for controlling the coupling of single emitters with nodes in a quantum network. Essential for our method is the dispersion relation underlying traveling wave antennas that provides a sharp tuneable cut-off. The specific design for a two beam antenna presented in this section uses host refractive index changes from n=1.5 to n=1.56. Such changes are in the range accessible with liquid crystals and phase change ma-

terials, [153, 156] but above the level accessible with, e.g., photochromic polymers [157] or thermal index tuning. Particularly promising is the use of a photo sensitive liquid crystal with potentially picosecond response time to UV pulses. [153, 157] Birefringence in the liquid crystal is generally no problem even for bent antennas, as long as the anisotropy is perpendicular to all antenna arms. Birefringence might even provide more versatile switching, as different arms can be switched differently through orientation relative to the axes of the birefringent host. Alternatively, embedding the Yagi-Uda antennas inside a semiconductor matrix (Si or GaAs) would allow ultrafast switching using free carrier excitation [158]. The operation wavelength in that case shifts to the infrared due to the high host index. In addition to the specific refractive index demands, we note several obstacles for reconfigurable optical antennas. First we note that despite the high directivity evident in Figs. 2 and 3, the side lobes contain a significant fraction of the emission. Indeed, at a 36° full width collection cone considered here, the two beams contain only about 50% of the emitted power (Fig. 5.10 (e)). One may note a slight variation of the sum $F_{\text{left}} + F_{\text{right}}$ with host index, due to dark plasmon excitation and emission side lobes. Enlarging the NA, or embedding the nanoscale antennas in micron scale dielectric waveguides will suppress the side lobes, while retaining high light matter interaction strength. As a second obstacle, we note that turning off a beam does not necessarily double the brightness of the remaining beam, as is evident from the drop in quantum efficiency in Fig. 5.10 (f). The quantum efficiency is reduced because the branch that is switched off still captures emission in the form of dark plasmons. Such losses can be avoided by using other resonant scatterers. We have calculated that Yagi-Uda antennas also work when made from high index (Si) particles. This configuration not only avoids loss but would also allow easier switching, since the particles themselves can be optically switched. Thirdly we notice that Yagi-Uda antennas are limited by the fact that the dispersion cut-off only occurs at one edge (blue edge). In N-beam antennas ($N > 2$) it is hence not possible to switch arbitrary combinations of beams. Nonetheless, our design strategy paves the way for plasmon quantum optics on the chip.

5.4 Conclusion

Optical nano-antenna can be used to mimic the traditional antennas to forward optical waves into desirable directions. In this chapter, we have extended such concept further to explore the possibilities of using optical antenna for developing

efficient single photon sources. Firstly, we have constructed an optical analogy of Yagi-Uda antenna by using the effective wavelength scaling based on the recipe of a radio wave antenna. Our calculations have shown that such transplantation yields directional emission with narrow beams. The spontaneous emission decay rate can be enhanced by taking advantage of the localized plasmon resonance in the feeding element. Secondly, a steerable plasmon-based single photon source has been proposed. Instead of metallic rods, metallic particle arrays with finite length can also function as Yagi-Uda antenna. We have shown that crossed particle arrays can split the stream of photons from a single emitter into multiple narrow beams. We predict that beams can be switched on and off by tuning the host refractive index that are achievable with liquid crystals.

Chapter 6

Summary and outlook

Surface plasmon polaritons are electromagnetic excitations associated with charge density waves. The tight confinement of the electromagnetic field gives the possibility of enhancing light-matter interaction. Understanding of such plasmon enhanced light emission from a single emitter embedded in complex photonic environment is crucial for developing efficient plasmon-based devices, i.e., single photon sources. Such a single emitter model incorporating the realistic photonic structures can be extremely useful to study the Purcell effect and emission profile of the light sources in the presence of metallic structures. This thesis presents a detailed modeling of plasmon mediated light matter interaction.

A FEM approach of calculating a single emitter coupled to plasmonic waveguides has been developed. The method consists of a 2D model and a 3D model: (I)In the 2D model, we have calculated the spontaneous emission decay rate of a single emitter into guided plasmonic modes by taking the advantage of the translation symmetry of the waveguides along the propagation direction; (II) In the 3D model, we have implemented the FEM calculation to include the radiation modes and the nonradiative contributions by solving the wave equation with a harmonic source terms. The FEM approach developed in the thesis is a flexible method, which can handle the plasmonic waveguides with different geometries, as long as only one guided plasmonic mode is dominating excited.

We have applied our numerical method to calculate the coupling of a single emitter to plasmonic waveguides embedded in a homogenous or an inhomogeneous dielectric environment. For the homogenous dielectric environment, we have calculated the coupling efficiency of the single emitter to a metallic nanowire, a squared

plasmonic waveguide and a metallic gap structure. We found the emission can be efficiently coupled to the plasmonic waveguide. We further compared the cylindrical metallic nanowire with previous work that employed quasistatic approximation. We found that the quasistatic approximation is typically valid when the size is less than the skin depth of the metals at optical frequencies. For the inhomogeneous dielectric environment, we have found that the coupling efficiency of an emitter to a metallic slot waveguide is significantly reduced, compared to the ideal case of a homogenous dielectric environment. We attributed the reduction to the coupling to leaky plasmonic modes. By increasing the refractive index of the coating layer to minimize the impacts from the leaky plasmonic modes, we found that the coupling efficiency of the quantum dot to the single mode supported by the metallic slot waveguide can be enhanced by more than a factor of 2.

We have examined the light emission from a single emitter mediated optical nanoantennas. Based the scaling of the operation wavelength, we have constructed an optical analogy of Yaga-Uda antenna from a recipe developed in the field of radio wave antenna. We have shown such optical nanoantennas yield strong directional emission. By engineering the dispersion relation of plasmon particle chain, we have proposed a steerable plasmon-based single photon sources. We have predicted the the beams can be switched on and off by switching the host refractive index.

For the future work, there are some interesting research work to be carried out. The first one is to examine the single photon absorption by a single emitter mediated by optical Yagi-Uda nanoantennas. It is expected that the presence of the optical nanoantenna can merit the single photon absorption by a single emitter, similar to the fact that the TV antenna on the roof of our houses can improve the reception of the radio waves. The second task is to study the fundamental limitations of the plasmonic benefits for the light emission of an emitter embedded in a substrate with higher refractive index, where the plasmonic structures are deposited on the top of the substrate. Such work may have tremendous impacts on the quantum optics which is primarily based on III-V semiconductors, as well as LEDs.

List of Figures

List of Tables

Bibliography

[1] J. M. Gérard, B. Sermage, B. Gayral, B. Legrand, E. Costard, and V. Thierry-Mieg. Enhanced spontaneous emission by quantum boxes in a monolithic optical microcavity. *Phys. Rev. Lett.*, 81(5):1110–1113, Aug 1998.

[2] Matthew Pelton, Charles Santori, Jelena Vučković, Bingyang Zhang, Glenn S. Solomon, Jocelyn Plant, and Yoshihisa Yamamoto. Efficient source of single photons: A single quantum dot in a micropost microcavity. *Phys. Rev. Lett.*, 89(23):233602, Nov 2002.

[3] D. K. Armani, T. J. Kippenberg, S. M. Spillane, and K. J. Vahala. Ultra-high-Q toroid microcavity on a chip. *Nature*, 421:925–928, Feb 2003.

[4] T. Yoshie, A. Scherer, J. Hendrickson, G. Khitrova, H. M. Gibbs, G. Rupper, C. Ell, O. B. Shchekin, and D. G. Deppe. Vacuum rabi splitting with a single quantum dot in a photonic crystal nanocavity. *Nature*, 432(7014):200–203, November 2004.

[5] Igor I. Smolyaninov, Jill Elliott, Anatoly V. Zayats, and Christopher C. Davis. Far-field optical microscopy with a nanometer-scale resolution based on the in-plane image magnification by surface plasmon polaritons. *Phys. Rev. Lett.*, 94(5):057401, Feb 2005.

[6] Junichi Takahara, Suguru Yamagishi, Hiroaki Taki, Akihiro Morimoto, and Tetsuro Kobayashi. Guiding of a one-dimensional optical beam with nanometer diameter. *Opt. Lett.*, 22(7):475–477, 1997.

[7] S. I. Bozhevolnyi, V. S. Volkov, E. Devaux, J.-Y. Laluet, and T. W. Ebbesen. Channel plasmon subwavelength waveguide components including interferometers and ring resonators. *Nature*, 440:508–511, March 2006.

[8] A. V. Akimov, A. Mukherjee, C. L. Yu, D. E. Chang, A. S. Zibrov, P. R. Hemmer, H. Park, and M. D. Lukin. Generation of single optical plasmons in metallic nanowires coupled to quantum dots. *Nature*, 450:402–406, Nov 2007.

[9] Chang D. E., Sørensen A. S., Hemmer P. R., and Lukin M. D. Quantum optics with surface plasmons. *Phys. Rev. Lett.*, 97(5):053002, Aug 2006.

[10] Y. C. Jun, R. D. Kekapture, J. S. White, and M. L. Brongersma. Nonresonant enhancement of spontaneous emission in metal-dielectric-metal plasmon waveguide structures. *Phys. Rev. B*, 78(15):153111, 2008.

[11] Yuntian Chen, Torben Roland Nielsen, Niels Gregersen, Peter Lodahl, and Jesper Mørk. Finite-element modeling of spontaneous emission of a quantum emitter at nanoscale proximity to plasmonic waveguides. *Phys. Rev. B*, 81(12):125431, Mar 2010.

[12] Holger F Hofmann, Terukazu Kosako, and Yutaka Kadoya. *New. J. Phys.*, 9(7):217, 2007.

[13] Jingjing Li, Alessandro Salandrino, and Nader Engheta. Shaping light beams in the nanometer scale: A yagi-uda nanoantenna in the optical domain. *Phys. Rev. B*, 76(24):245403, Dec 2007.

[14] Terukazu Kosako, Yutaka Kadoya, and Holger F. Hofmann. Directional control of light by a nano-optical yagi-uda antenna. *Nature Photonics*, 4, March 2010.

[15] A. Femius Koenderink. Plasmon nanoparticle array waveguides for single photon and single plasmon sources. *Nano Lett.*, 9(12):4228, 2009.

[16] Yuntian Chen, Niels Gregersen, Torben Roland Nielsen, Jesper Mørk, and Peter Lodahl. Spontaneous decay of a single quantum dot coupled to a metallic slot waveguide in the presence of leaky plasmonic modes. *Optics Express*, 18(12):12489–12498, 2010.

[17] Yuntian Chen, Torben Roland Nielsen, Niels Gregersen, Peter Lodahl, and Jesper Mørk. Finite-element modeling of spontaneous emission of a quantum emitter at nanoscale proximity to plasmonic waveguides. *Phys. Rev. B*, 82(12):125431, Mar 2010.

[18] R. J. Thompson, G. Rempe, and H. J. Kimble. Observation of normal-mode splitting for an atom in an optical cavity. *Phys. Rev. Lett.*, 68(8):1132–1135, Feb 1992.

[19] M. Brune, F. Schmidt-Kaler, A. Maali, J. Dreyer, E. Hagley, J. M. Raimond, and S. Haroche. Quantum rabi oscillation: A direct test of field quantization in a cavity. *Phys. Rev. Lett.*, 76(11):1800–1803, Mar 1996.

[20] A. Wallraff, D. I. Schuster, A. Blais, L. Frunzio, Huang, J. Majer, S. Kumar, S. M. Girvin, and R. J. Schoelkopf. Strong coupling of a single photon to a superconducting qubit using circuit quantum electrodynamics. *Nature*, 431(7005):162–167, Sep 2004.

[21] E. M. Purcell. Spontaneous emission probabilities at radio frequencies. *Phys. Rev.*, 69(1):681, Dec 1946.

[22] Sajeev John. Strong localization of photons in certain disordered dielectric superlattices. *Phys. Rev. Lett.*, 58(23):2486–2489, Jun 1987.

[23] Eli Yablonovitch. Inhibited spontaneous emission in solid-state physics and electronics. *Phys. Rev. Lett.*, 58(20):2059–2062, May 1987.

[24] John D. Joannopoulos, Robert D. Meade, and Joshua N. Winn. *Photonic Crystals: Molding the Flow of Light.* Princeton University Press, 1 edition, 1995.

[25] J. D. Joannopoulos, Pierre R. Villeneuve, and Shanhui Fan. Photonic crystals. *Solid State Communications*, 102(2–3):165–173, Apr 1997.

[26] W. L. Barnes, A. Dereux, and T. W. Ebbesen. Surface plasmon subwavelength optics. *Nature*, 424:824–830, Aug 2003.

[27] Anatoly V. Zayats, Jill Elliott, Igor I. Smolyaninov, and Christopher C. Davis. Imaging with short-wavelength surface plasmon polaritons. *Appl. Phys. Lett.*, 86(15):151114, 2005.

[28] J. B. Pendry, A. J. Holden, W. J. Stewart, and I. Youngs. Extremely low frequency plasmons in metallic mesostructures. *Phys. Rev. Lett.*, 76(25):4773–4776, Jun 1996.

[29] J. B. Pendry, A. J. Holden, D. J. Robbins, and W. J. Stewart. Magnetism from conductors and enhanced nonlinear phenomena. *Microwave Theory and Techniques, IEEE Transactions on*, 47(11):2075–2084, Aug 2002.

[30] D. R. Smith, Willie J. Padilla, D. C. Vier, S. C. Nemat-Nasser, and S. Schultz. Composite medium with simultaneously negative permeability and permittivity. *Phys. Rev. Lett.*, 84(18):4184–4187, May 2000.

[31] Rodney Loudon. *The Quantum Theory of Light*. Oxford University Press, 3 edition, 2000.

[32] J. Dalibard, J. Dupont-Roc, and C. Cohen-Tannoudji. Vacuum fluctuations and radiation reaction: identification of their respective contributions. *J. Phys.*, 43:1617–1638, 1982.

[33] J. Dalibard, J. Dupont-Roc, and C. Cohen-Tannoudji. Dynamics of a small system coupled to a reservoir: reservoir fluctuations and self-reaction. *J. Phys.*, 45:637–656, 1984.

[34] H. P. Urbach and G. L. J. A. Rikken Rikken. Spontaneous emission from a dielectric slab. *Phys. Rev. A*, 57(5):3913–3930, May 1998.

[35] Jeppe Johansen, S. Stobbe, Ivan S. Nikolaev, Toke Lund-Hansen, Philip T. Kristensen, J. M. Hvam, Willem L. Vos, and Peter Lodahl. Size dependence of the wavefunction of self-assembled inas quantum dots from time-resolved optical measurements. *Phys. Rev. B*, 77(7):073303, 2008.

[36] Gunnar Björk, Susumu Machida, Yoshihisa Yamamoto, and Kazuhiro Igeta. Modification of spontaneous emission rate in planar dielectric microcavity structures. *Phys. Rev. A*, 44(1):669–681, Jul 1991.

[37] P. Lodahl, A. F. van Driel, I. S. Nikolaev, A. Irman, K. Overgaag, D. Vanmaekelbergh, and W. L. Vos. Controlling the dynamics of spontaneous emission from quantum dots by photonic crystals. *Nature*, 430(7000):654–657, August 2004.

[38] Daniel Kleppner. Inhibited spontaneous emission. *Phys. Rev. Lett.*, 47(4):233–236, Jul 1981.

[39] T. Lund-Hansen, S. Stobbe, B. Julsgaard, H. Thyrrestrup, T. Sünner, M. Kamp, A. Forchel, and P. Lodahl. Experimental Realization of Highly

Efficient Broadband Coupling of Single Quantum Dots to a Photonic Crystal Waveguide. *Phys. Rev. Lett.*, 101(11):113903–113906, September 2008.

[40] Katrin Kneipp, Yang Wang, Harald Kneipp, Lev T. Perelman, Irving Itzkan, Ramachandra R. Dasari, and Michael S. Feld. Single molecule detection using surface-enhanced raman scattering (sers). *Phys. Rev. Lett.*, 78(9):1667–1670, Mar 1997.

[41] Shuming Nie and Steven R. Emory. Probing single molecules and single nanoparticles by surface-enhanced raman scattering. *Science*, 275(5303):1102–1106, Feb 1997.

[42] N. E. Hecker, R. A. Hopfel, N. Sawaki, T. Maier, and G. Strasser. Surface plasmon-enhanced photoluminescence from a single quantum well. *Appl. Phys. Lett.*, 75(11):1577–1579, 1999.

[43] K. B. Crozier, A. Sundaramurthy, G. S. Kino, and C. F. Quate. Optical antennas: Resonators for local field enhancement. *J. Appl. Phys.*, 94(7):4632–4642, 2003.

[44] T. H. Taminiau, F. D. Stefani, F. B. Segerink, and N. F. van Hulst. Optical antennas direct single-molecule emission. *Nature Photonics*, 2(4):234–237, April 2008.

[45] Sergei Kühn, Ulf Hakanson, Lavinia Rogobete, and Vahid Sandoghdar. Enhancement of single-molecule fluorescence using a gold nanoparticle as an optical nanoantenna. *Phys. Rev. Lett.*, 97(1):017402, 2006.

[46] D. E. Chang, A. S. Sørensen, E. A. Demler, and M. D. Lukin. A single-photon transistor using nanoscale surface plasmons. *Nature Physics*, 3:807–812, Nov 2007.

[47] D. E. Chang, A. S. Sørensen, P. R. Hemmer, and M. D. Lukin. Strong coupling of single emitters to surface plasmons. *Phys. Rev. B*, 76(3):035420, Jul 2007.

[48] Lukas Novotny and Bert Hecht. *Principles of Nano Optics*. Cambridge University Press, 2ed edition, 2006.

[49] Jean-Claude Weeber, Alain Dereux, Christian Girard, Joachim R. Krenn, and Jean-Pierre Goudonnet. Plasmon polaritons of metallic nanowires for controlling submicron propagation of light. *Phys. Rev. B*, 60(12):9061–9068, Sep 1999.

[50] George H. Goedecke and Sean G. O'Brien. Scattering by irregular inhomogeneous particles via the digitized green's function algorithm. *Appl. Opt.*, 27(12):2431–2438, 1988.

[51] Rémi Carminati and Jean-Jacques Greffet. Influence of dielectric contrast and topography on the near field scattered by an inhomogeneous surface. *J. Opt. Soc. Am. A*, 12(12):2716–2725, 1995.

[52] Olivier J. F. Martin, Christian Girard, and Alain Dereux. Generalized field propagator for electromagnetic scattering and light confinement. *Phys. Rev. Lett.*, 74(4):526–529, Jan 1995.

[53] Magdy F. Iskander, H. Y. Chen, and J. E. Penner. Optical scattering and absorption by branched chains of aerosols. *Appl. Opt.*, 28(15):3083–3091, 1989.

[54] Philip Trøst Kristensen, Peter Lodahl, and Jesper Mørk. Light propagation in finite-sized photonic crystals: multiple scattering using an electric field integral equation. *J. Opt. Soc. Am. B*, 27(2):228–237, 2010.

[55] Roy J. Glauber. Coherent and incoherent states of the radiation field. *Phys. Rev.*, 131(6):2766–2788, Sep 1963.

[56] V. V. Klimov and M. Ducloy. Spontaneous emission rate of an excited atom placed near a nanofiber. *Phys. Rev. A*, 69(1):013812, Jan 2004.

[57] William L. Barnes, Alain Dereux, and Thomas W. Ebbesen. Surface plasmon subwavelength optics. *Nature*, 424(6950):824–830, Aug 2003.

[58] J. Zenneck. Über die ausbreitung ebener elektro-magnetischer wellen langs einer ebenen leiterflache und ihre beziehung zur drahtlosen telegraphie. *Annalen der Physik*, 23:846–866, 1907.

[59] A. Sommerfeld. Über die ausbreitung der wellen in der drahtlosen telegraphie. *Annalen der Physik*, 28:665–736, 1909.

[60] Stefan A. Maier. *Plasmonics: Fundamentals and Applications.* Springer, Berlin, 1st edition, May 2007.

[61] T. W. Ebbesen, H. J. Lezec, H. F. Ghaemi, T. Thio, and P. A. Wolff. Extraordinary optical transmission through sub-wavelength hole arrays. *Nature*, 391(6668):667–669, Feb 1998.

[62] Harry A. Atwater and Albert Polman. Plasmonics for improved photovoltaic devices. *Nature Materials*, 9(3):205–213, Feb 2010.

[63] Olga Lyandres Nilam C. Shah Jing Zhao Jeffrey N. Anker, W. Paige Hall and Richard P. Van Duyne. Biosensing with plasmonic nanosensors. *Nature Materials*, 7:442–453, 2008.

[64] H. Raether. *Surface Plasmonics*. Spring, Berlin, 1988.

[65] J. D. Jackson. *Classical Electrodynamics*. John Wiley & Sons, Inc., 3ed edition, 1999.

[66] B. Hecht, H. Bielefeldt, L. Novotny, Y. Inouye, and D. W. Pohl. Local excitation, scattering, and interference of surface plasmons. *Phys. Rev. Lett.*, 77(9):1889–1892, Aug 1996.

[67] Mark I. Stockman. Nanofocusing of optical energy in tapered plasmonic waveguides. *Phys. Rev. Lett.*, 93(13):137404, Sep 2004.

[68] Edward D. Palik. *Handbook of optical constants of solids II*. Academic Press, 1991.

[69] J. Jung, T. Søndergaard, and S. I. Bozhevolnyi. Theoretical analysis of square surface plasmon-polariton waveguides for long-range polarization-independent waveguiding. *Phys. Rev. B*, 76(3):035434, 2007.

[70] Pierre Berini. Plasmon-polariton waves guided by thin lossy metal films of finite width: Bound modes of symmetric structures. *Phys. Rev. B*, 61(15):10484–10503, Apr 2000.

[71] S. J. Al-Bader. Optical transmission on metallic wires–fundamental modes. *IEEE. J. Quant. Elec*, 40:325, 2004.

[72] Aloyse Degiron and David Smith. Numerical simulations of long-range plasmons. *Opt. Express*, 14(4):1611–1625, 2006.

[73] S. Chattopadhyay and P. K. Saha. Study of bound surface plasmon modes on subwavelength structures of rectangular cross section using a simple analytical technique. *J. Opt. A: Pure Appl. Opt.*, 10(9):095201, 2008.

[74] Sung Yong Park and David Stroud. Surface-plasmon dispersion relations in chains of metallic nanoparticles: An exact quasistatic calculation. *Phys. Rev. B*, 69(12):125418, Mar 2004.

[75] W. H. Weber and G. W. Ford. Propagation of optical excitations by dipolar interactions in metal nanoparticle chains. *Phys. Rev. B*, 70(12):125429, Sep 2004.

[76] D. S. Citrin. Plasmon-polariton transport in metal-nanoparticle chains embedded in a gain medium. *Opt. Lett.*, 31(1):98–100, 2006.

[77] A. Femius Koenderink and Albert Polman. Complex response and polariton-like dispersion splitting in periodic metal nanoparticle chains. *Phys. Rev. B*, 74(3):033402, Jul 2006.

[78] C. F. Bohren and D. R. Huffman. *Absorption and scattering of light by small particles.* John Wiley & Sons, Inc., 1983.

[79] J. A. Stratton. *Electromagnetic Theory.* McGraw-Hill, New York, 1ed edition, 1941.

[80] Walton C. Gibson. *The Method of Moments in Electromagnetics.* Taylor and Francis Group, 2007.

[81] Allen Taflove and Susan C. Hagness. *Computational Electrodynamics: The Finite-Difference Time-Domain Method.* Artech House, 2ed edition, 2000.

[82] Jian Min Jin. *The Finite Element Method in Electromagnetics.* Wiley-IEEE Press, 2ed edition, 2002.

[83] Jian Min Jin and Douglas J. Riley. *Finite Element Analysis of Antenna and Arrays.* Wiley-IEEE Press, 2002.

[84] Mark L. Brongersma and Pieter G. Kik. *Surface Plasmon Nanophotonics.* Springer, 2007.

[85] A. Femius Koenderink, Maria Kafesaki, Costas M. Soukoulis, and Vahid Sandoghdar. Spontaneous emission rates of dipoles in photonic crystal membranes. *J. Opt. Soc. Am. B*, 23(6):1196–1206, 2006.

[86] Yong Xu, Reginald K. Lee, and Amnon Yariv. Quantum analysis and the classical analysis of spontaneous emission in a microcavity. *Phys. Rev. A*, 61(3):033807, Feb 2000.

[87] C. Hermann and O. Hess. Modified spontaneous emission rate in an inverted-opal structure with complete photonic bandgap. *J. Opt. Soc. Am. B*, 19:3013, 2002.

[88] Bruce T. Draine and Piotr J. Flatau. Discrete-dipole approximation for scattering calculations. *J. Opt. Soc. Am. A*, 11(4):1491–1499, 1994.

[89] Georgios Veronis and Shanhui Fan. Guided subwavelength plasmonic mode supported by a slot in a thin metal film. *Opt. Lett.*, 30(24):3359–3361, 2005.

[90] T. Søndergaard and B. Tromborg. General theory for spontaneous emission in active dielectric microstructures: Example of a fiber amplifier. *Phys. Rev. A*, 64(3):033812, Aug 2001.

[91] A .W. Snyder and J. Love. *Optical Waveguide Theory.* Springer, 1983.

[92] Jian Min Jin. *The Finite Element Method in Electromagnetics.* Wiley-IEEE Press, 2ed edition, 2002.

[93] V. N. Kanellopoulos and J. P. Webb. The importance of the surface divergence term in the finite element-vector absorbing boundary condition method. *IEEE Trans. Microw. Theory Tech.*, 43(9):2168–2170, Sep 1995.

[94] J. P. Webb. Edge elements and what they can do for you. *IEEE Trans. Magnetics*, 29(2):1460–1465, Mar 1993.

[95] M. M. Botha and D. B. Davidson. Rigorous, auxiliary, variable-based implementation of a second-order abc for the vector fem. *IEEE Trans. Antennas Propag.*, 54:3499–3504, Nov. 2006.

[96] M.A. Yurkin and A.G. Hoekstra. The discrete dipole approximation: An overview and recent developments. *Journal of Quantitative Spectroscopy and Radiative Transfer*, 106(1-3):558 –589, 2007.

[97] F. J. García de Abajo and A. Howie. Relativistic electron energy loss and electron-induced photon emission in inhomogeneous dielectrics. *Phys. Rev. Lett.*, 80(23):5180–5183, Jun 1998.

[98] F. J. García de Abajo. Multiple scattering of radiation in clusters of dielectrics. *Phys. Rev. B*, 60(8):6086–6102, Aug 1999.

[99] Leonard Mandel and Emil Wolf. *Optical Coherence and Quantum Optics.* Cambridge University Press, 1 edition, 1995.

[100] R. Hanbury-Brown and R. Q. Twiss. Correlation between photons in two coherent beams of light. *Nature*, 177:27–29, 1956.

[101] P. Grangier, G. Roger, and A. Aspect. Experimental evidence for a photon anticorrelation effect on a beam splitter: A new light on single-photon interferences. *EPL (Europhysics Letters)*, 1(4):173–179, Feb 1986.

[102] H. J. Kimble, M. Dagenais, and L. Mandel. Photon antibunching in resonance fluorescence. *Phys. Rev. Lett.*, 39(11):691–695, Sep 1977.

[103] Brahim Lounis and Michel Orrit. Single-photon sources. *Reports on Progress in Physics*, 68(5):1129, 2005.

[104] Michael A. Nielsen and Isaac L. Chuang. *Quantum Computation and Quantum Information*. Cambridge University Press, 2000.

[105] C. H. Bennett and G. Brassard. Quantum cryptography and its application to provably secure key expansion, public-key distribution, and coin-tossing. *IEEE International Symposium on Information Theory*, page 91, 1983.

[106] Nicolas Gisin, Grégoire Ribordy, Wolfgang Tittel, and Hugo Zbinden. Quantum cryptography. *Rev. Mod. Phys.*, 74(1):145–195, Mar 2002.

[107] Dik Bouwmeester, Jian-Wei Pan, Klaus Mattle, Manfred Eibl, Harald Weinfurter, and Anton Zeilinger. Experimental quantum teleportation. *Nature*, 390:575–579, Dec 1997.

[108] E. Knill, R. Laflamme, and G. J. Milburn. A scheme for efficient quantum computation with linear optics. *Nature*, 409(6816):46–52, Jan 2001.

[109] T. C. Ralph, N. K. Langford, T. B. Bell, and A. G. White. Linear optical controlled-not gate in the coincidence basis. *Phys. Rev. A*, 65(6):062324, Jun 2002.

[110] H. Fearn and R. Loudon. Quantum theory of the lossless beam splitter. *Optics Communications*, 64(6):485 – 490, 1987.

[111] C. K. Hong, Z. Y. Ou, and L. Mandel. Measurement of subpicosecond time intervals between two photons by interference. *Phys. Rev. Lett.*, 59(18):2044–2046, Nov 1987.

[112] Norbert Lütkenhaus. Security against individual attacks for realistic quantum key distribution. *Phys. Rev. A*, 61(5):052304, Apr 2000.

[113] C. K. Hong and L. Mandel. Experimental realization of a localized one-photon state. *Phys. Rev. Lett.*, 56(1):58–60, Jan 1986.

[114] A. Imamoglu. Are quantum dots useful for quantum computation? *Physica E: Low-dimensional Systems and Nanostructures*, 16(1):47 –50, 2003.

[115] Axel Kuhn, Markus Hennrich, and Gerhard Rempe. Deterministic single-photon source for distributed quantum networking. *Phys. Rev. Lett.*, 89(6):067901, Jul 2002.

[116] J. McKeever, A. Boca, A. D. Boozer, R. Miller, J. R. Buck, A. Kuzmich, and H. J. Kimble. Deterministic Generation of Single Photons from One Atom Trapped in a Cavity. *Science*, 303(5666):1992–1994, 2004.

[117] Christian Brunel, Brahim Lounis, Philippe Tamarat, and Michel Orrit. Triggered source of single photons based on controlled single molecule fluorescence. *Phys. Rev. Lett.*, 83(14):2722–2725, Oct 1999.

[118] Th. Basché, W. E. Moerner, M. Orrit, and H. Talon. Photon antibunching in the fluorescence of a single dye molecule trapped in a solid. *Phys. Rev. Lett.*, 69(10):1516–1519, Sep 1992.

[119] W. Patrick Ambrose, Peter M. Goodwin, Jörg Enderlein, David J. Semin, John C. Martin, and Richard A. Keller. Fluorescence photon antibunching from single molecules on a surface. *Chemical Physics Letters*, 269(3-4):365 – 370, 1997.

[120] L. Fleury, J.-M. Segura, G. Zumofen, B. Hecht, and U. P. Wild. Nonclassical photon statistics in single-molecule fluorescence at room temperature. *Phys. Rev. Lett.*, 84(6):1148–1151, Feb 2000.

[121] B Lounis and W. E. Moerner. Single photons on demand from a single molecule at room temperature. *Nature*, 407:491–493, 2000.

[122] F. Treussart, R. Alléaume, V. Le Floc'h, L. T. Xiao, J. M. Courty, and J. F. Roch. Direct measurement of the photon statistics of a triggered single photon source. *Phys. Rev. Lett.*, 89(9):093601, Aug 2002.

[123] A. Gruber, A. Drabenstedt, C. Tietz, L. Fleury, J. Wrachtrup, and C. von Borczyskowski. Scanning Confocal Optical Microscopy and Magnetic Resonance on Single Defect Centers. *Science*, 276(5321):2012–2014, 1997.

[124] Thomas M. Babinec, Birgit J. M. Hausmann, Mughees Khan, Yinan Zhang, Jeronimo R. Maze, Philip R. Hemmer, and Marko Lončar. A diamond nanowire single-photon source. *Nature Nanotechnology*, 5:195–199, Feb.

[125] B. Lounis, H. A. Bechtel, D. Gerion, P. Alivisatos, and W. E. Moerner. Photon antibunching in single cdse/zns quantum dot fluorescence. *Chemical Physics Letters*, 329(5-6):399 –404, 2000.

[126] X. Brokmann, E. Giacobino, M. Dahan, and J. P. Hermier. Highly efficient triggered emission of single photons by colloidal cdse/zns nanocrystals. *Applied Physics Letters*, 85(5):712–714, 2004.

[127] Zhiming M. Zhang. *Self-Assemlbed Quantum Dots*. Springer, 2007.

[128] L. A. Coldren and S. W. Corzine. *Diode Laser and Photonic Integrated Circuits*. John Wiley Sons Inc, 1995.

[129] Peter Michler. *Single Semiconductor Quantum Dots*. Springer, 2009.

[130] Andrew J. Shields. Semiconductor quantum light sources. *Nature Photonics*, 1(4):215–223, Apr 2007.

[131] M. B. Ward, O. Z. Karimov, D. C. Unitt, Z. L. Yuan, P. See, D. G. Gevaux, A. J. Shields, P. Atkinson, and D. A. Ritchie. On-demand single-photon source for 1.3 mu m telecom fiber. *Applied Physics Letters*, 86(20):201111, 2005.

[132] Stefan Strauf, Nick G. Stoltz, Mattew T. Rakher, Larry A. Coldren, Pierre M. Petroff, and Dirk Bouwmeester. Single photons on demand from a single molecule at room temperature. *Nature Photonics*, 407:491–493, 2000.

[133] Charles Santori, Matthew Pelton, Glenn Solomon, Yseulte Dale, and Yoshihisa Yamamoto. Triggered single photons from a quantum dot. *Phys. Rev. Lett.*, 86(8):1502–1505, Feb 2001.

[134] G. S. Solomon, M. Pelton, and Y. Yamamoto. Single-mode spontaneous emission from a single quantum dot in a three-dimensional microcavity. *Phys. Rev. Lett.*, 86(17):3903–3906, Apr 2001.

[135] E. Moreau, I. Robert, J. M. Gerard, I. Abram, L. Manin, and V. Thierry-Mieg. Single-mode solid-state single photon source based on isolated quantum dots in pillar microcavities. *Applied Physics Letters*, 79(18):2865–2867, 2001.

[136] Julien Claudon, Joel Bleuse, Nitin S. Malik, Maela Bazin, Perine Jaffrennou, Niels Gregersen, Christophe Sauvan, Philippe Lalanne, and Jean-Michel Gerard. A highly efficient single-photon source based on a quantum dot in a photonic nanowire. *Nature Photonics*, 4(3):174–177, Jan 2010.

[137] A. Imamoglu, D. D. Awschalom, G. Burkard, D. P. DiVincenzo, D. Loss, M. Sherwin, and A. Small. Quantum information processing using quantum dot spins and cavity qed. *Phys. Rev. Lett.*, 83(20):4204–4207, Nov 1999.

[138] Tomonori Ishikawa, Shigeru Kohmoto, and Kiyoshi Asakawa. Site control of self-organized inas dots on gaas substrates by in situ electron-beam lithography and molecular-beam epitaxy. *Applied Physics Letters*, 73(12):1712–1714, 1998.

[139] Xiangang Luo and Teruya Ishihara. Surface plasmon resonant interference nanolithography technique. *Applied Physics Letters*, 84(23):4780–4782, 2004.

[140] Jeppe Johansen, S. Stobbe, Ivan S. Nikolaev, Toke Lund-Hansen, Philip T. Kristensen, J. M. Hvam, Willem L. Vos, and Peter Lodahl. Size dependence of the wavefunction of self-assembled inas quantum dots from time-resolved optical measurements. *Phys. Rev. B*, 77(7):073303, 2008.

[141] Rashid Zia, Mark D. Selker, and Mark L. Brongersma. Leaky and bound modes of surface plasmon waveguides. *Phys. Rev. B*, 71(16):165431, Apr 2005.

[142] Pierre Berini. Plasmon-polariton waves guided by thin lossy metal films of finite width: Bound modes of asymmetric structures. *Phys. Rev. B*, 63(12):125417, Mar 2001.

[143] R. Esteban, T. V. Teperik, and J. J. Greffet. Optical patch antennas for single photon emission using surface plasmon resonances. *Phys. Rev. Lett.*, 104(2):026802, Jan 2010.

[144] Constantine A. Bananis. *Antenna Theory: Analysis and Design.* Wiley-Interscience, 3ed edition, 2005.

[145] J. D. Kraus and R. J Marhefka. *Antennas for All Applications.* MacGras-Hill, 3ed edition, 2002.

[146] Palash Bharadwaj, Bradley Deutsch, and Lukas Novotny. Optical antennas. *Advances in Optics and Photonics*, 1(3):438–483, 2009.

[147] Anika Kinkhabwala, Zongfu Yu, Shanhui Fan, Yuri Avlasevich, Klaus Mullen, and W. E. Moerner. Large single-molecule fluorescence enhancements produced by a bowtie nanoantenna. *Nature Photonics*, 3(11):654–657, October 2009.

[148] Andrea Alù and Nader Engheta. Input impedance, nanocircuit loading, and radiation tuning of optical nanoantennas. *Phys. Rev. Lett.*, 101(4):043901, Jul 2008.

[149] Andrea Alù and Nader Engheta. Tuning the scattering response of optical nanoantennas with nanocircuit loads. *Nature Photonics*, 2(5):307–310, Apr 2008.

[150] Nader Engheta. Circuits with light at nanoscales: Optical nanocircuits inspired by metamaterials. *Science*, 317(5845):1698–1702, Sep 2007.

[151] Lukas Novotny. Effective wavelength scaling for optical antennas. *Phys. Rev. Lett.*, 98(26):266802, Jun 2007.

[152] Tim H. Taminiau, Robert J. Moerland, Frans B. Segerink, Laurens Kuipers, and Niek F. van Hulst. $\lambda/4$ resonance of an optical monopole antenna probed by single molecule fluorescence. *Nano Letters*, 7(1):28–33, 2007. PMID: 17212435.

[153] Pascale El-Kallassi, Rolando Ferrini, Libero Zuppiroli, Nicolas Le Thomas, Romuald Houdré, Audrey Berrier, Srinivasan Anand, and Anne Talneau. Optical tuning of planar photonic crystals infiltrated with organic molecules. *J. Opt. Soc. Am. B*, 24(9):2165–2171, 2007.

[154] Jingjing Li, Alessandro Salandrino, and Nader Engheta. Optical spectrometer at the nanoscale using optical yagi-uda nanoantennas. *Phys. Rev. B*, 79(19):195104, May 2009.

[155] A. Femius Koenderink and Albert Polman. Complex response and polariton-like dispersion splitting in periodic metal nanoparticle chains. *Phys. Rev. B*, 74(3):033402, Jul 2006.

[156] Christophe Arnold, Yichen Zhang, and Jaime Gomez Rivas. Long range surface polaritons supported by lossy thin films. *Applied Physics Letters*, 96(11):113108, 2010.

[157] Kevin G. Yager and Christopher J. Barrett. Novel photo-switching using azobenzene functional materials. *Journal of Photochemistry and Photobiology A: Chemistry*, 182(3):250 – 261, 2006.

[158] Tijmen G. Euser, Adriaan J. Molenaar, J. G. Fleming, Boris Gralak, Albert Polman, and Willem L. Vos. All-optical octave-broad ultrafast switching of si woodpile photonic band gap crystals. *Phys. Rev. B*, 77(11):115214, Mar 2008.